

July 2019

## Modulations of Lipid Membranes Caused by Antimicrobial Agents and Helix 0 of Endophilin

Nawal Kishore Khadka

University of South Florida, nawals\_id@yahoo.com

Follow this and additional works at: <https://scholarcommons.usf.edu/etd>

 Part of the [Biophysics Commons](#), and the [Physics Commons](#)

---

### Scholar Commons Citation

Khadka, Nawal Kishore, "Modulations of Lipid Membranes Caused by Antimicrobial Agents and Helix 0 of Endophilin" (2019). *Graduate Theses and Dissertations*.  
<https://scholarcommons.usf.edu/etd/7829>

This Dissertation is brought to you for free and open access by the Graduate School at Scholar Commons. It has been accepted for inclusion in Graduate Theses and Dissertations by an authorized administrator of Scholar Commons. For more information, please contact [scholarcommons@usf.edu](mailto:scholarcommons@usf.edu).

Modulations of Lipid Membranes Caused by Antimicrobial Agents and Helix 0  
of Endophilin

by

Nawal Kishore Khadka

A dissertation submitted in partial fulfillment  
of the requirements for the degree of  
Doctor of Philosophy in Applied Physics  
Department of Physics  
College of Arts and Sciences  
University of South Florida

Major Professor: Jianjun Pan, Ph.D.  
Jianfeng Cai, Ph.D.  
Sagar Pandit, Ph.D.  
Zhimin Shi, Ph.D.

Date of Approval:  
June 25, 2019

Keywords: Lipid bilayer, AFM, GUV, Peptidomimetics, Colistin, Endophilin H0

Copyright © 2019, Nawal Kishore Khadka

## ACKNOWLEDGMENTS

I would like to take this opportunity to thank all who had helped and inspired me during my graduate studies. First and foremost, I thank my advisor, Dr. Jianjun Pan for his continuous support, encouragement, and suggestions. I am grateful for his tremendous input on providing time, ideas, and funding during my stay with him. Without him, my journey throughout graduate studies would not be possible.

I thank the dissertation committee members Dr. Sagar Pandit, Dr Zhimin Shi, Dr Jianfeng Cai, and Dr Libin Ye (chairperson of examination committee) for serving in my dissertation committee and providing advices as well as support to accomplish this achievement.

I would like to thank my former Lab member Chian Sing (Josh) Ho who had been a great friend and lab partner during my early years. We learned together many experimental techniques, and helped each other to understand and employ them in our research work.

I thank the professors of the physics department Dr. Pritish Mukherjee, Dr. David Robson, Dr Ghanim Ullah, Dr Hariharan Srikanth, Dr Robert Hoy, Dr. Ivan Oleynik, Dr Xiaomei Jiang, and Dr. Denis Karaiskaj. They have been helpful in guiding my graduate studies. I also thank the physics department staffs Candice Pietri, Mary Ann, Daisy Matos, Jimmy Suarez, Miguel Nieves, James Kersey and James Christopher for their help.

I am very grateful to my lab member Chinta Mani Aryal for his continuous support, inspiration and being a great friend. I am indebted for his help with some of the experimental parts in this dissertation.

I also thank my family members for their continuous support and encouragement. My sincere gratitude goes to all my teachers and friends who had been a part of my life and inspiring all the times.

Last but not the least, I thank my wife Nabina Subedi, for her selfless support and my daughter Archisa for making this journey even more purposeful.

## TABLE OF CONTENTS

List of Tables .....	iii
List of Figures .....	iv
List of Abbreviations .....	vii
Abstract .....	ix
1.Introduction.....	1
1.1 Cell membrane .....	1
1.2 Bacterial membrane .....	4
1.3 Model lipid membrane systems .....	5
1.3.1 Black lipid membranes .....	5
1.3.2 Lipid monolayers .....	6
1.3.3 Liposomes .....	7
1.3.4 Supported lipid bilayer.....	8
1.4 Compounds used in the studies.....	9
1.4.1 Peptidomimetics E107-3.....	9
1.4.2 Colistin.....	11
1.4.3 N-BAR Endophilin amphiphilic helix H0 .....	12
1.2 Motivation for studies .....	13
1.3 Dissertation overview .....	14
2.Experimental setup.....	16
2.1 Introduction.....	16
2.2 Experimental approach .....	16
2.2.1 Permeability experiment .....	16
2.2.2 GUV experiment.....	25
2.2.3 AFM experiment.....	30
2.2.4 Bacterial studies .....	39
2.3 Conclusion .....	40
3.Peptidomimetic E107-3 Effect in Model Lipid Bilayer.....	41
3.1 Introduction.....	41
3.2 Results.....	43
3.2.1 Calcein leakage .....	43
3.2.2 Micropipette aspiration of GUVs.....	46
3.2.3 Solution atomic force microscopy .....	47
3.2.4 AFM-based force spectroscopy .....	52
3.2.5 Double-bilayer structure in the presence of calcium ions.....	58

3.4 Discussion .....	61
3.5 Conclusions .....	67
4. Interaction of Colistin with LPS Containing Bilayer and <i>E. coli</i> .....	69
4.1 Introduction .....	69
4.2 Results .....	73
4.2.1 Vesicle leakage .....	73
4.2.2 AFM experiment on planar lipid bilayers .....	76
4.2.3 Morphological changes induced by colistin in <i>E. coli</i> .....	79
4.3 Discussion .....	81
4.4 Conclusions .....	85
5 Pore Formation induced by Amphipathic Helix H0 of Endophilin BAR Domain on Planar Lipid Bilayer .....	86
5.1 Introduction .....	86
5.2 Results .....	88
5.2.1 Endophilin helix H0 in neutral bilayer .....	89
5.2.2 Endophilin BAR helix H0 in negatively charged bilayer .....	90
5.2.3 Endophilin BAR helix H0 with POPC/ cholesterol bilayer .....	90
5.2.4 Time course effect on POPC/Cholesterol .....	91
5.3 Discussion .....	92
5.4 Conclusion .....	95
6. Conclusions and Future Directions .....	96
6.1 Conclusion .....	96
6.2 Future Studies .....	97
7. References .....	98
Appendix A: List of Publications .....	124
Appendix B: Copyright Permissions .....	126

## LIST OF TABLES

Table 1-1 Main model membranes and techniques of study .....	9
Table 3-1 Concentration-dependent effect of E107-3 on lipid bilayer nanomechanics. ....	57

## LIST OF FIGURES

Figure 1.1 An updated Fluid—Mosaic Membrane Model that contains information on membrane domain structures and membrane-associated cytoskeletal and extracellular structures.....	2
Figure 1.2 Image of a typical phospholipid (POPC) which is found in the mammalian cell membrane. ....	3
Figure 1.3 The bacterial cell wall. ....	4
Figure 1.4 Images of model experimental lipid system.....	6
Figure 1.5 Images of common lipid model membrane systems used for the experimental purpose.....	7
Figure 1.6 A design of peptidomimetics containing reduced amide (A).....	10
Figure 1.7 Chemical structure of colistin.....	11
Figure 1.8 Human endophilin-A1 BAR domain.....	12
Figure 2.1 Structure of POPC, POPG, POPE, and cholesterol.....	18
Figure 2.2 Chemical structure of lipopolysaccharide (LPS) from pseudomonas aeruginosa.....	19
Figure 2.3 ÄKTA Pure FPLC system from General electronics.. ....	20
Figure 2.4 Schematics for preparing and separating dye encapsulated unilamellar vesicles (ULVs).....	21
Figure 2.5 FP-8300 spectrofluorometer (A) and schematics for the pathway of the spectrofluorometer (B).....	23
Figure 2.6 Structure of calcein disodium salt (A).....	26
Figure 2.7 Structure of melittin.....	28
Figure 2.8 Micropipette aspiration setup.. ....	29
Figure 2.9 Schematics of the working of AFM. ....	31

Figure 2.10 Image of multimode AFM from Bruker.....	32
Figure 2.11 Peakforce QNM mode scanning process.....	36
Figure 2.12 MaxQ 8000 incubator used to grow E.coli bacteria.....	39
Figure 3.1 Time-course measurements of the fluorescence enhancement of calcein-enclosed POPC/POPG ULVs exposed to different concentrations of E107-3 (A). .....	44
Figure 3.2 Fluorescence spectra of calcein-enclosed ULVs incubated with different concentrations of E107-3 for ~20 hours (1). .....	45
Figure 3.3 Real-time response of an aspirated POPC/POPG GUV exposed to 5 $\mu$ M E107-3. ....	46
Figure 3.4 Solution AFM height images of a POPC/POPG bilayer exposed to incremental concentrations of E107-3: 0 $\mu$ M (A), 5 $\mu$ M (B), 20 $\mu$ M (C), and 100 $\mu$ M (D).. .....	48
Figure 3.5 Solution AFM height images of a POPC/POPG bilayer exposed to 5 $\mu$ M E107-3 for different amount of times.....	49
Figure 3.6 Solution AFM height image of a POPC/POPG bilayer before (A) and after (B) being exposed to 0.4 $\mu$ M melittin.. .....	50
Figure 3.7 Height- weighted pair distribution functions $G(r)$ for a POPC/POPG bilayer exposed to different concentrations of E107-3. ....	51
Figure 3.8 Schematic of an AFM-based force spectroscopy measurement as the tip approaches a planar lipid bilayer (A). .....	53
Figure 3.9 Force-separation curves of a POPC/POPG bilayer exposed to incremental concentrations of E107-3. ....	55
Figure 3.10 Probability distributions of force-separation curves shown in Figure 3.9. ....	57
Figure 3.11 Solution AFM height image of a POPC/POPG bilayer in 5 mM $\text{CaCl}_2$ and 10 mM HEPES pH 7.4. ....	59
Figure 3.12 A POPC/POPG bilayer treated with 50 $\mu$ M E107-3 in the presence of 5 mM $\text{CaCl}_2$ . (A).....	60
Figure 3.13 A schematic diagram of bilayer disruption induced by E107-3. ....	65
Figure 4.1 Vesicle leakage induced by colistin as a function of the peptide concentration .....	73
Figure 4.2 Solution AFM images of an LPS/POPC 1:60 bilayer before (a) and after (b) exposure to 10 $\mu$ M colistin.....	74

Figure 4.3 Solution AFM images of an LPS/POPC 1:60 bilayer before (a) and after (b) exposure to 10 $\mu$ M colistin; solution AFM images of an LPS/POPC 1:30 bilayer before (c) and after (d) exposure to 10 $\mu$ M colistin. ....	75
Figure 4.4 Solution AFM images of an LPS/POPC 1:30 bilayer exposed to 5 $\mu$ M (a) and 10 $\mu$ M (b) colistin. ....	76
Figure 4.5 Solution AFM images of an LPS/POPC 1:30 bilayer in 5 mM MgCl <sub>2</sub> before (a) and after (b) exposure to 5 $\mu$ M colistin. ....	77
Figure 4.6 E.coli before adding colistin ( a), after adding 1 $\mu$ M (b) and 5 $\mu$ M colistin (c) for 30 minutes.....	78
Figure 4.7 E.coli after adding 1 $\mu$ M colistin and incubated for 1hr (a) and for 4 hours (b). ....	79
Figure 4.8 Morphology of E.coli after incubated with 5 $\mu$ M colistin for 1hr (a), 2hrs (b), and 4hrs (c).....	80
Figure 4.9 A schematic diagram depicting the proposed mechanism of colistin-induced clustering of LPS molecules in mica-supported planar bilayers. ....	84
Figure 5.1 Mica supported lipid bilayers incubated with helix H0 of endophilin. ....	88
Figure 5.2 POPC/POPG bilayer treated with different concentration of endophilin helix H0.....	90
Figure 5.3 POPC/Chol. bilayer treated with endophilin helix .	
Figure 5.4 Time dependent effect of helix 0 on POPC/Chol bilayer.....	92
Figure 5.5 POPC/POPE bilayer exposed to 0.5 $\mu$ M helix H0 concentration (a) and POPC bilayer with 2 $\mu$ M helix H0 concentration (b). ....	94

## LIST OF ABBREVIATIONS

AFM	Atomic Force Microscopy
ULV	Unilamellar Vesicle
MLV	Multilamellar Vesicle
SUV	Small Unilamellar Vesicle
GUV	Giant Unilamellar Vesicle
MA	Micropipette Aspiration
POPC	1-Palmitoyl-2-Oleoyl-sn-glycero-3- Phosphocholine
POPG	1-Palmitoyl-2-Oleoyl-sn-glycero-3-Phosphoglycerol
POPE	1-Palmitoyl-2-Oleoyl-sn-glycero-3-Phosphatidylethanolamine
LPS	Lipopolysaccharides
SEC	Size-Exclusion Chromatography
FPLC	Fast Protein Liquid Chromatography
Chol	Cholesterol
SPM	Scanning Probe Microscopy
PSPD	Position Sensitive Photo Detector/Diode
PF-QNM	Peak Force-Quantitative Nano Mechanical
FTIR	Fourier Transform Infrared spectroscopy
DPPE	1,2-Dipalmitoyl-sn-glycero-3-Phosphatidylethanolamine
SLB	Supported Lipid Bilayer

OM	Outer Membrane
MDR	Multidrug-Resistant
DAB	Diaminobutyric Acid
HEPES	4-(2Hydroxyethyl)-1-Piperazineethanesulfonic Acid
BLM	Black Lipid Membrane
AMP	Antimicrobial peptides

## ABSTRACT

Understanding the cellular membrane interaction with membrane active biomolecules and antimicrobial agents provides an insight in their working mechanism. Here, we studied the effect of antimicrobial agents; a recently developed peptidomimetics E107-3 and colistin as well as the N-terminal helix H0, of Endophilin A1 on the lipid bilayer.

It is important to discern the interaction mechanism of antimicrobial peptides with lipid membranes in battling multidrug resistant bacterial pathogens. We study the modification of structural and mechanical properties with a recently reported peptidomimetic on lipid bilayer. The compound referred to as E107-3 is synthesized based on the acylated reduced amide scaffold and has been shown to exhibit good antimicrobial potency. This compound increases lipid bilayer permeability as indicated by our vesicle leakage assay. Micropipette aspiration experiment shows that exposure of GUV to the compound causes the protrusion length  $L_p$  to spontaneously increase and then decrease, followed by GUV rupture. Solution atomic force microscopy (AFM) is used to visualize lipid bilayer structural modulation within a nanoscopic regime. This compound induces nanoscopic heterogeneous structures rather than pore like structures as produced by melittin. Finally, we use AFM-based force spectroscopy to study the impact of the compound on lipid bilayer's mechanical properties. With the incremental addition of this compound, we found the bilayer puncture force decreases moderately and a 39% decrease of the bilayer area compressibility modulus  $K_A$ . To explain our experimental data, we propose a membrane interaction model encompassing disruption of lipid chain packing and extraction of lipid molecules. The later action

mode is supported by our observation of a double-bilayer structure in the presence of fusogenic calcium ions.

Polyanionic Lipopolysaccharides LPS are important in regulating the permeability of outer membrane (OM) of gram-negative bacteria. To initiate the bactericidal activity of polymyxins, it is essential to impair the LPS-enriched OM. Here, we study the mechanism of membrane permeability caused by colistin (Polymyxin E) of LPS/phospholipid bilayers. Our vesicle leakage experiment showed that colistin binding enhanced bilayer permeability; the maximum increase in the bilayer permeability was positively correlated with the LPS fraction. Addition of magnesium ions abolished the effect of LPS in enhancing bilayer permeabilization. Solution atomic force microscopy (AFM) measurements on planar lipid bilayers shows the formation of nano- and macro clusters which protruded from the bilayer by ~2nm. Moreover, increasing the fraction of LPS or colistin enhances the formation of clusters but inhibits by magnesium ions addition. To explain our experimental data, we proposed a lipid-clustering model where colistin binds to LPS to form large-scale complexes segregated from zwitterionic phospholipids. The discontinuity (and thickness mismatch) at the edge of LPS-colistin clusters will create a passage that allows solutes to permeate through. The proposed model is consistent with all data obtained from our leakage and AFM experiments. Our results of LPS-dependent membrane restructuring provided useful insights into the mechanism that could be used by polymyxins in impairing the permeability barrier of the OM of Gram-negative bacteria.

Also, we studied the effect of helix H0 of a membrane modification inducing protein endophilin, on planar bilayer. We obtained transmembrane defects on the bilayer when scanned with AFM.

## 1. INTRODUCTION

### 1.1 Cell membrane

Membrane bounds cells and cell organelles. This membrane, also known as the plasma membrane, serves as a physical barrier to preserve the cytoplasm, protect from the toxic materials and pathogens, mediate activities to pass between extracellular environment and cells, and separate metabolic activities conducted within cells. Most of the cellular processes are directed by the gradient of charges and concentration across the membrane. The membranes are composed of lipids with embedded proteins, including peripheral, membrane, and transmembrane. The thickness of the membrane is variable due to the presence of these proteins. However, the apical plasma membrane purified from rat hepatocytes is found to be ~4.2nm [1] The membrane also acts as a site for attachment of cell wall, glycocalyx, and the cytoskeleton. Lipids are arranged in the bilayer with asymmetrical leaflets and comprise up to 50% by weight of the membrane. The phospholipid is the most abundant lipid found in the biological mammalian membranes. The outer leaflet of the mammalian plasma membrane mostly consists of choline phospholipids whereas inner leaflet has predominantly amino phospholipids (PS and PE) [2]. The plasma membrane also contains cholesterol in a significant amount which modulates the membrane fluidity. The arrangement and composition of the membrane adjust constantly to maintain fluidity and effect of the surrounding environmental changes. The model attributing the dynamic nature of a membrane is best described by a fluid mosaic which was first formulated by Singer and Nicolson in 1972 [3]. This model is able to describe several cellular features related to the cell membrane. A sketch of the cell membrane described by this model is shown in Figure 1.1

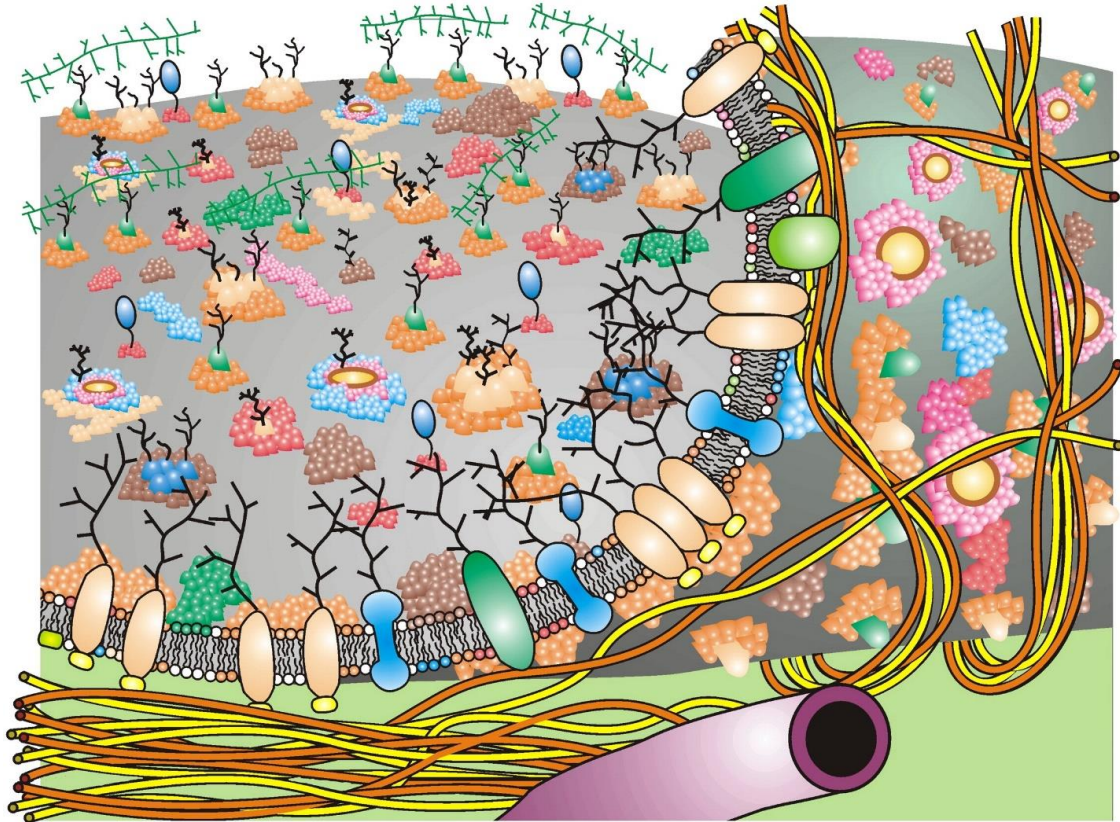


*Figure 1.1 An updated Fluid—Mosaic Membrane Model that contains information on membrane domain structures and membrane-associated cytoskeletal and extracellular structures. Different integral proteins, glycoproteins, lipids and oligosaccharides are represented by different colors, and where the membrane has been peeled-up to view the inner membrane surface cytoskeletal fencing is apparent that restricts the lateral diffusion of some but not all trans-membrane glycoproteins. Other lateral diffusion restriction mechanisms are also represented, such as lipid domains, integral membrane glycoprotein complex formation (seen in the membrane cut-away), polysaccharide–glycoprotein associations (at the far top left) and direct or indirect attachment of inner surface membrane domains to cytoskeletal elements (at lower left). Although this figure suggests some possible integral membrane protein and lipid mobility restraint mechanisms, it does not accurately present the sizes or structures of integral membrane proteins, cytoskeletal structures polysaccharides, lipids, submicro- or nano-sized domains or membrane-associated cytoskeletal structures or their crowding in the membrane Image adapted form [4].*

The design of the biological membrane to function in a complex environment where two distinct aqueous compartments are separated by the intricate hydrophilic-hydrophobic interface is the root problem to study them [5]. Thus, a simpler experimental model is used to study the

properties of the cell membrane. A membrane with single phospholipid or a mixture of few component lipids is used for a lot of studies. Having Amphiphilic characteristic of lipid forces it to self-aggregate in different structures. Depending upon the lipid structure, lipid-lipid interaction and preparation environment, they form micellar aggregates, lamellar and non-lamellar liquid crystalline phase of different topology [6, 7]. In fact, the self-assembly and organization of the lipids are carried out by relatively weak forces comparative to thermal energy [8]. The enthalpy component of the free energy arises from most central interactions like hydrogen bonding, Van Der Waals bonding, and electrostatic interaction while the entropic component originates from the thermal motion responsible for keeping lipid in fluid in motion[9].

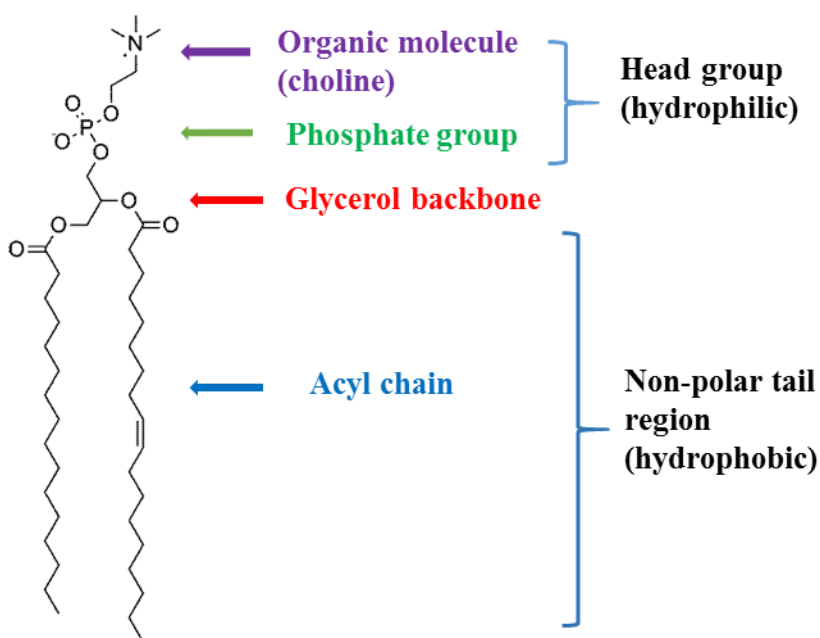


Figure 1.2 Image of a typical phospholipid (POPC) which is found in the mammalian cell membrane. Image adapted from[10]

In aqueous solution with amphiphilic molecules, the subtle competition between enthalpic and the entropic forces represents the tendency to exclude the water molecules from a nonpolar

molecule which leads to minimizing the free energy,  $F=E-TS$ . This leads to the self-aggregation of the lipid molecules to sealed compartments in such a way that the contact of water molecules restricts with the polar region of the lipids [9].

## 1.2 Bacterial membrane

The cell envelope of the bacteria is made of an inner plasma membrane and the rigid cell wall. The plasma membrane is similar to the eukaryotic cell membrane mostly consisting of lipids like phosphatidylethanolamine, phosphatidylglycerol, and cardiolipin [11]. The presence of a cell wall in a bacterial cell is essential to protect protoplast from the mechanical damages and withstand large turgor pressure.

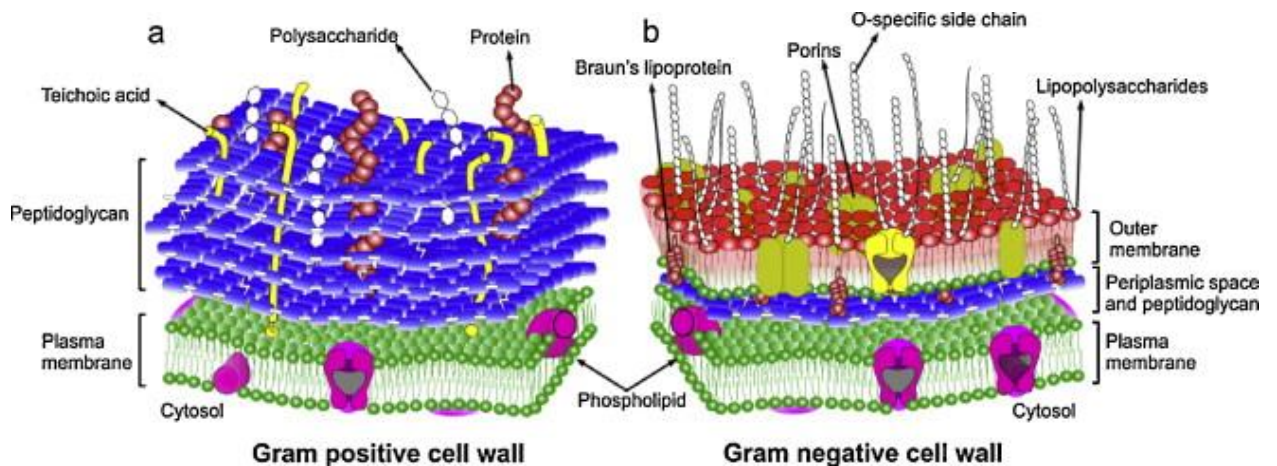


*Figure 1.3 The bacterial cell wall. The Gram-positive envelope (a). The Gram-negative envelope (b). In Gram-positive bacteria, the lipidic plasma membrane with embedded proteins is covered by a multilayered peptidoglycan shell decorated with polysaccharides, teichoic acids, and proteins. In Gram-negative bacteria, a thin peptidoglycan layer surrounds the plasma membrane and is covered by an asymmetrical outer membrane containing lipopolysaccharides, which lies on the peptidoglycan layer. Image adapted from [12]*

The cell wall of gram positive-bacteria (g+) consists of the thick layer (around 15-80nm) of peptidoglycan, also known as murine. Peptidoglycans are polymers of disaccharides (glycan)

which are linked by a short chain of amino acids (peptides). Teichoic acid, unique to the gram-positive cells, runs perpendicular to the layers of peptidoglycan. Lipoteichoic acids, which are anchored to the cell membrane, has its function related to growth, physiology, and development of bacterial cell [13]. Wall teichoic acids are covalently bonded with a peptidoglycan layer which is involved in cell division and maintaining the shape of the cell[14].

Gram-negative bacteria (g-) cell wall is composed of one or a few layers of peptidoglycan encompassed by an outer membrane (OM). Peptidoglycan layer sits on the periplasmic fluid between OM and the cell membrane. The OM is highly asymmetric; inner leaflet has lipid composition similar to the inner membrane, and outer leaflet consists of lipopolysaccharides (LPS) [11]. LPS are made of repeating unit of O-antigen, core region and Lipid A. LPS can hinder the entrance of the drugs making the cell resistance towards them [15]

### **1.3 Model lipid membrane systems**

The difficulty of achieving an exact replica of the cell membrane guides to preparing some simple model membranes. Some of the experimental model membranes used for research purposes are described below.

#### **1.3.1 Black lipid membranes**

This is one of the oldest model lipid-membrane systems, which was first described by Mullers et.al. [16]. A thin aperture (order of few hundred micrometers) on hydrophobic support like Teflon or polyethylene separates the two compartments with aqueous solutions. A mixture of phospholipids in the relatively viscous hydrophobic solvent like hexane or decane is painted across this small opening on the support. Monolayers of lipid are formed instantly at the interface of the aqueous/organic solvent droplet. As the wall of the opening is hydrophobic, the solvent migrates

towards it leaving the monolayer to fuse together with thinning at the center and leaving annulus at the perimeter. A more uniform bilayer is prepared by pre-forming the lipid monolayer on one side of the chamber in an aqueous solution and slowly lowering the solution level. This process forms a single monolayer. The second monolayer of lipid is formed by pulling up the solution and completes the bilayer [17] (Figure 1.4A) Electrodes can be placed at both sides of the bilayer compartments to conduct the electrical measurement and patch clamping.

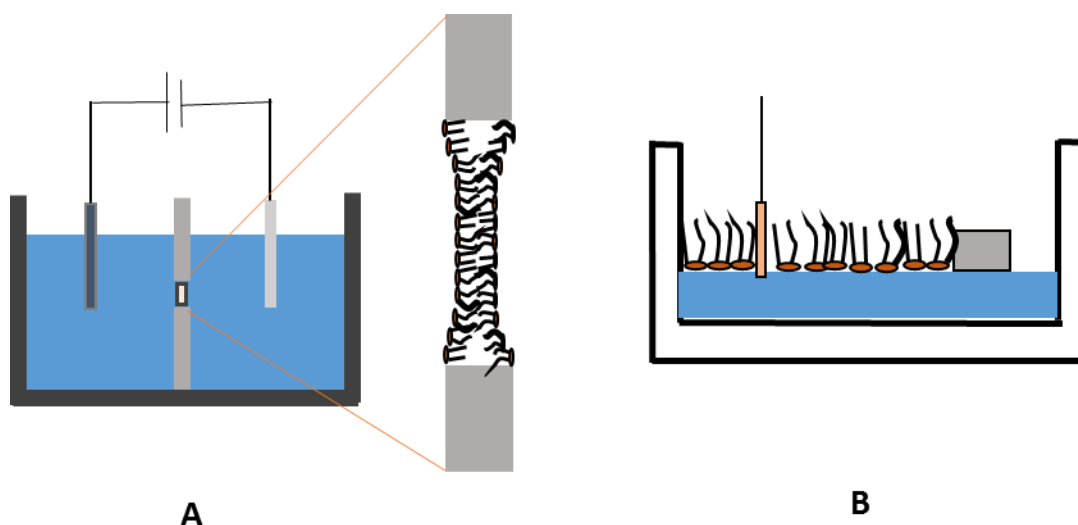
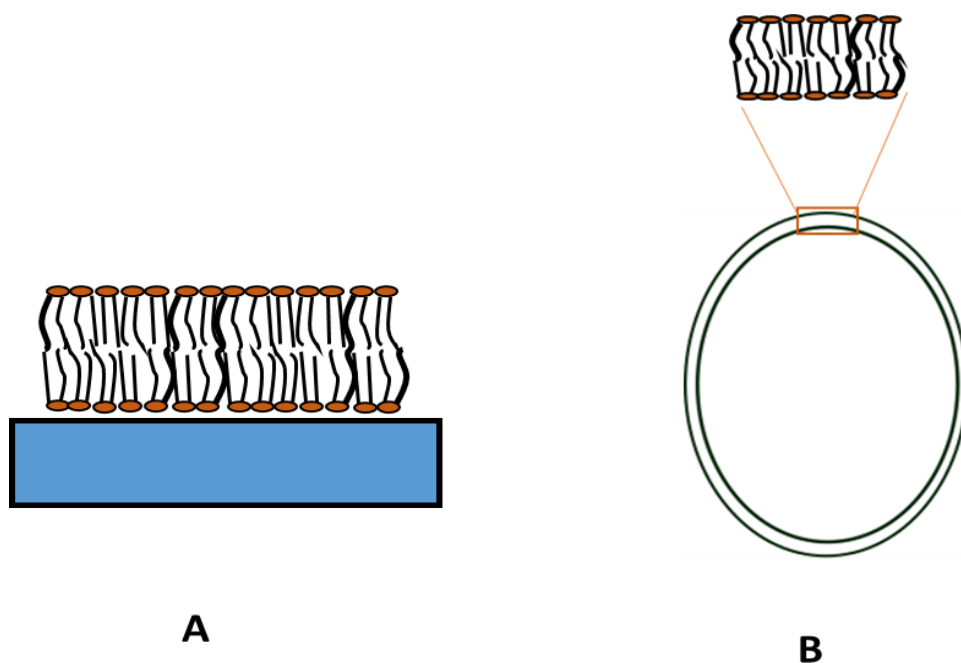


Figure 1.4 Images of model experimental lipid system. Black lipid membrane (BLM) (A) and Langmuir monolayer (B)

### 1.3.2 Lipid monolayers

The half of a bilayer or monolayer is a monomolecular film formed at the air-water interface and is obtained by spreading lipid molecules on the surface of an aqueous solution (Figure 1.4 B). The lipid solution dissolved in a highly volatile organic solvent is deposited on the water surface in a trough. The organic solvent evaporates leaving the hydrophilic head group of lipid in contact with an aqueous solution and hydrophobic hydrocarbon chain pointing in the air. Monolayers are used to extract isotherm characteristics, which are obtained from surface pressure

as a function of area per molecule and are used to characterize the nature of phase separation. In addition, so formed monolayers can be transferred to a smooth solid surface by Langmuir-Blodgett (LB) or Langmuir-Schaefer techniques to obtain supported lipid bilayer. The former transfer method uses vertical deposition whereas the latter uses the horizontal lifting of the monolayer. This technique provides a very strong platform to study the intra-and intermolecular interaction at interfaces [18]



*Figure 1.5 Images of common lipid model membrane systems used for the experimental purpose. Supported lipid bilayers (SLB)(A) and Liposomes (B).*

### **1.3.3 Liposomes**

Liposomes are the simplest model mimicking a closed, natural cell membrane of organisms (Figure 1.5B). They are small artificial sphere shaped vesicles, which are developed from one or more lipid components, mostly the non-toxic phospholipids. Liposomes are classified as multilamellar vesicles (MLVs) consisting of several lamellae lipid bilayer and unilamellar vesicles

(ULVs) consisting of a single lipid bilayer lamella. Further, depending on the size, unilamellar vesicles are classified as small unilamellar vesicles (SUVs, < 100 nm in diameter), large unilamellar vesicles (LUVs, < 1000 nm in diameter), giant unilamellar vesicles (GUVs, > 1000 nm in diameter) [19]. Depending upon the lipid components used, the charge of the lipid component, size, and methodology for the preparation, the properties of liposomes vary considerably. Liposomes are used to study membrane interaction events, thermodynamic, structural, and mechanical properties of the cell membrane. In recent years, the use of liposomes is extensive as carriers for drugs and cosmetics due to its biocompatibility nature [20]. Entrapment of hydrophilic and lipophilic drugs inside and within the lamella has made liposomes an excellent vehicle for drug delivery [21].

#### **1.3.4 Supported lipid bilayer**

Supported lipid bilayers are the surface-confined model system with flat bilayers prepared on top of the firm substrate like mica, silica, glass, etc. (Figure 1.5A). They can be prepared by depositing lipid monolayers on a hard surface by langmuir deposition techniques, vesicle fusion on the hydrophilic surface or self-assembled by rehydrating spin coated lipid surface[22] [19]. Solid-supported lipid bilayer formation by vesicle fusion includes two critical steps i) adhesion and rupture of liposomes on the substrate forming patches and ii) formation of a complete bilayer by subsequent evolution of bilayer patches[23]. One way of incorporating protein in the supported bilayer is achieved by using a polymer cushion for the bilayer formation [24]. These models are mostly used to study the interaction of drugs and proteins with membranes along with phase behavior and molecular organization. There are several techniques and instruments to study a variety of properties using model membranes.

The following table includes some of the methodologies used depending upon the model membrane.

*Table 1-1 Main model membranes and techniques of study*

<b>Model membranes</b>	<b>Main techniques of study</b>
<i>Langmuir monolayers at air-water interface</i>	
Bidimensional stems with planar geometry	Surface pressure-area isotherms
Ideally smooth, uncorrugated substrate	Brewster angle microscopy
Temperature and surface controlles	Fluorescence microscopy
Ion content and pH of the subphase controlled	X-ray or neutron reflectivity, grazing incidence X-ray or neutron scattering
<i>Liposomes</i>	
Giant Unilamellar Vesicles(GUVs): geometry and dimensions close to that of cells	Scattering techniques: quasi-elastic light scattering, small angle X-ray (or neutron) scattering, wide-angle X-ray scattering
Temperature controlled	Cryo-transmission electron microscopy, fluorescence microscopy
Ion content and pH of the aqueous phase controlled	Spectroscopic techniques: UV-visible, Fluorescence, Raman, NMR Differential scanning calorimetry (DSC)
<i>Supported monolayers or bilayers</i>	
Stability and well-defined geometry of the membrane (planar or spherical for bilayers)	Atomic Force Microscopy (AFM), Fluorescence microscopy
Asymmetric bilayers possible	X-ray or neutron reflectivity, grazing-incidence X-ray or neutron scattering
Stacks of parallel bilayers possible	
Ion content and pH of the aqueous phase controlled	Quartz crystal microbalance (QCM-D), surface plasmon resonance (SPR), UV-vis sum-frequency generation (SFG), second harmonic generation(SHG)

Table adapted from [25]

## **1.4 Compounds used in the studies**

### **1.4.1 Peptidomimetics E107-3**

The increase of resistance towards drugs during the treatment of infectious diseases is an alarming global threat to which thousands of people give lives yearly. Particularly the bacterial pathogens, which have developed the antibiotic resistance, have grown up as superbugs. In addition, the resistance of drugs for the treatment of malaria [26], human immunodeficiency virus/acquired immune deficiency syndrome (HIV/AIDS), tuberculosis [27], and many cancers

[28] are reported. This promotes the seeking of diseases' treatment with alternative drugs and methodologies. Antimicrobial peptides (AMPs) are one class of promising agents in the treatment of drug-resistant bacteria and have a large spectrum of activity. However, these molecules have limitation regarding prone to proteolysis, short half-lives, etc. A slight modification in the structure of these AMPs produces more stable and potent antimicrobial compounds, which are known as peptidomimetics.

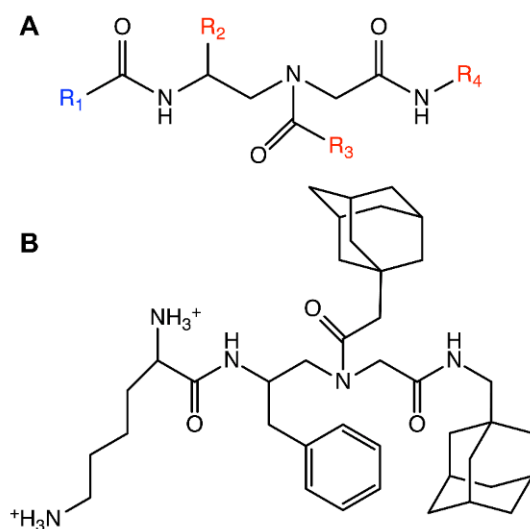


*Figure 1.6 A design of peptidomimetics containing reduced amide (A). The blue colored side group  $R_1$  is positively charged; the red colored side groups  $R_2$ ,  $R_3$ , and  $R_4$  are hydrophobic. (B) The chemical composition of the antimicrobial E107-3 based on the scaffold shown in (A).  $R_2$  contains a phenyl ring, and  $R_3$  and  $R_4$  each contains an adamantyl group. At neutral pH, the two amines at  $R_1$  position are likely positively charged.*

A group of such peptidomimetics is reduced amide derivatives, which has an amide bond reduced on the backbone of  $\alpha$ -peptide. This reduction of the amide bond to produce secondary amine bond has significantly increased the stability against proteolytic degradation activity. One such library of compounds is synthesized in Dr. Jianfeng Cai's group in the Department of Chemistry, USF. These compounds have four side chain of which R1 exhibits hydrophilic nature,

and the rest side chains are hydrophobic. One lead compound referred to E107-3 with a molecular weight of ~660 is used for observing the changes imparted on the membrane bilayer. The two amines at R1 position of E107-3 are likely to exhibit positively charge at neutral pH.

### 1.4.2 Colistin

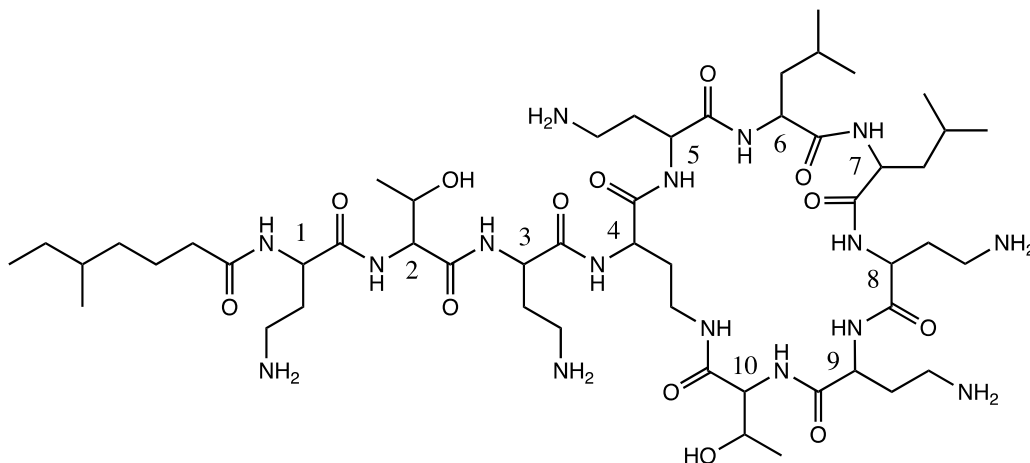


*Figure 1.7 Chemical structure of colistin. The amphipathic peptide is composed of a heptapeptide macrocycle, an exocyclic tripeptide, and an acyl tail. Colistin has two hydrophobic domains, including the acyl chain and the hydrophobic patch of the macrocycle at positions 6 and 7. Cationic diaminobutyric acids are located at positions 1, 3, 5, 8, and 9.*

Colistin is a cyclic lipopeptide belonging to polymyxin family, which possesses antimicrobial activity against gram-negative microbes. It consists of the heptapeptide ring of polymyxins enriched with cationic diaminobutyric acid (DAB). The C-terminus of the exocyclic tripeptide is fused to the macrocyclic ring, while the N-terminus is linked to a fatty acid tail (prominently 6-methyl-octanoic acid). Colistin was first isolated from the Gram-positive bacterium *Bacillus colistinus* and was used for clinical application since the 1950s. Due to observed nephrotoxicity and neurotoxicity accompanied by colistin administration on patients, its practice was gradually receded. However, due to the development of Multi-drug resistance species,

it has generated a new interest due to its antimicrobial activity and low susceptibility against bacteria [29].

### 1.4.3 N-BAR Endophilin amphiphilic helix H0

Endophilin is a BAR (Bin/Amphiphysin/Rvs) protein associated with sensing and inducing membrane curvature during the process of endocytosis. It consists of a banana-shaped dimeric structure with identical three helices coupled together. The N-BAR endophilin consists of additional helix H0 at the N-terminal. For the dissertation work, we used N-terminal helix H0 of human endophilin A1 which consists of 24 amino acids.

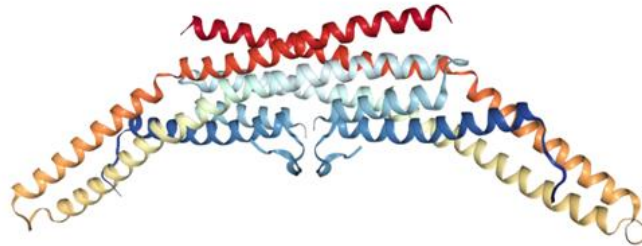


*Figure 1.8 Human endophilin-A1 BAR domain. Image adapted from PDB with id:1ZWW and reference [30]*

The amino acid sequence of this helix 0 is MSVAGLKKQFHKATQKVSEKVGGA. This helix H0 rearranges to form an amphiphilic helix coil when it comes in contact with membrane and inserts into the membrane. However, controversial results have been published earlier regarding the role of this helix in sensing and inducing membrane curvature.

## 1.5 Motivation for studies

This dissertation aims for the model membrane interaction studies with a member of peptide mimics E107-3, antimicrobial lipopeptide colistin and a membrane curvature-inducing fragment of Endophilin BAR domain.

The preliminary study of the bacteria treated with E107-3 indicated that it induces permeability of propidium iodide to the membrane, a signature of compromising bacterial membrane.[29]. This indicates the possibility of this compound to be a potential antimicrobial agent that acts by targeting and damaging bacterial membranes. Membrane damage induced by AMPs can proceed with different mechanisms, such as pore formation and detergent-like membrane disintegration [31]. During the process of membrane disruption, structural change and modulation in mechanical properties can occur. This work is motivated to elucidate the mechanical and surface changes that occur on the model lipid membrane induced by the peptidomimetics E107-3.

Polymyxins have grown a renewed interest in the treatment of multidrug-resistant species. The activity of polymyxin is believed to be related to the impairment of LPS on the outer membrane (OM) of bacterial cells. To study the interaction of the OM of bacterial cells with polymyxin several LPS containing vesicular system or monolayers has been employed but only limited studies on the planer model. Previous two AFM studies on planar bilayer with Polymyxin were based on Lipid A and on a cushioned monolayer of biotinylated LPS. This limited work on AFM based planar bilayer containing LPS with polymyxin motivated for this study. This study is inspired to detail the nano-scale morphological changes impaired by colistin (Polymyxin E), and the role of divalent cations on its effectiveness with LPS containing planner bilayer using AFM.

Endophilin BAR domain protein is related to curvature sensing and generation as well as recruiting other proteins for the endocytosis in cells. An amphiphilic N-terminal helix H0 is believed to anchor the membrane and help to generate membrane curvature. Earlier research based mostly on the curvilinear membrane or computational work has resulted in controversial outcomes regarding curvature formation by helix H0. Planar membranes are sometimes an excellent model for the peptide's interaction studies. No such studies on planar membrane based upon AFM with helix H0 have been conducted earlier. This study is motivated to decipher the modulation on surface topography induced by helix H0 on planar bilayer made of different lipid composition.

## **1.6 Dissertation overview**

This dissertation work focuses on the study of the molecular interaction of biomolecules with the model lipid membranes.

Chapter 2 describes the materials and methods implemented for the whole study. This includes the drugs and peptides, lipids and instruments used for the studies.

Chapter 3 deals with the study of a reduced amide scaffold based antimicrobial peptidomimetics E107-3 with the model bilayer. Permeability of ULVs and the kinetic response of GUVs with exposure of E107-3 is described in this chapter. Surface modulation of the supported bilayer in the presence of the peptide mimics is imaged by using a solution AFM. A comparison with a well-known pore-forming antimicrobial peptide melittin is also performed.

Chapter 4 details the interaction study of colistin with a lipid bilayer containing lipopolysaccharides (LPS). It deals with the change in membrane structure introduced in a bilayer with different LPS content due to the effect of colistin. A detail permeability behavior is studied

using leakage experiment as well as atomic force microscopy (AFM). The effect of a divalent cation on the permeability of LPS containing bilayer is also a part of the study.

Chapter 5 deals with the study of a membrane curvature promoting amphipathic helix H0 of the endophilin BAR domain on the supported bilayer. Transmembrane defects promoted by the N-terminal helix H0 are visualized by AFM in topographic images.

Chapter 6 deals with the conclusion and future work.

## **2. EXPERIMENTAL SETUP**

### **2.1 Introduction**

Lipid bilayers along with liposomes of different sizes and supported lipid bilayer (SLB) were used for the experimental purpose. We used giant unilamellar vesicles (GUVs) for micropipette aspiration experiment and unilamellar vesicles (ULVs) of smaller size for the permeability experiment. For the preparation of supported lipid bilayers, we used small unilamellar vesicles (SUVs). We also used a gram-negative species of bacteria, *E.coli* for the experiment.

In this chapter, we describe the experimental procedure for the preparation of the samples and the methodology for the experimental purpose. In addition, we discuss some of the theoretical backgrounds for those approaches.

### **2.2 Experimental approach**

#### **2.2.1 Permeability experiment**

A commonly used experimental approach to investigate the leakage through the model lipid membrane is permeability experiment. Permeability experiment is conducted by measuring the amount of fluorescence markers that leaked from the dye encapsulated unilamellar vesicle due to the addition of the compound of interest. Commonly used markers for such experiments are self-quenching dyes like carboxyfluorescein and calcein. Generally, unilamellar vesicles, which are encapsulated with the markers, are incubated with the compounds of interest. These compounds might compromise the membrane and induce leakage of the marker from the enclosure. This release process can occur in two ways: i) graded process in which the vesicles

release portions of their loadings or ii) all-or-none in which some fractions of the vesicles release all of their loadings or none at all [32]. The emission intensity due to the dequenching of fluorescence dye after releasing from vesicles measures the leakage. Other approaches to measuring the leakage include chromatographic separation [33], fluorescence correlation spectroscopy [34], etc.

### **2.2.1.1 Unilamellar vesicles preparation and calcein encapsulation**

1-palmitoyl-2-oleoyl-sn-glycero-3-phosphocholine (POPC) was purchased from either Avanti Polar Lipids (Alabaster, AL) or NOF America. 1-palmitoyl-2-oleoyl-sn-glycero-3-phosphoglycerol (POPG), 1-palmitoyl-2-oleoyl-sn-glycero-3-phosphoethanolamine (POPE), and cholesterol were purchased from Avanti Polar Lipids (Alabaster, AL). Stock solutions for these lipids were prepared with chloroform or chloroform: methanol mixture (3:1 ratio). Melittin purified from bee venom was purchased from Thermo Fisher Scientific (Waltham, MA). E107-3 was synthesized using solid phase synthesis method [29] by Dr. Jianfeng Cai's group at the department of chemistry, USF, FL. Calcein disodium salt and lyophilized LPS powder were purchased from Sigma-Aldrich. LPS was phenol extracted from *Pseudomonas aeruginosa* whose source strain is ATCC 27316. A stock solution of LPS was prepared in ultrapure water.

Dry lipid films were prepared in glass test tubes by mixing appropriate ratios of lipid stock solutions. Around 1- 4mg of total lipid content was used for vesicle preparation. Organic solvents were removed by a gentle stream of nitrogen gas using a 12-position N-EVAP evaporator (Organomation Associates, Inc., Berlin, MA). The samples were further dried by vacuum pumping for ~1 hour. The obtained lipid films were hydrated in 1ml 30 mM calcein and 10 mM 4-(2-hydroxyethyl)-1-piperazineethanesulfonic acid (HEPES) at pH 7.4 (now onwards known as buffer A).

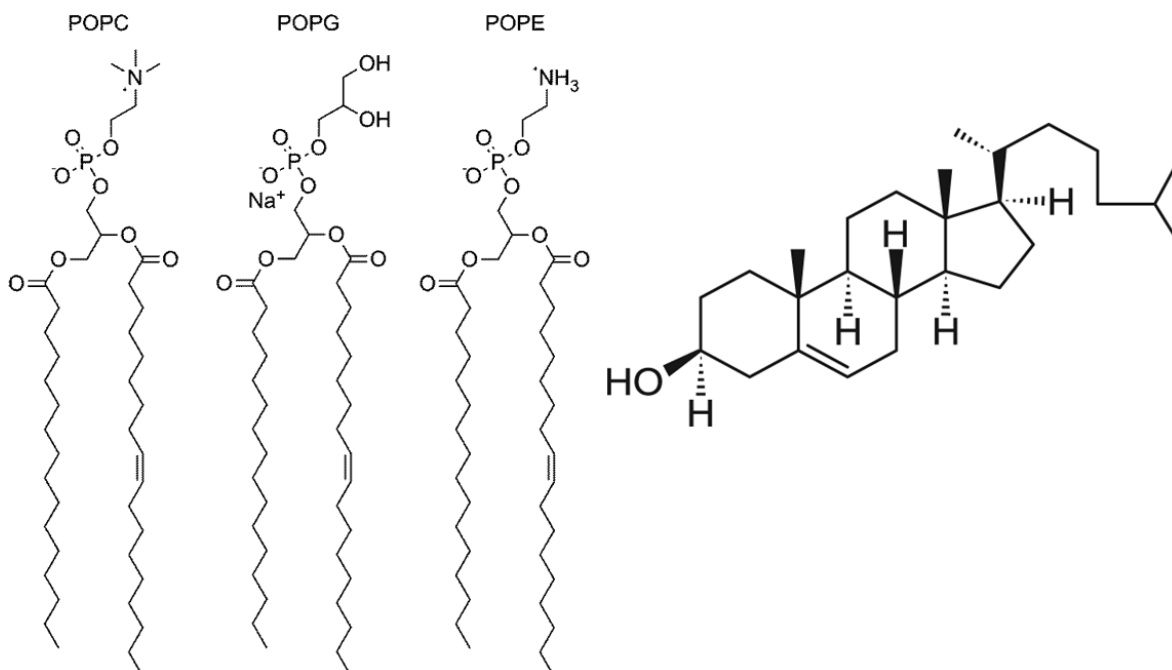


Figure 2.1 Structure of *POPC*, *POPG*, *POPE*, and *cholesterol*. Images are adapted from [10] and Avanti polar lipids

For LPS-containing samples, an appropriate amount of an LPS stock solution (in water) was mixed with lipid suspension during the hydration process (total volume 1ml). We prepared unilamellar vesicles by two methods:

- i) Freeze-thaw cycles between  $-80^{\circ}\text{C}$  and  $50^{\circ}\text{C}$  were carried out to ensure uniform distribution of calcein across the multilamellar vesicles (MLVs). The resultant lipid solution was extruded using an Avanti mini-extruder outfitted with a 100 nm diameter pore filter to produce ULVs.
- ii) Qsonica cup-horn powered by a Fisher brand model 705 sonic Dismembrator was used to prepare calcein-enclosed unilamellar vesicles (ULVs) with LPS. The output power of the sonicator was set at 50% and the total sonication time was 20 min (1-min on and 30-sec off)

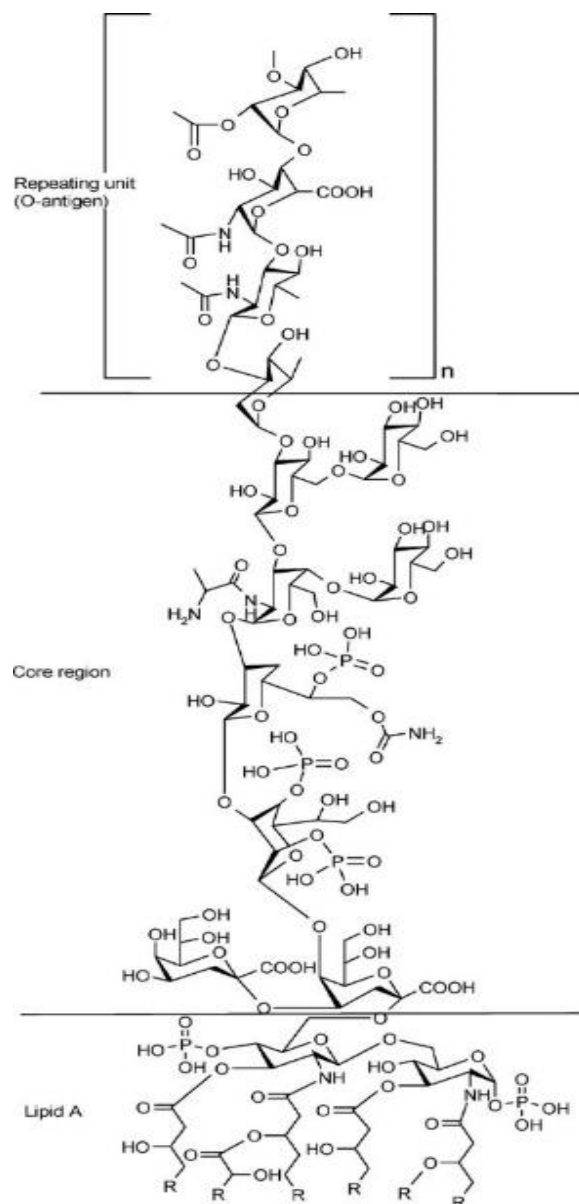
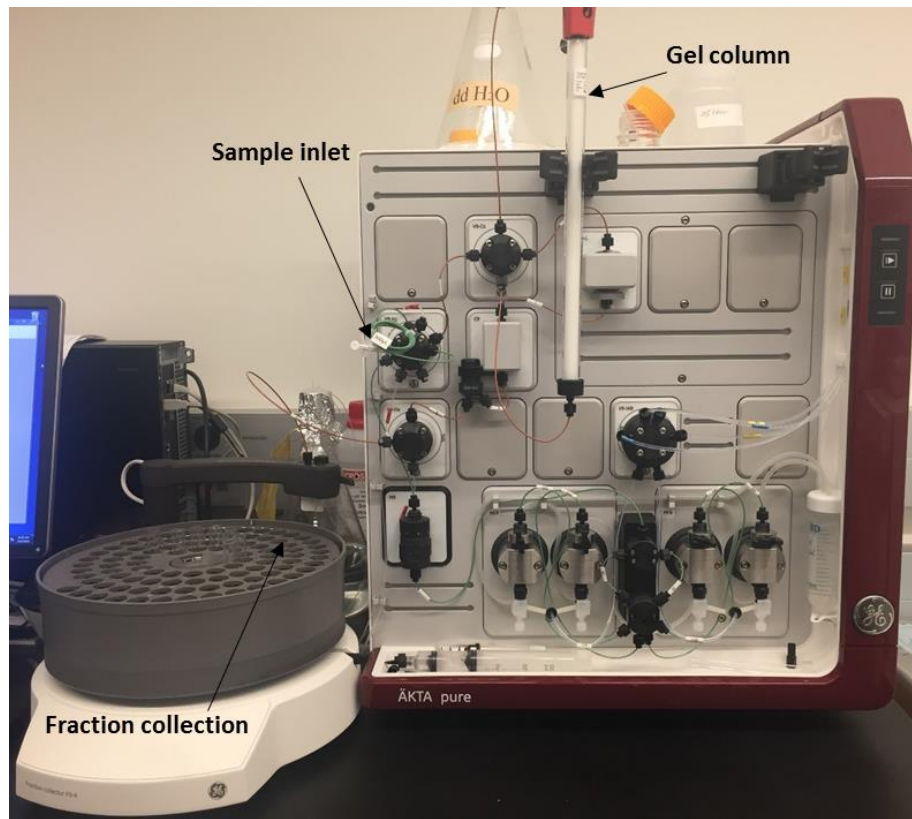


Figure 2.2 Chemical structure of lipopolysaccharide (LPS) from *pseudomonas aeruginosa*. Figure adapted from [35]. Lipid A, core region, and repeat unit of O- Antigen region are distinguished in figure.

External calcein was removed by using an ÄKTA Pure FPLC (GE Healthcare) and a gel filtration column (Superdex 200,10/300GL). The elution buffer contained 45 mM NaCl and 10 mM HEPES (pH 7.4) (now onwards known as buffer B). The vesicles' portions were fractionated by monitoring UV absorption at 280 nm.

### 2.2.1.2 Removal of calcein via SEC column on ÄKTA FPLC

Size exclusion chromatography (SEC) is a chromatographic technique used to separate the solute from a solution depending upon its size or often molecular weight. Based on the elution buffer used to transport sample on the column, it is referred to as gel filtration when the aqueous buffer is used and gel permeation when an organic solvent is used.



*Figure 2.3 ÄKTA Pure FPLC system from General electronics. The gel column is shown in the figure above fractionates the solutes based on the size or the molecular weight of the sample which is collected in rotatory fraction collection.*

Since we prepared calcein encapsulated unilamellar vesicles in an aqueous medium, we used gel filtration column to separate the ULVs from non-entrapped calcein solution. This Superdex 200,10/300GL gel column has an exclusion limit for globular proteins ( $M_r$ ) of

approximately  $1.3 \times 10^6$ . The composites of cross-linked agarose and dextran with an average particle size of  $13 \mu\text{m}$  are packed in this column to form the bed. These composites consist of spherical porous particles, which have none or minimal chemical and physical interaction. Initially, the bed is filled with elute buffer, which covers the pores of matrix and spaces between the particles. The stationary phase liquid inside the matrix is in equilibrium with the mobile phase liquid outside of the particles. When the solution passes through the column, the molecules with small size diffuse into the pores of spherical beads, which retard the flow of these particles. The size of the solute entering the matrix determines the depth of diffusion within the matrix. These molecules travel slower depending upon the degree of diffusion in the matrix. Large molecules are excluded from the porous matrix and make an uninterrupted flow, which is faster than the small molecules diffused in the matrix.

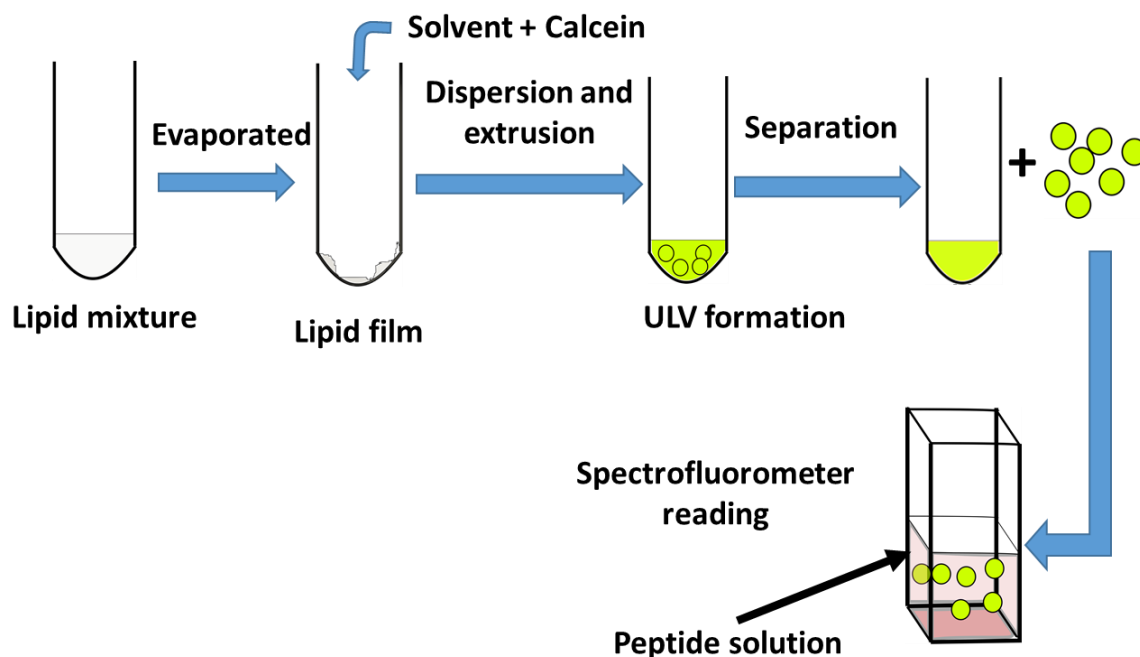


*Figure 2.4 Schematics for preparing and separating dye encapsulated unilamellar vesicles (ULVs). Calcein dye molecules are encapsulated in the ULVs used for dye leakage experiments.*

In our experiment, the size of the calcein encapsulated ULVs are much larger than the calcein molecules. Thus, calcein molecules are entrapped inside the gel due to diffusion whereas the ULVs elute faster through the column, which is collected earlier during fractionation.

### **2.2.1.3 Fluorescence reading Experiment**

To monitor the leakage of the calcein, FP-8300 spectrofluorometer (Jasco Analytical Instruments, Easton, MD) was used. This device has continuous output Xe arc lamp with shielded lamp housing having excitation and emission wavelength range of 200-750 nm. Solution samples are filled in a quartz cuvette and placed in Peltier thermal cell holder (Model EHC-813).

#### **2.2.1.3.1 Working of Spectrofluorometer**

Spectrofluorometry, which is also known as fluorescence spectroscopy or fluorometry, is a type of analytical technique that can measure, record, and analyze fluorescence from the sample. It is able to record both excitation and emission spectra. The main components of spectrofluorometer consist of a light source, excitation monochromatic filter, sample holder, emission monochromatic filter and a detector.

The Xenon lamp light source in our spectrofluorometer emits light from 200nm-750nm. Before reaching the sample, the light passes through the excitation monochromatic filter that blocks the entire source wavelength except the specified excitation wavelength. This monochromatic light passes through the sample placed on the holder (cell cuvette) and is absorbed by the fluorophore.

The absorption of the appropriate wavelength ( $\lambda_A$ ) light excites the electrons of the fluorophore from the ground state to the excited state with higher energy and vibrational energy state within the order of femtosecond ( $10^{-15}$  sec). The excited electrons will rapidly ( $10^{-12}$ sec) lose its energy by internal conversion like vibrational relax to the lowest energy singlet excited state.

This lowest energy singlet excited state electrons are able to relax back to the ground state by emitting a photon of higher wavelength ( $\lambda_F$ ). This shift towards larger wavelength for emission light is called Stokes shift. This emission continuous as long as the excitation sources and fluorophores are present.

The emitted light is passed through the emission monochromatic filter preferably selected at the wavelength of highest emission intensity for particular fluorophore. This filter is positioned at a right angle to the path from the incident excitation source. This geometry reduces the possible interference of emission light with transmitted excitation light. The light passing through this filter reaches the detector, which measures and quantifies the fluorescence value of emitted light and also fluorescence signature of a fluorophore.

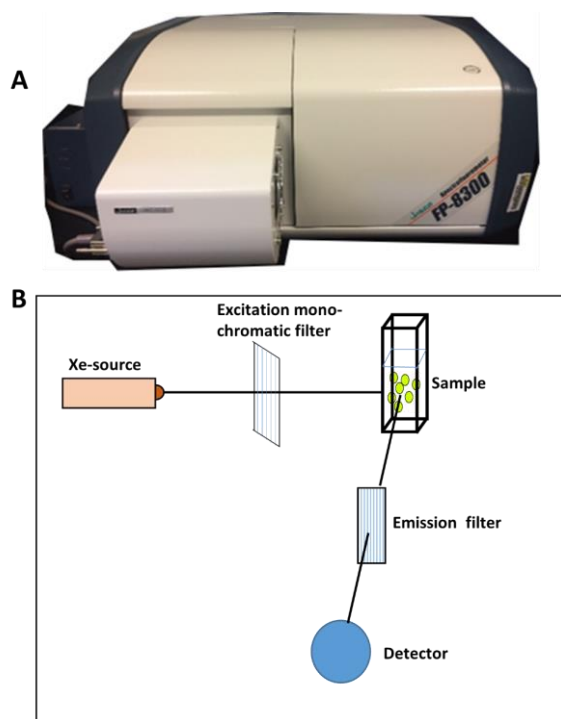


*Figure 2.5 FP-8300 spectrofluorometer (A) and schematics for the pathway of the spectrofluorometer (B). The light emitted from the source passes through monochromatic filter, which excites the fluorophore, and the light emitted ray from the fluorophore passing through emission monochromatic filter is collected in detector*

We studied the vesicle leakage by two methods:

**i) Time course**

For kinetic calcein leakage study (23°C), an aliquot of E107-3 or melittin stock solution (in buffer B) was diluted with buffer B to make a final volume of 1990  $\mu\text{L}$ . The solution was transferred to a 3-mL quartz cuvette placed in a Peltier thermal cell holder of the spectrofluorometer. A small magnetic rod was used to stir the solution (300 rpm). Right before each measurement, 10  $\mu\text{L}$  of calcein-enclosed POPC/POPG(9:1) ULVs prepared by method (i) was pipetted into the cuvette. Time-course fluorescence intensity was collected every 0.5 or 1.0 sec for fast kinetics, and 1.0 min for slow kinetics. To alleviate photobleaching, the excitation gate was closed between data points for 1.0-min-interval measurements. The obtained fluorescence intensity was calibrated by the maximum intensity ( $I_{\text{max}}$ ) when complete leakage occurs.  $I_{\text{max}}$  is determined by adding 200  $\mu\text{L}$  of 200 mM Triton X-100 (in buffer B) to 10  $\mu\text{L}$  ULV stock and 1790  $\mu\text{L}$  buffer B.

**ii) Steady-state fluorescence**

Steady-state fluorescence spectroscopy measurements were performed for 10  $\mu\text{L}$  POPC/POPG(9:1) ULV stock solutions incubated with different concentrations of E107-3 and melittin with the volume of 1990  $\mu\text{l}$  for about ~20 hours. Maximum fluorescence intensity of the sample was determined by adding 200  $\mu\text{l}$  of 200 mM Triton X-100 (in buffer B) to 10  $\mu\text{l}$  ULV stock and 1790  $\mu\text{L}$  buffer B.

Similarly, for the vesicles containing different amount of LPS, 30  $\mu\text{l}$  of calcein encapsulated ULVs were added to the 970  $\mu\text{l}$  colistin solution of different concentration prepared in buffer B. To obtain maximum vesicle leakage, the colistin solution was substituted with the nonionic surfactant Triton X-100 (final concentration of 20 mM). The vesicle-colistin mixtures

were incubated in the dark for 20 h. These samples were transferred to a quartz cuvette and placed in the cell holder to measure the emission spectrum.

For both of the methods, the excitation wavelength used was  $494 \pm 2.5$  nm. The emission spectrum was measured from 500 to 600 nm (bandwidth of 2.5 nm). Three measurements were performed for each sample. The maximum intensity at 515 nm of the emission spectrum was used for vesicle leakage evaluation. Fluorescence enhancement (FE) or Vesicle leakage % was calculated using the following equation:

$$\text{Leakage \%} = (I - I_0) / (I_{max} - I_0) \times 100\%, \quad (2.1)$$

$$\text{Fluorescence Enhancement (FE)} = \frac{I(t) - I_0}{(I_{max} - I_0)} \times 100\% \quad (2.2)$$

Where  $I_0$  is the fluorescence intensity of control vesicles,  $I_{max}$  is the fluorescence intensity of vesicles treated with Triton X-100, and  $I$  is the fluorescence intensity of vesicles treated with different concentrations of agents and  $I(t)$  is the fluorescence intensity at each time step for time course experiment.

### **2.2.2 GUV experiment**

The other method that we used for our experiments is using giant unilamellar vesicles (GUV). We prepared GUVs and used them for micropipette aspiration experiments to obtain the change in membrane property as an effect of E107-3.

#### **2.2.2.1 GUV preparation**

GUVs were produced by the electroformation method [36]. A mixture of 0.2 mg POPC/POPG (10:1) and 1.0 mol% Rh-DPPE (total volume of 200  $\mu$ L in chloroform/methanol 3:1) was deposited onto two ITO coated glass slides. Organic solvents were removed by vacuum

pumping for >1 h (2-stage, 5 CFM). A Viton O-ring was placed between the two slides to form a GUV production chamber, which was filled by 500  $\mu$ L 100 mM sucrose.

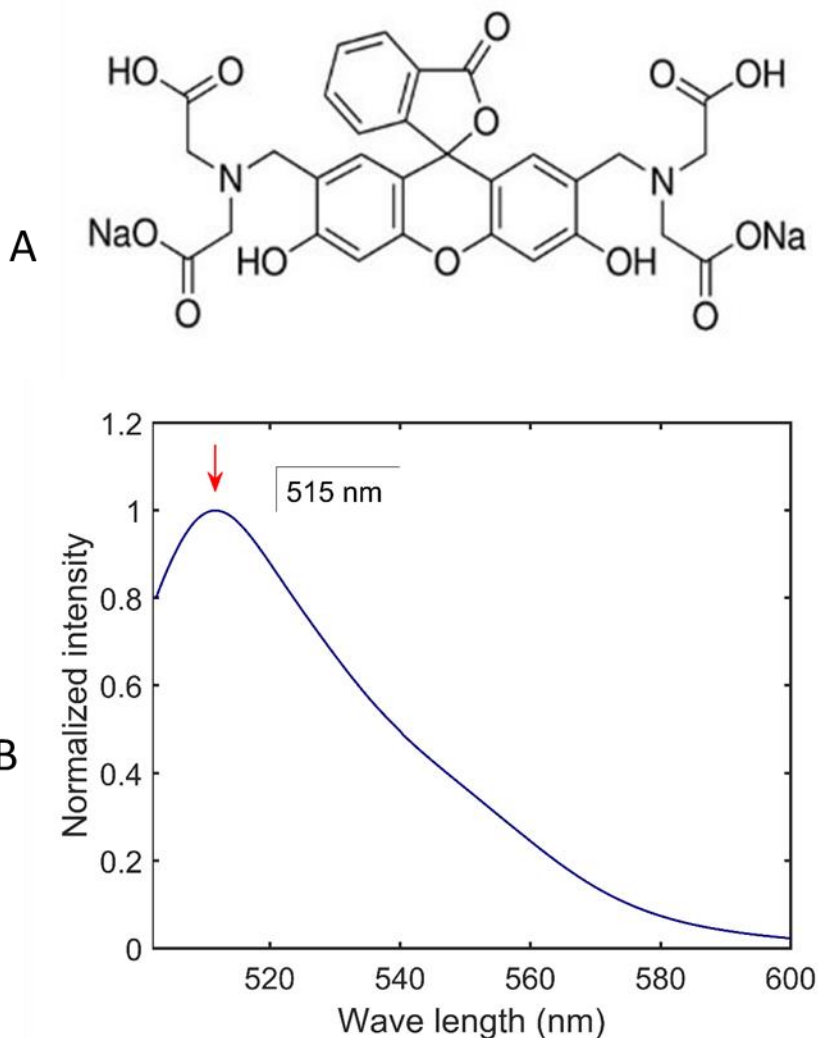


Figure 2.6 Structure of calcein disodium salt (A). Image is adapted from [37]. The emission spectrum of calcein molecules leaked from POPC vesicles obtained by treating with surfactant. The emission intensity peaks at 515 nm (B)

The two slides were clamped together, inserted into a homemade aluminum block, and heated to 60°C using a Digi-Sense temperature controller (Cole-Parmer). An AC field of 10 Hz and 2.0  $V_{pp}$  was applied to the heated assemblage for 2 h. After the AC field was turned off, the

assemblage was gradually cooled to room temperature (-5°C per hour controlled by the temperature controller). GUV solution was harvested and mixed with 3 mL of 100 mM glucose solution. After settling for ~30 min, GUV aliquot pipetted from the bottom was diluted with 100 mM glucose and used for aspiration experiment.

### 2.2.2.2 Micropipette aspiration (MA) experiment

We performed micropipette aspiration (MA) experiments to extract the mechanical properties of the GUV in presence of the peptidomimetics. This method provides the qualitative response of single vesicle, unlike permeability experiment that provides the global averaged response on the vesicles. This MA method was pioneered by Evans and Rawicz group, which employs an external mechanical force to probe vesicles deformity in the form of the aspiration length of GUV inside the micropipette. Such superficial pressure on the pipette(P), produces a uniform membrane tension ( $\tau_m$ ) on the vesicle, depending on the micropipette diameter and the diameter of the spherical section of the vesicles given by:

$$\tau_m = R_p P / 2 \left( 1 - \frac{2R_p}{2R_v} \right) \quad (2.3)$$

Where  $2R_p$  and  $2R_v$  are the diameter of the micropipette and the spherical portion outside of micropipette respectively. In addition, the length protrusion inside the micropipette is altered by either a change of temperature or pipette pressure or the effect of external agents. Whatsoever, the change in protrusion length ( $L_p$ ) is related to the change in area and volume which is given by:

$$\Delta A \approx \pi \left[ 2R_p \cdot L_p \cdot \left( 1 - \frac{R_p}{R_v} \right) + \frac{2\Delta V}{\pi R_v} \right] \quad (2.4)$$

However, the volume of the vesicles remains effectively constant for the area experiment, which approximates the second part of the above equation to zero [38, 39].

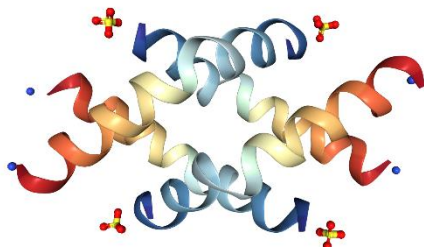


*Figure 2.7 Structure of melittin. PDB id is 2MLT*

### **2.2.2.3 Micropipette aspiration set up**

A micropipette was manufactured by pulling and polishing. Briefly, a 1-mm glass capillary was pulled by a Narishige PN-30 magnetic glass microelectrode horizontal puller (East Meadow, NY). The sharp end of the pulled capillary was cut and polished by a Narishige MF-900 microforge. For GUV aspiration, the capillary was typically cut at a position, so the resulting micropipette has an inner diameter of 10–20  $\mu\text{m}$ . The forged micropipette was inserted into a Narishige HI-7 injector holder, which was mounted to a motorized MP-225 micromanipulator (Sutter Instrument, Novato, CA). To control the pressure at the micropipette tip, we connected the injector holder to a silicone tubing filled with 100 mM glucose. The open end of the tubing was fixed to a motorized vertical translator (Velmex Inc., Bloomfield, NY).

The pressure at the micropipette tip was tuned by adjusting the height of the open end of the tubing. Our GUV aspiration experiment (23°C) followed the procedure reported by other groups [40-43]. Two wells were made by placing silicone sheets (Grace BioLabs, Inc.) on a glass

coverslip. The first well contained a diluted GUV solution ( $\sim 300 \mu\text{L}$ ), and the second well contained the desired peptide concentration in 100 mM glucose ( $\sim 200 \mu\text{L}$ ).

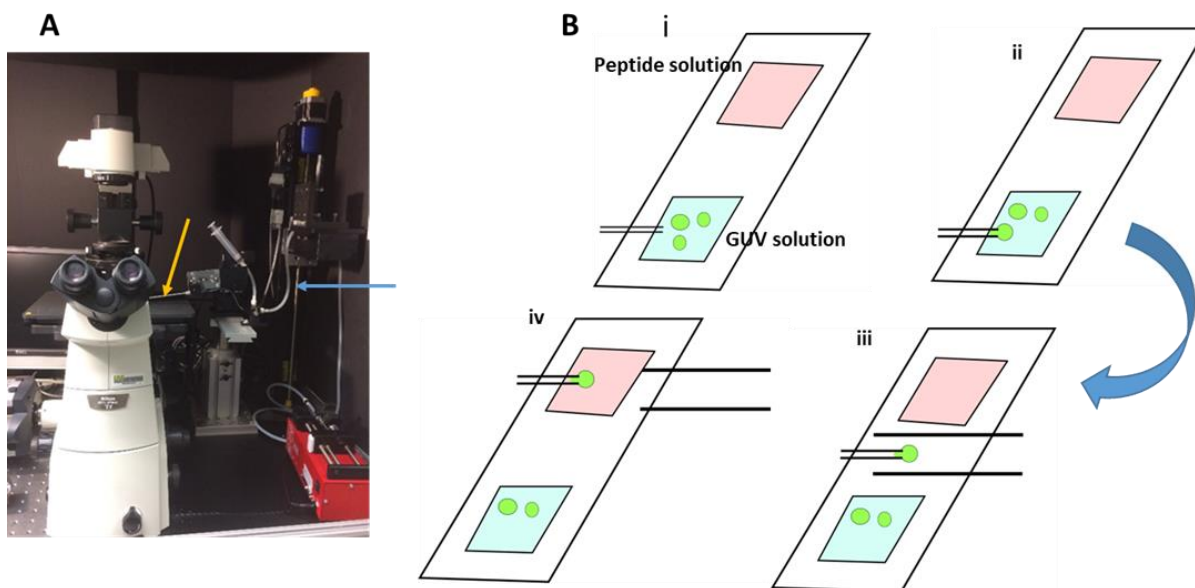


*Figure 2.8 Micropipette aspiration setup. The glass coverslip with attached silicon wafer wells is on top of Nikon inverted microscope (A). Blue arrow shows the tube filled with buffer liquid (glucose 200mM) for pressure adjustment and orange arrow points the micropipette holder. The transferring of single GUV to the peptide solution. (B). The steps include; micropipette is brought closer to GUV solution (i) single GUV is attached to the micropipette by applying negative pressure (ii), GUV containing micropipette covered with a transfer pipette and escort to peptide solution (iii), and removal of transfer pipette to expose aspirated GUV to the peptide solution (iv).*

The coverslip was mounted on an inverted Nikon Eclipse *Ti-U* fluorescence microscope (Nikon Instruments Inc., Melville, NY). The forged micropipette was inserted into the GUV well by using the motorized micromanipulator. A selected GUV was aspirated when there was a small constant negative pressure at the micropipette tip compared to the well solution. (The magnitude of the negative pressure was adjusted by moving the vertical translator.) To obtain the real-time effect of E107-3 on GUV area/volume properties, the micropipette with an aspirated GUV was inserted into a transfer-pipette (I.D. of 0.75 mm) filled with 100 mM glucose. The transfer-pipette

and the micropipette were simultaneously moved to the reaction well containing 5  $\mu\text{M}$  E107-3 in 100 mM glucose. The transfer-pipette was retracted from the micropipette using a manual micromanipulator (MM33, World Precision Instruments). The real-time response of the aspirated GUV to E107-3 was monitored by fluorescence video images acquired using a CFI Super Fluor ELWD 60 $\times$  Ph2 objective and an Andor EM-CCD camera (iXon Ultra 897). The exposure time for each video image was 50 ms, and the video frame rate was 2 Hz. To diminish the effect of water evaporation on osmolality imbalance, both the GUV well and the reaction well were refreshed every  $\sim$ 10 min.

### **2.2.3 Atomic Force Microscopy (AFM) experiment**

AFM is a scanning probe microscopy (SPM) which has the capability of detecting forces in single molecule level. Due to the possibility of operating in any environment, AFM has gained extensive attention in a wide area of research, including material characterizing [44, 45], biomedical[46], engineering. AFM has been an important tool for studying biological samples as it can provide close to physiological settings.

A general working diagram of an AFM is shown in Figure 2.9. It consists of a cantilever with an attached sharp tip, three-dimensional piezo scanner, laser system with a position sensitive photodetector (PSPD) and a controller for a feedback loop. The sample placed on the piezo scanner is brought in close proximity to the tip which develops the van der Waals force. As the tip approaches the surface, the long-range van der Waals force attracts the cantilever to the sample. However, when the tip is brought in contact with the sample, the short-range repulsive van der Waals force deflects the cantilever in the opposite direction. This motion in cantilever is recorded by the deflection of the laser beam reflected from the tip of the cantilever to a PSPD which is used to reconstruct topographical images as well as discern several other mechanical information. A

fluid-compatible Multimode 8 AFM (Bruker, Santa Barbara, CA) and a Nanoscope V controller were used for the studies. The components of the AFM is shown in Figure 2.10(A).

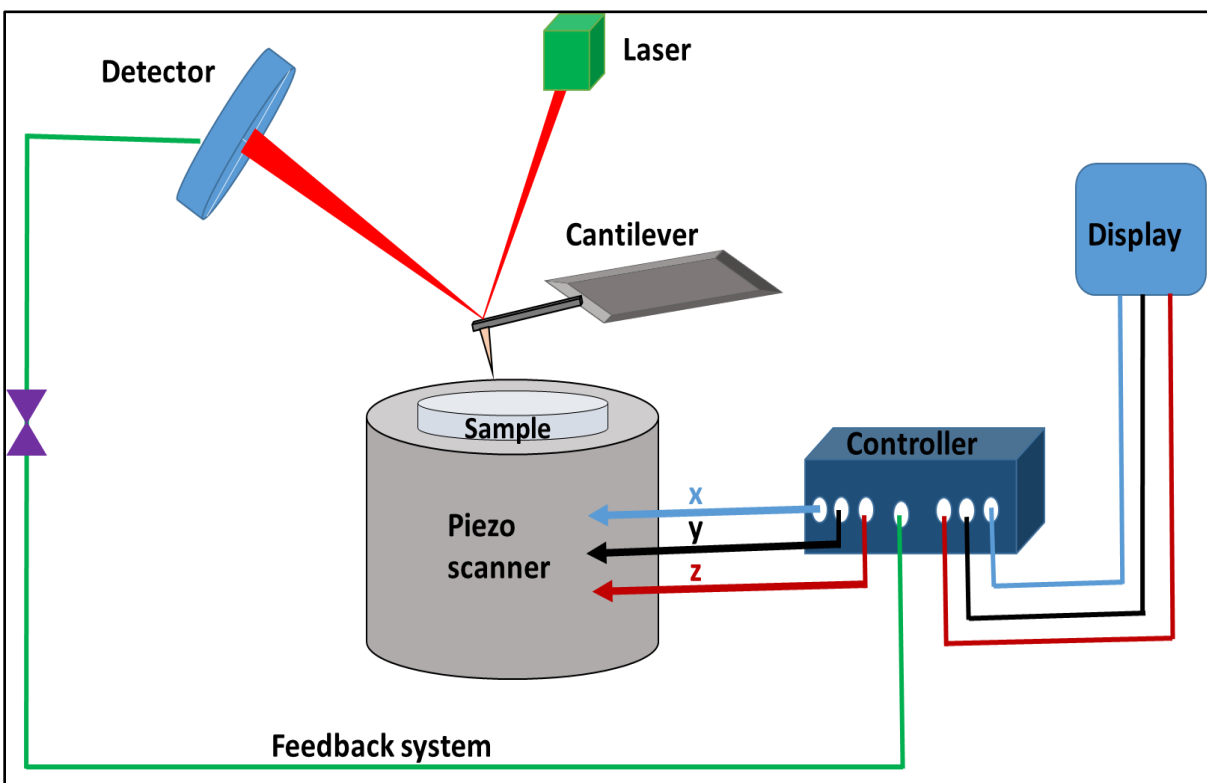


Figure 2.9 Schematics of the working of AFM. The laser beam is incident on the tip of the cantilever probe which might deflect while scanning. The position sensitive detector is very sensitive to detect the slight change in direction of a reflected laser beam off the cantilever. The controller processes the signals for display and provides appropriate feedback in the system.

### 2.2.3.1 Components of Multimode AFM Bruker

The main components of the AFM are similar for most AFM systems although they are placed in a different region of the system during set up. Here, we describe the main components of the multimode AFM from Bruker.

#### i) SPM system

SPM system in multimode AFM consists of the scanner, scanner support ring, and base. There are several scanners based on the need of scanning parameters like longer type ‘J’ scanners

and shorter type ‘A’ scanner. The longer type scanner provides a larger field of scan whereas shorter scanner scans smaller images but with higher resolution.

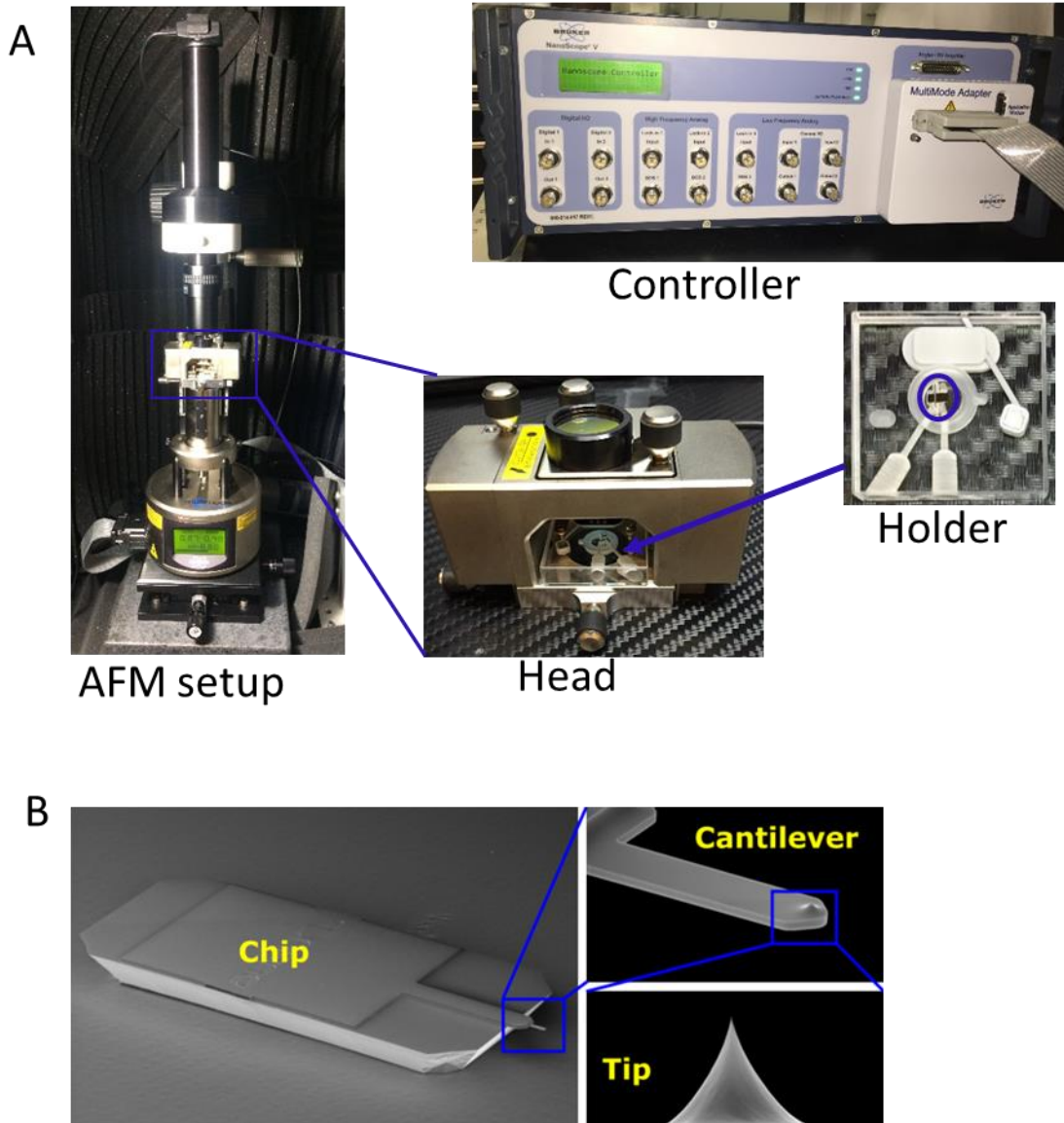


Figure 2.10 Image of multimode AFM from Bruker. The different components of AFM; setup, controller, head ,and holder are shown in (A).. The encircled region in holder is the position for holding the AFM probe. The enlarged view of the AFM probe(B). Adapted from [47]

These scanners consist of piezo crystal, which translates the stage or the probe as a response to the voltage supply. In our experiment, we used a longer type ‘J’ scanner to collect signals.

It also consists of a scanner support ring to attach the scanner and a base that has an LCD to display the detector parameters

#### **ii) Controller**

Controller of an AFM is to process the captured signal and provide the necessary feedback for the scanning purpose. The feedback system of the AFM is generated as a response to a deviation of signals from the constant set points like deviation/force or amplitude. In our system, we used the nanoscope V controller.

#### **iii) Head**

The head in multimode AFM consists of the laser source, probe holder attachment system, position sensitive photodetector (PSPD), and an attached XY-stage. The laser beam is incident to the cantilever probe in the probe holder which reflects and reaches the photodetector via tilt mirror. This photodetector consists of four elements. The differences of the signal between the sum of the top two elements (A) and the bottom two elements (B) is displayed as a vertical signal in a display of base. Similarly, the signal difference between the sum of left two (C) and the right two (D) is displayed as a horizontal signal [48]. Whereas, the total sum of the signals of all the four elements is displayed as ‘SUM’, which should be maximized during the setup.

#### **iv) Probe holder and probes**

The probe holder attaches the probe in position while scanning and taking measurements in AFM. Depending upon the mode of scan and sample type, the probe holder might be different. We used special fluid cell made of glass for most of the scanning as we scanned our samples in an

aqueous medium. In addition, a standard probe holder was employed for some measurement to perform in the air.

AFM probes consists of a sharp tip placed at the end of the cantilever, attached to the chip (Figure 2.10B). The radius of the tip ranges from a few nanometer to few tens of nanometer. Usually a beam cantilever or a V-shaped cantilever is attached to the chip whose deflection is recorded during AFM measurement.

### **2.2.3.2 Primary modes of Imaging**

#### **i) Static or Contact mode**

In this mode, the tip of the cantilever is in continuous physical contact with the sample at all the times while scanning either by keeping the force constant or the height above the sample constant. Cantilever deflection provides the feedback for this mode while operating in constant force while no force feedback is provided while operating in constant height mode. This mode can be useful for imaging the samples in the air which can handle high loads. Tip contamination, sample damage, tip damage, distorted images are some of the drawbacks of contact mode.

#### **ii) Non-contact mode**

In non-contact mode, the tip of AFM probe hovers 5-15 nm above the sample. Since the interacting forces are very weak to detect, the cantilever is provided with a small oscillation so that the change in frequency, amplitude or phase in oscillating cantilever due to force gradient with the sample occurs. These changes in cantilever are used to detect the sample properties. Low-resolution images and contamination on the sample surface limit the usage of non-contact mode.

#### **iii) Tapping mode**

This advanced hybrid mode of contact and non-contact mode scans the sample by alternatively placing the probe in contact with the sample and withdrawing off to prevent dragging.

The cantilever is oscillated at or near the resonant frequency during scanning with a constant amplitude provided by a feedback loop. When the oscillating cantilever approaches the sample, it loses its oscillation due to energy loss as it contacts the surface. This change in oscillation amplitude is used to map surface features and measure the surface property. Cantilevers used in fluid for tapping mode are generally soft  $< 1$  N/m, whereas more rigid cantilevers are used to operate in air mode (1-100 N/m).

### **2.2.3.3 PeakForce Quantitative Nanomechanics (PF-QNM)**

We used peakforce quantitative nanomechanics (PF-QNM) mode for all our experimental purpose. This mode accesses the high-resolution mechanical mapping of several sample properties with very little or no destruction of the sample or the tip. In peak force tapping mode, the probe and sample are brought together intermittently at a periodically modulated frequency by controlling the maximum force, called peak force, using a system feedback loop. This modulation frequency is well below the cantilever resonance frequency. At each period, the interaction force is measured directly by the deflection of the cantilever. This interaction force is converted to force-separation plots, which enable to determine several QNM information such as elastic modulus, tip-sample adhesion, energy dissipation, and maximum deformation. Such sample properties are extracted by fitting different regions of the calibrated force curve with corresponding models. For example, the reduced Young's modulus  $E^*$  is obtained from the retract curve region as shown in Figure 2.11(iv) using the Derjaguin, Muller, Toropov (DMT) model given by

$$F_{tip} = \frac{4}{3} E^* \sqrt{Rd^3} + F_{adh} \quad (2.5)$$

Where  $F_{tip}$  is the force on the tip,  $F_{adh}$  is the adhesion force,  $R$  is the tip end radius and  $d$  is the tip sample separation.

However, obtaining this information is limited to a single point of interaction in peak force tapping mode. PF-QNM system enables to acquire such information for each pixels of collected data and display to the corresponding image channels scanning across the sample [45, 46]. Although the maximum deflection of the cantilevers is held constant, the raised and the lowered feature of the sample surface influences the deflection and piezo position of the cantilever. By using a feedback loop to control the tip-height above the surface, and monitoring tip deflection for corresponding influences, topographic images of the samples are reconstructed.

This mode of operation does not require resonating the cantilever, eliminating the necessity of cantilever tuning, so it is particularly advantageous in scanning samples in solution.

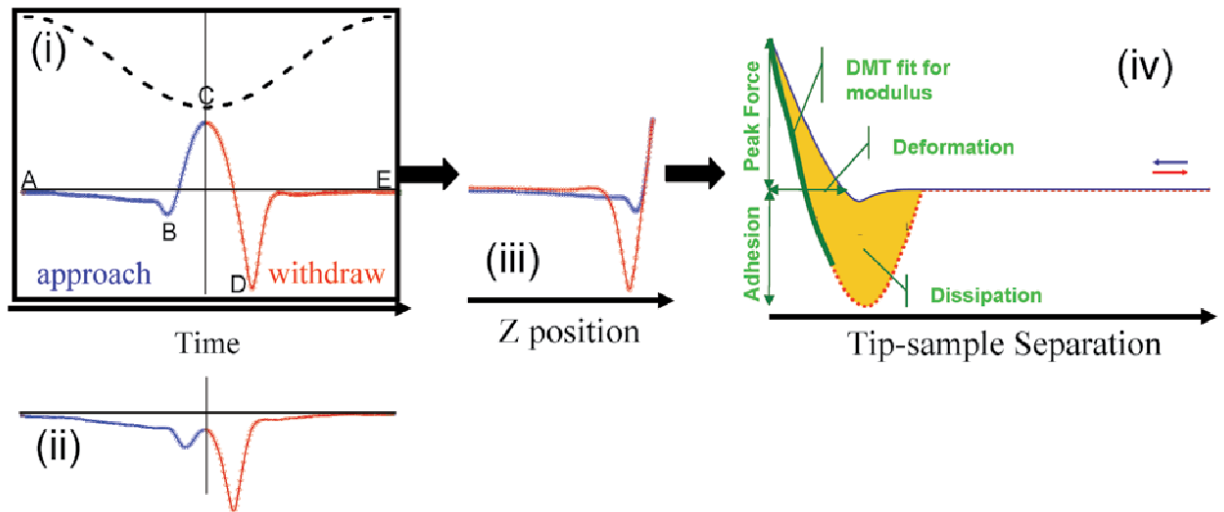


Figure 2.11 Peakforce QNM mode scanning process The force curve captured at each pixels are simultaneously converted to the mechanical properties based on the different regions of curves as shown in figure (iv). The images based on the properties are displayed in multi-channel display. Image courtesy of Bruker Nano Surfaces [48].

#### **2.2.3.4 Bilayer sample preparation**

The lipid mixtures were prepared by mixing the appropriate ratio of stock solutions in glass test tubes. Organic solvents were removed by a gentle stream of argon gas using a 12-position N-EVAP evaporator (Organomation Associates, Inc., Berlin, MA), and then vacuum pumped for >2 h. The resultant lipid films were hydrated in 10 mM HEPES pH 7.4. Small unilamellar vesicles (SUVs) are produced by ultrasonication using a Sonic Dismembrator (3-mm micro tip, a total duration of 10 min). To obtain LPS/POPC mixtures with different weight ratios, an appropriate volume of the LPS stock solution was added to the POPC film. The mixture was repeatedly vortexed and sonicated using a bath sonicator. The lipid suspension was later transferred to a 10-mL glass beaker. Additional ultrapure water was supplied to the beaker so that the final volume was ~5 mL. Small unilamellar vesicles (SUVs) were prepared using a Branson Ultrasonics Sonifier SFX 250 and a 10-mm flat tip. The obtained SUVs were centrifuged briefly before planar bilayer preparation to get rid of possible metal particles shredded from the sonicator tip. This obtained solution was injected into the fluid cell, spreading over freshly cleaved mica as a substrate, via a syringe pump.

Planar supported bilayer was formed after incubation of SUVs for 15-30 minutes by fusion. The excess SUVs were flushed out with the appropriate buffer solution.

Another approach was used to prepare the bilayer outside of the fluid chamber for helix H0 endophilin N-BAR domain experiments. Freshly cleaved mica was marked with a circle (6-8 mm diameter) at the center by a super pap pen liquid blocker from Ted Pella Inc. Redding, CA. The SUV solution (60-100  $\mu$ l) obtained after centrifugation was deposited within the marking in mica and the assemblage was placed on dry heat block at ~37°C for 10 minutes to prepare bilayer. The SUVs were attached and fused on the mica substrate which eventually coalesces to form a

uniform supported bilayer. The excess SUV solution was gently exchanged with ultrapure water (~80  $\mu$ l) using a pipette (8-10 times). Keeping the bilayer hydrated at all the times, the mica was transferred to the fluid chamber and replenished with appropriate buffer via a syringe pump.

### **2.2.3.5 Measurement process**

AFM was used to scan the topographic images and acquire the force curve as discussed below:

#### **2.2.3.5.1 Topographic**

Topographic images of the samples were acquired either by using ScanAsyst-Fluid+ with 2-nm tip or DNP-S10 probe with a nominal tip radius of 10 nm. Squared images were acquired at a scan rate of 0.5-1.0Hz. The maximum force or peak force was set at 300pN -400pN. After obtaining several control images, we inject the solution with compounds of interest at specific concentrations. This includes colistin, E107, Melittin, and helix H0 domain of endophilin in ultrapure water. AFM images of a compound of interest-treated bilayers were acquired using the same procedure as for the control bilayer. The obtained AFM images were leveled by subtracting a polynomial background using in-house developed MATLAB scripts.

#### **2.2.3.5.2 Force measurement**

In the region of interest, evenly spaced points were marked on a bilayer area of 4  $\mu$ m  $\times$  4  $\mu$ m. Force measurements were performed at each point using the automated force-ramping function. The  $z$ -range for the force measurements was 100 nm; the approaching and retracting speed of the AFM tip was 200 nm/s; the number of data points for each curve was 2560. One parameter used to analyze the obtained force curves was the tip radius. The nominal tip radius was 20 nm for the ScanAsyst-Fluid probe. To obtain a more accurate estimation, we used the tip quantification function provided by the Nanoscope Analysis software. The function estimates tip

end radius by analyzing height images of a titanium characterizer sample (model RS-12M) that contains many sharp grain features.

#### 2.2.4 Bacterial studies

To investigate the effect of colistin on the gram-negative bacterial cells, *E. coli* (ATCC 25922) obtained from Dr. Jianfeng Cai's group in the Department of Chemistry, USF, were used. These cells were grown in LB broth medium (Miller from Fisher Scientific). A small aliquot (10  $\mu$ l) of the stock sample (stored at -80C, after thawing) is pipetted into 60 ml LB broth taken in 250 ml conical glass vessel. This vessel was loosely covered and placed in an incubator (MaxQ 8000, Thermofisher Scientific, NY) at 37C, 120 rpm. Overnight grown bacteria with optical density (OD<sub>600</sub>) ~1.0, measured by Nanodrop, were taken for experiment.

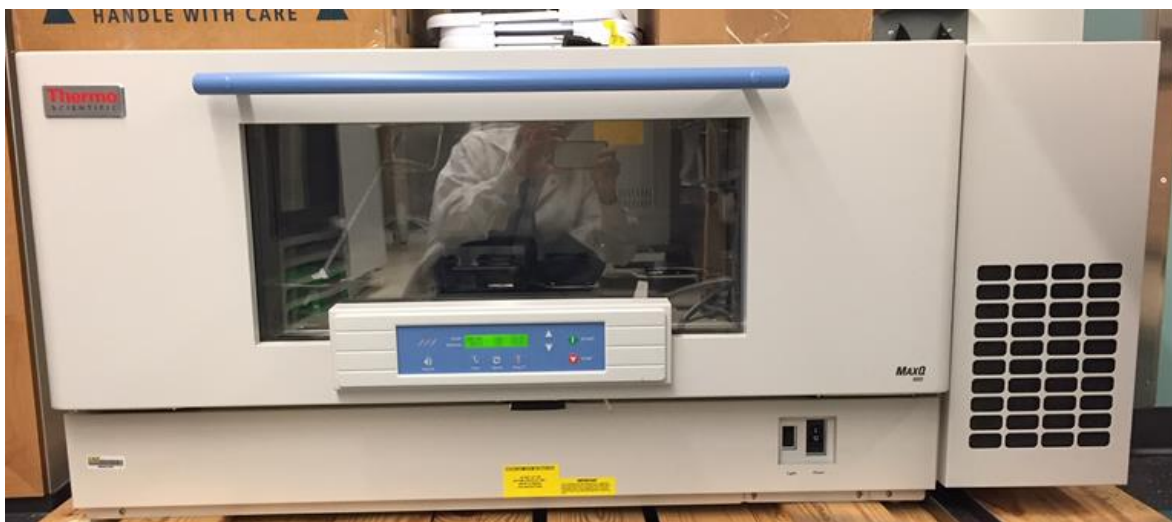


Figure 2.12 MaxQ 8000 incubator used to grow *E.coli* bacteria

We placed 200  $\mu$ l of freshly grown bacteria in 800  $\mu$ l of LB broth with appropriate colistin concentration taken in 48 well microplate (Falcon polystyrene Microplates, Fisher Scientific, Pittsburg, PA). This microplate was incubated at 37C in Heratherm incubator (Fisher Scientific,

USA) equipped with a microplate shaker (Fisher Scientific, USA) at 120 rpm. The samples were transferred to eppendorf tubes from the microplate and centrifuged to remove the broth. The pellet was suspended in 1 ml ultrapure water, and 20  $\mu$ l solution was deposited on freshly cleaved mica. After complete drying at room temperature, samples were scanned with AFM in air. Topographic images were acquired using the FMV-A probe scanned at 0.8-1 Hz scan rate with auto pick force set point.

### **2.3 Conclusion**

In this chapter, materials and methodologies used for the dissertation work are discussed. Here we introduced the most frequently used instruments like spectrofluorometer, atomic force microscopy and the micropipette aspiration of giant unilamellar vesicles. We also discussed the theoretical background and general operating procedure of the aforementioned techniques. Furthermore, we briefly discussed about the culture of *E.coli* cells along with sample preparation procedure to observe the topographical changes induced by colistin using atomic force microscopy.

### 3. PEPTIDOMIMETIC E107-3 EFFECT IN MODEL LIPID BILAYER<sup>1</sup>

In this chapter, we discuss the effect of a potential antimicrobial peptidomimetic, E107-3, on lipid membrane. The effects in lipid bilayers' structural and mechanical properties are studied using vesicle leakage experiments, micropipette aspiration and supported bilayers by AFM. A comparison effect of melittin is also performed. The part of this chapter is published earlier in *Biochim Biophys Acta* in 2017 under *Modulation of Lipid Membrane structural and Mechanical properties by a Peptidomimetic derived from Reduced Amide Scaffold*.

#### 3.1 Introduction

Multidrug resistance of infectious bacterial pathogens is becoming an emerging health problem worldwide. Small amphipathic antimicrobial peptides (AMPs) are nature's ancient antibiotics [49]. They possess a broad spectrum of antimicrobial activity and are less prone to eliciting multidrug resistance. However, AMP-based antibiotics suffer from several limitations, including immunogenicity and susceptibility to protease degradation [50]. Recently, creation and development of non-natural oligomeric peptide mimics, the so-called peptidomimetics, have become a field of large interest in biomedicine [51]. Examples include peptoids [52],  $\beta$ -peptides[53],  $\gamma$ - and  $\delta$ -peptides [54], azapeptides[55],  $\alpha$ -aminoxy-peptides [56], sugar-based peptides [57],  $\alpha/\beta$ -peptides [58], phenylene ethynylenes [59], and AApeptides [60, 61], to name a

---

<sup>1</sup> This chapter is partially reproduced from a work published in a peer reviewed journal. The author of this dissertation is the first author of the published work. See Appendix B for the permissions

few. By introducing unnatural backbones, these oligomers are more stable against proteolysis and are believed to have reduced immunogenicity [62].

Peptidomimetics containing reduced amide bonds have been shown to exhibit superb resistance to enzymatic degradation [63]. The unique properties offered by reduced amide have inspired a wave of interests in the field of biology and medicine [64-67]. We have recently developed a library of small compounds based on the reduced amide scaffold (Figure 1.6A) [29]. All compounds share the same backbone. However, the four side groups vary regarding hydrophobicity and charge state. Due to their amphipathic nature, the compounds are expected to have antimicrobial activities similar to AMPs. Indeed, a lead compound referred to as E107-3 (compound **13** in ref [29]) was identified. E107-3 exhibits bactericidal activity against both Gram-positive and Gram-negative microbes. The published preliminary study indicates that bacterial membranes become permeable to propidium iodide after being treated with E107-3 [29]. It seems that the compound acts by targeting and damaging bacterial membranes. Membrane damage induced by AMPs can proceed with different mechanisms, such as pore formation and detergent-like membrane disintegration [31]. In this study, we are interested in elucidating detailed structural and mechanical modulations of model lipid membranes imparted by E107-3.

We use vesicular and planar lipid bilayers in the study. To mimic the anionic nature of bacterial membranes, we add 10 mol% 1-palmitoyl-2-oleoyl-*sn*-glycero-3-phosphatidylglycerol (POPG) to lipid bilayers formed by 1-palmitoyl-2-oleoyl-*sn*-glycero-3-phosphatidylcholine (POPC). We note that the lipid composition of bacterial membranes is far more complicated than what we use here [68]. Therefore, the results we show in this study only represent an initial step toward a more comprehensive evaluation of different lipid species, whose physicochemical properties may be affected by the antimicrobial compound differently. Time-course and steady-

state fluorescence spectroscopy measurements are performed to investigate dose- and time-dependent membrane permeation induced by E107-3. The leakage experiment only provides averaged response of unilamellar vesicles (ULVs). To explore the kinetic response of individual giant unilamellar vesicles (GUVs), we use micropipette aspiration experiment [39, 43, 69-71]. Kinetic behavior of GUV area/volume is obtained by monitoring GUV protrusion length [40, 41, 72-74]. Solution atomic force microscopy (AFM) is used to visualize the impact of E107-3 on lipid bilayer structures within a nanoscopic regime. Different modes of action by E107-3 and melittin are obtained by comparing the resulting structures of planar lipid bilayers. In addition to providing bilayer topographic information [75-78], AFM measurements can also be used to determine bilayer mechanical properties [79-88]. We use AFM-based force spectroscopy to investigate bilayer mechanical perturbation exerted by E107-3. Quantitative mechanical modulation is obtained by determining the bilayer puncture force  $F_P$  and the bilayer area compressibility modulus  $K_A$  as a function of E107-3 concentration. Our experimental results provide useful insights into the molecular basis used by E107-3 in impairing lipid bilayer's structural and mechanical integrity. Such knowledge is useful for future optimization of antimicrobial peptidomimetics based on the reduced amide scaffold.

## **3.2 Results**

### **3.2.1 Calcein leakage**

We first use time-dependent vesicle leakage to assess the effect of E107-3 on lipid bilayer permeability. The control experiment with pure ULVs shows that no calcein leaks out during the experimental time scale (Figure 3.1A). The control experiment is necessary because osmotic stress caused by different salt concentrations in the interior and at the exterior of ULVs can artificially

induce calcein leakage. The addition of 20  $\mu\text{M}$  E107-3 results in a gradual increase of the fluorescence signal, suggesting that E107-3 enhances lipid bilayer permeability; increasing E107-3 to 30  $\mu\text{M}$  yields a faster leakage behavior; the leakage rate is continuously increased by larger concentrations of E107-3 (i.e., 60, 80, and 100  $\mu\text{M}$ ).

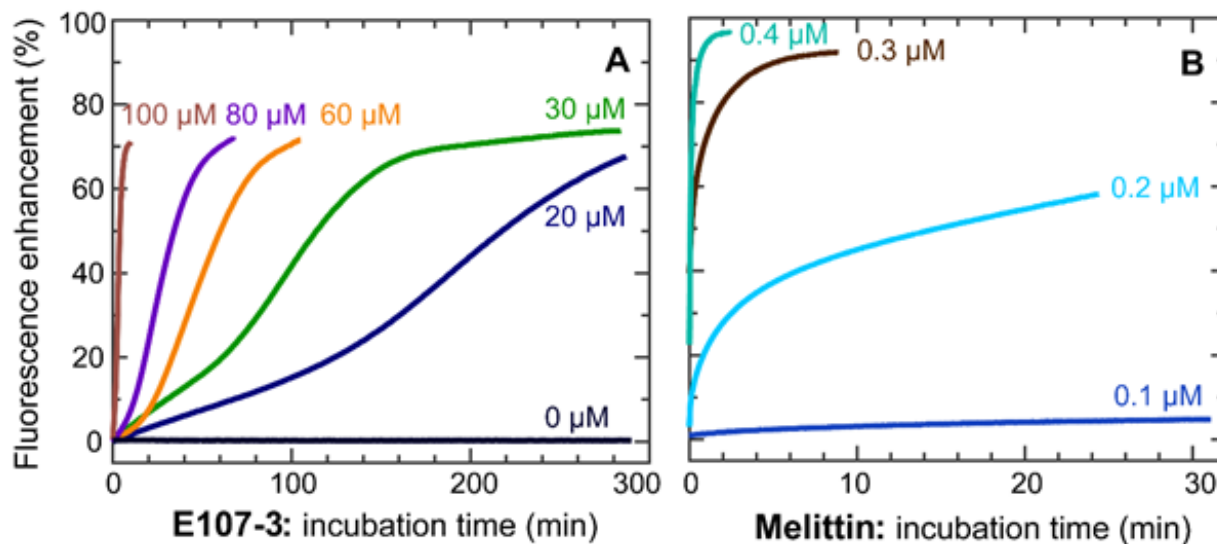


*Figure 3.1 Time-course measurements of the fluorescence enhancement of calcein-enclosed POPC/POPG ULVs exposed to different concentrations of E107-3 (A). A control experiment without E107-3 is also displayed. Similar time-course measurements for POPC/POPG ULVs exposed to the antimicrobial peptide melittin at four concentrations(B).*

For comparison, time-course measurements of the well-studied antimicrobial peptide melittin are also shown (Figure 3.1B). [40, 73, 89]. For 0.1  $\mu\text{M}$  melittin, almost no increase of the fluorescence signal is observed over the 30-min incubation period; the increase of the fluorescence signal becomes fairly significant over  $\sim 30$  min for 0.2  $\mu\text{M}$  melittin; near full leakage is achieved within a few minutes for melittin  $\geq 0.3$   $\mu\text{M}$ . Compared to E107-3, melittin seems to require much lower concentration to cause acute calcein leakage. This implies that different mechanisms might be utilized by the two agents to increase bilayer permeability.

To study the leakage behavior over a longer period, we measure fluorescence spectrum of calcein-enclosed ULVs incubated with different concentrations of E107-3 for ~20 h (Figure 3.2(1)).

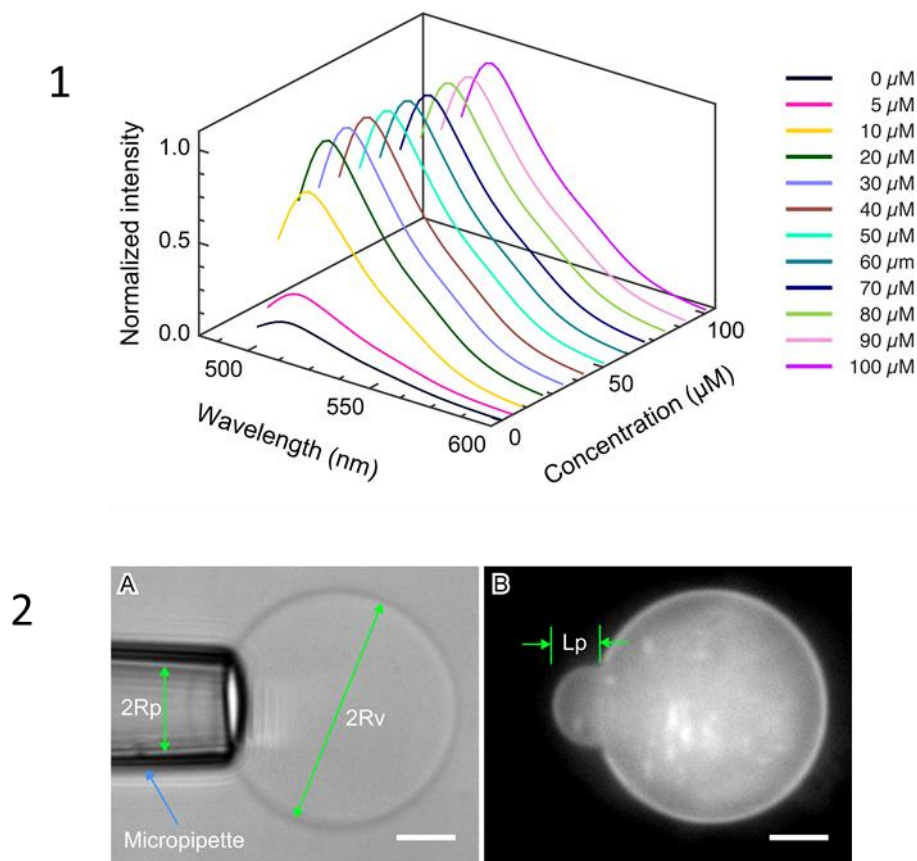
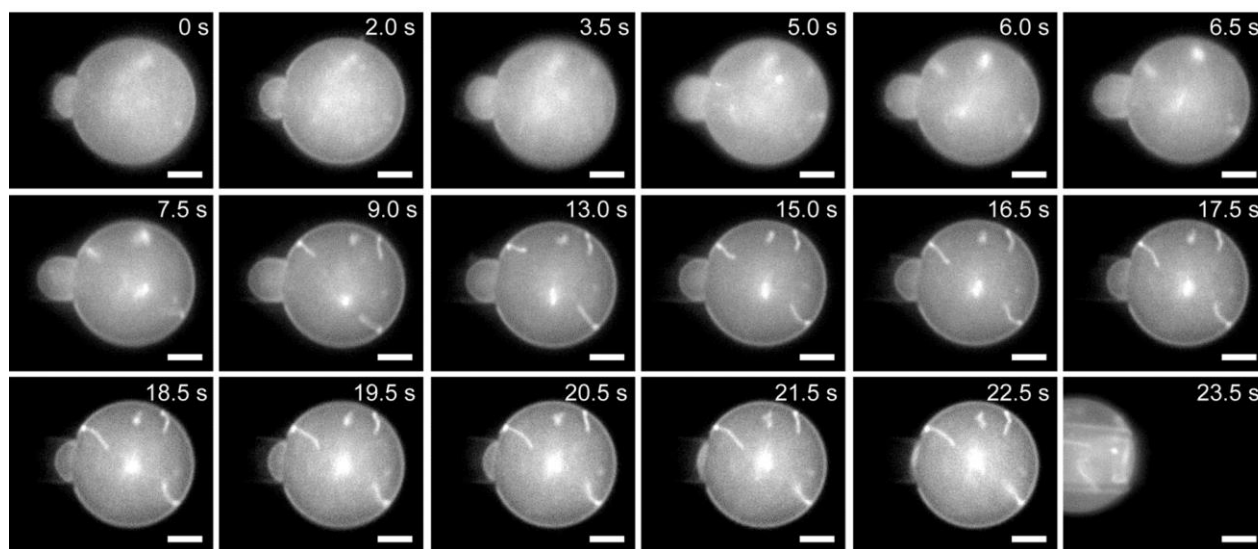


Figure 3.2 Fluorescence spectra of calcein-enclosed ULVs incubated with different concentrations of E107-3 for ~20 hours (1). Each spectrum is normalized by the maximum intensity of ULVs treated with 20 mM Triton X-100. In panel 2, Bright field (A) and fluorescence (B) images of an aspirated POPC/POPG GUV are shown. The protrusion length  $L_p$ , the micropipette inside diameter  $2R_p$ , and the GUV diameter  $2R_v$  are illustrated. Scale bars are 10  $\mu\text{m}$ .

The obtained spectra are normalized by the peak intensity at 514 nm for ULVs treated with 20 mM Triton X-100. It is clear that full leakage is achieved for E107-3  $\geq 20 \mu\text{M}$  over the 20-h incubation period, whereas 5  $\mu\text{M}$  E107-3 is only able to induce a small fraction of calcein leakage.

### 3.2.2 Micropipette aspiration of GUVs

Fluorescence spectroscopy-based leakage experiment only provides averaged response of ULVs treated with insulting agents [32, 90]. We use micropipette aspiration of GUVs to obtain a qualitative response of individual vesicles exposed to E107-3. Under a small constant negative pressure, the GUV protrudes by a length  $L_P$  into the micropipette (Figure 3.2(2)) The change of  $L_P$  is directly related to the change of the GUV area and volumetric properties.



*Figure 3.3 Real-time response of an aspirated POPC/POPG GUV exposed to 5  $\mu$ M E107-3. Scale bars are 10  $\mu$ m*

Immediately after retracting the transfer-pipette from the micropipette in the reaction well (marked as  $t=0$  s), the kinetic response of the aspirated POPC/POPG GUV to 5  $\mu$ M E107-3 is shown in Figure 3.3. The GUV protrusion length  $L_P$  increases spontaneously and reaches a maximum value at  $\sim 7.5$  s, after which the protrusion length decreases continuously. The GUV is ruptured when the protrusion length diminishes to near zero. In addition to the change of the protrusion length, Figure 3.3 shows that string-like structures emerge near  $\sim 9.0$  s. These strings are anchored to the inner leaflet of the GUV. Since they are visible under the fluorescence

microscope, the strings contain Rh-DPPE lipids. Other features have been observed when GUVs are exposed to membrane active molecules, such as tubules [91] and lipid clusters (or substances) [72]. The formation of extra features (e.g., strings, tubules, and clusters) requires lipids derived from GUVs. Therefore, our observation could indicate that E107-3 is able to extract lipid molecules from the GUV bilayer.

We have performed the aspiration measurements for >30 GUVs. The majority of them exhibit the similar trend of the protrusion length shown in Figure 3.3, i.e.,  $L_P$  increases and then decreases followed by GUV rupture. However, the time point when the  $L_P$  starts to decrease does vary. This could be caused by variation of the initial suction pressure, the quality of the micropipette, and GUV parameters (e.g., size). In a few cases, GUVs rupture before  $L_P$  decreases noticeably. These GUVs might have a “weaker” resistance to rupture.

Overall, the GUV aspiration experiment qualitatively shows that E107-3 binds to lipid bilayers, resulting in a modulated protrusion length that first increases and then decreases as a function of the incubation time. To gain a better understanding of the effects of E107-3 on lipid bilayer physical properties, we use solution AFM experiments to characterize structural and mechanical parameters of planar lipid bilayers within a nanoscopic regime

### **3.2.3 Solution atomic force microscopy**

Solution AFM is used to visualize the effect of E107-3 on POPC/POPG lipid bilayer structure. A mica-supported planar bilayer is first prepared in the AFM fluid cell. After bilayer formation, excessive SUVs are flushed out by injecting buffer solution. During the bilayer preparation process, the AFM tip is positioned at  $\sim 50 \mu\text{m}$  above the mica surface. AFM height images are acquired by engaging the tip to different locations. The height image of the intact bilayer is shown in Figure 3.4A. The height profile along the bilayer surface indicates that the

surface roughness is  $\sim 0.1$  nm. We note that the topographic structure of the planar bilayer is uniform within the fluid cell. This is confirmed by scanning and comparing bilayer patches at different locations. Bilayer uniformity is important when studying structural modulation induced by E107-3 because the AFM tip is moved to different locations (to eliminate the influence of repetitive scanning) to acquire height images and perform force spectroscopy measurements.

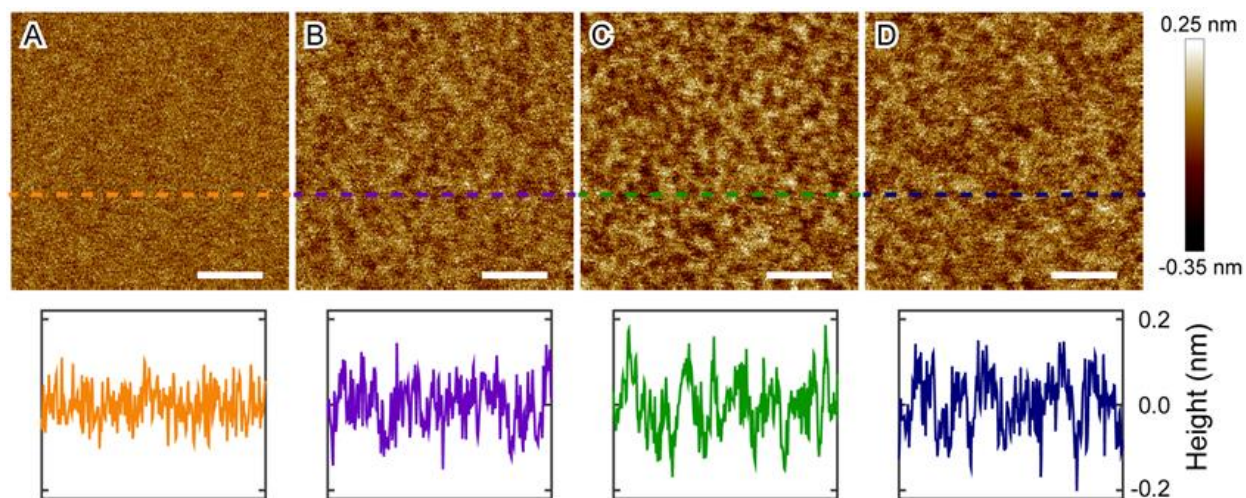


*Figure 3.4 Solution AFM height images of a POPC/POPG bilayer exposed to incremental concentrations of E107-3: 0  $\mu\text{M}$  (A), 5  $\mu\text{M}$  (B), 20  $\mu\text{M}$  (C), and 100  $\mu\text{M}$  (D). The bottom row displays height profiles along the dashed lines highlighted in A–D. Scale bars are 100 nm*

After image acquisition of the control bilayer at several locations ( $\geq 3$ ), the AFM tip is retracted, and a solution containing 5  $\mu\text{M}$  E107-3 is injected. The bilayer is exposed to the 5  $\mu\text{M}$  E107-3 solution for  $\sim 30$  min, after which the AFM tip is moved to a different location to acquire the modified bilayer topography (Figure 3.4B). It is clear that the bilayer becomes rougher with many higher and lower features. The height profile indicates that the bilayer roughness increases to  $\sim 0.2$  nm. The total reaction time between the bilayer and the 5  $\mu\text{M}$  E107-3 is about 2 h. (Similar amount of the reaction time is used for other concentrations of the compound.) During the  $\sim 2$ -h

incubation period, we do not find noticeable changes of the bilayer topography (Figure 3.5). The absence of kinetic modulation could indicate that bilayer perturbation imparted by E107-3 completes before the first scan is taken. To explore the effect of E107-3 at higher concentrations, we inject a solution containing 20  $\mu\text{M}$  E107-3 to replace the 5  $\mu\text{M}$  solution. After equilibrating for  $\sim 30$  min, the height image (acquired at a different location) is shown in Figure 3.4C. The heterogeneous features observed at 5  $\mu\text{M}$  E107-3 become more pronounced, accompanied by a slightly larger bilayer roughness. Finally, we inject a solution containing 100  $\mu\text{M}$  E107-3 to replace the 20  $\mu\text{M}$  solution. The topographic structure of the planar bilayer (acquired at a different location) is further modified, although the surface roughness does not seem to increase (Figure 3.4D).

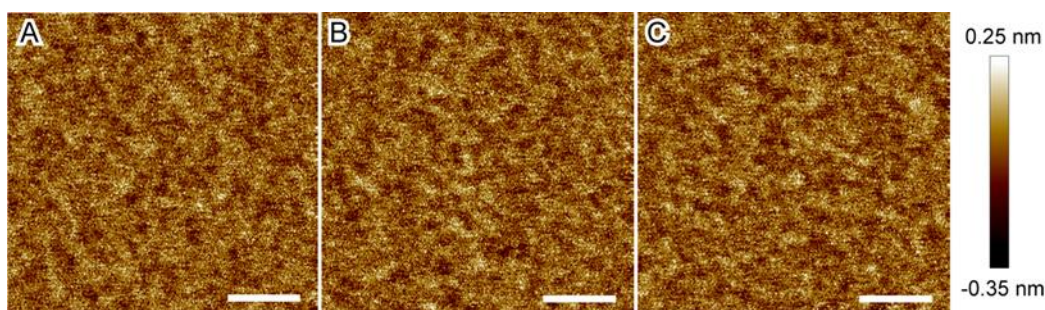


*Figure 3.5 Solution AFM height images of a POPC/POPG bilayer exposed to 5  $\mu\text{M}$  E107-3 for different amount of times. The three images are acquired in sequence with a time interval of  $\sim 40$  min. Scale bars are 100 nm.*

AFM height images reveal that E107-3 modifies lipid bilayer topography, but does not produce pore-like structures. To support this statement, we expose a POPC/POPG bilayer to the well-studied antimicrobial peptide melittin, which is known to form transmembrane pores (or defects) [40, 89, 92]. After equilibrating with 0.4  $\mu\text{M}$  melittin for  $\sim 30$  min, the bilayer is perforated with numerous pore-like defects (Figure 3.6). It is noteworthy that the maximum depth of the

defects is smaller than the bilayer thickness ( $\sim 3\text{--}4$  nm) [93-95]. This is mainly related to the geometry and size of the AFM tip (and scanning parameters such as tip speed) [89]. Nevertheless, a comparison between Figure 3.4 and Figure 3.6 clearly shows that E107-3 and melittin disrupt lipid bilayers by different mechanisms.

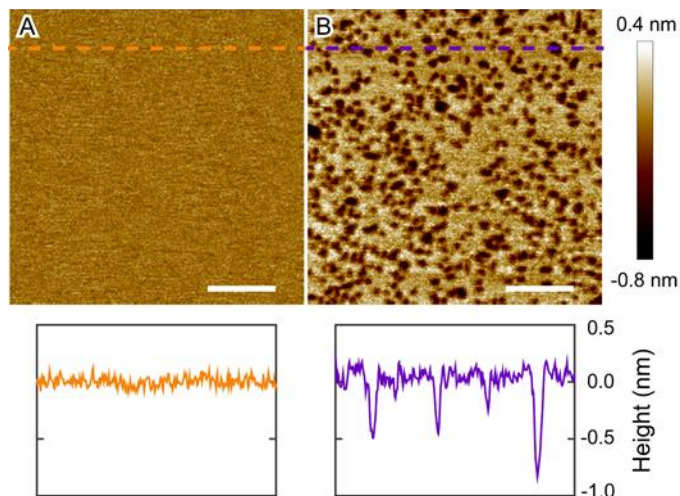


*Figure 3.6 Solution AFM height image of a POPC/POPG bilayer before (A) and after (B) being exposed to  $0.4 \mu\text{M}$  melittin. Scale bars are 100 nm. The bottom row displays height profiles along the dashed lines highlighted in (A) and (B).*

The planar bilayer exposed to E107-3 does not contain transmembrane pores, but rather resembles the fluctuation-like structures observed in ternary lipid mixtures [96, 97]. A correlation length  $\xi$  was used to describe the length scale of the fluctuation-like structures [96, 97]. Correlation length has also been used to characterize the length scale of critical fluctuations observed in GUVs [98, 99]. Here we use the same concept of the correlation length to characterize the length scale of the heterogeneous features induced by E107-3 (Figure 3.4). First, we calculate the height weighted pair distribution function  $G(r)$  [99, 100]

$$G(r) = \langle h(r) \times h(r + \delta) \rangle - \langle h(r) \rangle \langle h(r + \delta) \rangle \quad (3.1)$$

where brackets denote ensemble average over the radial distance  $\delta$ . Within a certain distance range  $r$ , the pair distribution function  $G(r)$  decays exponentially [99, 100]. The corresponding decay length is defined as the correlation length  $\xi$ . A similar calculation has been performed by Connell et al. to show that the correlation length of planar lipid bilayers decreases at elevated temperatures [97].

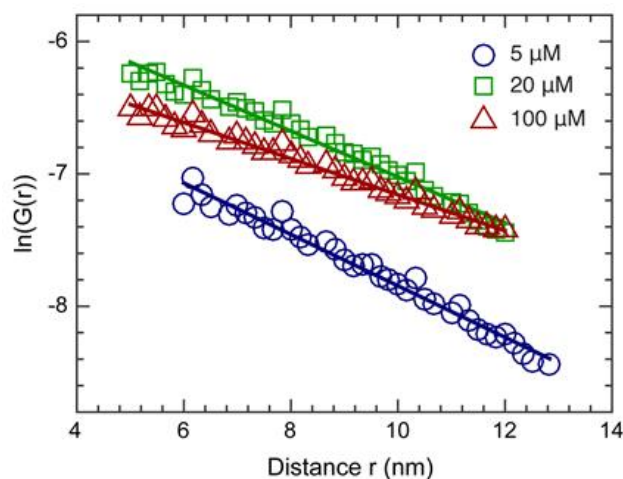


*Figure 3.7 Height-weighted pair distribution functions  $G(r)$  for a POPC/POPG bilayer exposed to different concentrations of E107-3. Linear fitting to the logarithm of  $G(r)$  gives rise to the correlation length  $\xi$ , which is 5.1, 5.8, and 7.3 nm for 5, 20, and 100  $\mu\text{M}$  E107-3, respectively.*

A qualitative description of the correlation length is that it is correlated with the distance between nearest neighbors that have the same features in AFM height images Figure 3.7. shows linear fits to the logarithm of the pair distribution functions  $G(r)$ . The resulting correlation length is 5.1, 5.8, and 7.3 nm for 5, 20, and 100  $\mu\text{M}$  E107-3, respectively (uncertainty of  $\sim 3$  nm). Close examination indicates that at a fixed distance  $r$ , the pair distribution function is about one order of magnitude smaller at 5  $\mu\text{M}$  than at 20 and 100  $\mu\text{M}$  E107-3. This is consistent with the trend of the bilayer roughness as a function of the peptide concentration shown in Figure 3.4.

### 3.2.4 AFM-based force spectroscopy

The obtained AFM height images indicate that E107-3 modulates lipid bilayer structure by generating heterogeneous features. To study how E107-3 perturbs lipid bilayer mechanical properties, we use AFM-based force spectroscopy. Force measurements are performed on the same bilayer (but at different regions within the fluid cell) as the peptide concentration increases. Since the same tip is used throughout the experiment, relative changes of the bilayer mechanical properties derived from the force spectroscopy data can be unambiguously determined. Moreover, the size of the determined correlation length of the modulated bilayer (Figure 3.4) is smaller than the AFM tip size (~20 nm) used in force spectroscopy measurements. This means that each force curve corresponds to an averaged measure of the heterogeneous bilayer. To gain good statistics, (i) multiple force curves are measured at one bilayer region, (ii) force measurements are performed at different bilayer regions (by manually moving the tip to different locations), and (iii) experiments are repeated by using different bilayers. Overall, the trend of the force curves as a function of the peptide concentration is very repeatable. However, for control bilayers prepared from different runs, the magnitude of the maximum force that punctures the bilayer can vary up to ~0.4 nN. This variation is comparable to the change caused by E107-3 as shown later. To eliminate the variation between different runs, the force spectroscopy data presented here correspond to the experiment performed on one bilayer.

The schematic of a force spectroscopy measurement is illustrated in Figure 3.8. (We only consider the tip force during the approaching process.) When the tip is far away from the bilayer surface (step 1), the force experienced by the tip is zero (after subtracting a baseline). Once the tip is near the bilayer surface, the tip force deviates slightly from zero due to non-steric interactions, such as hydration and van der Waals interactions [101].

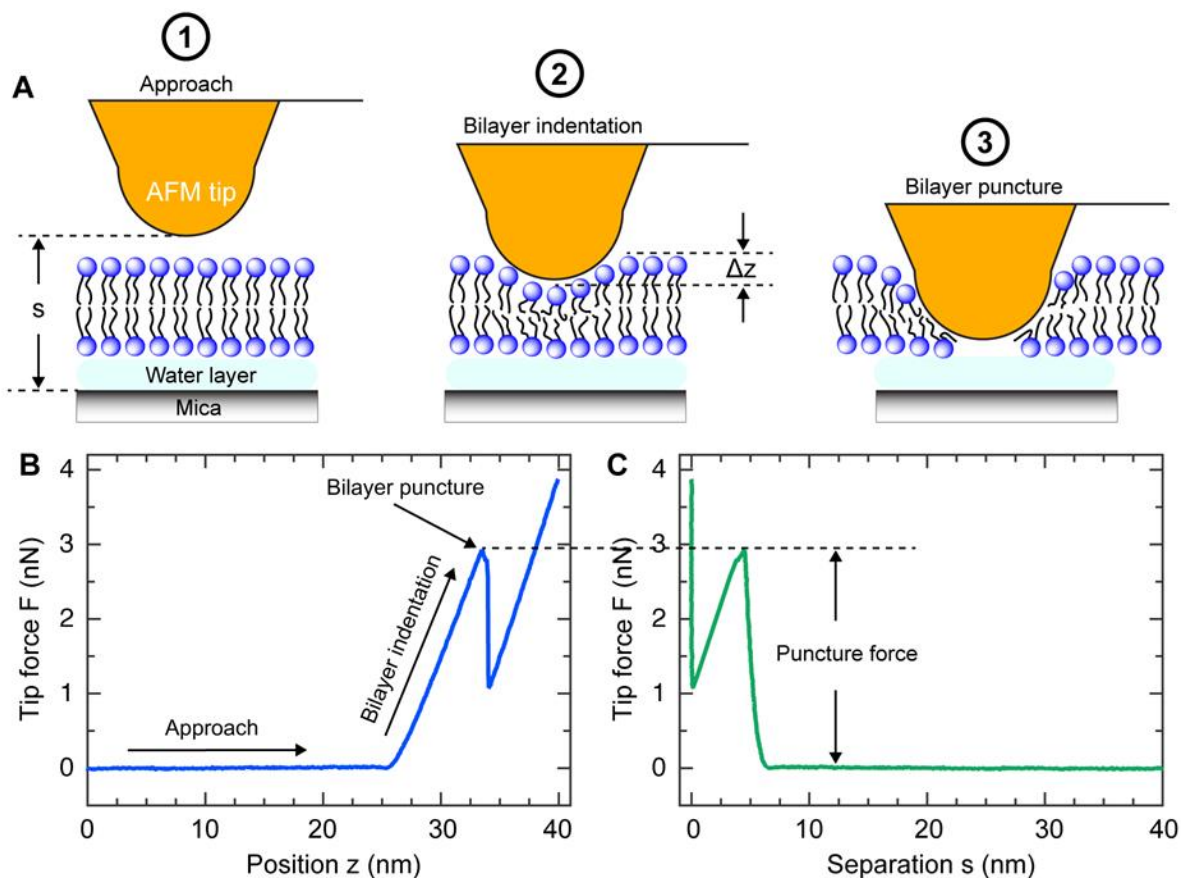


Figure 3.8 Schematic of an AFM-based force spectroscopy measurement as the tip approaches a planar lipid bilayer (A). An example of a tip force-position curve (B). The tip position  $z$  in (B) is converted into tip-mica separation  $s$ , resulting in a tip force-separation curve (C).

The tip force increases continuously as the tip indents into the lipid bilayer, which deforms elastically (step 2). A maximum force defined as the puncture force  $F_P$  is reached right before the bilayer fails (step 3). The puncture force reflects the mechanical stability that a bilayer can withstand before being punctured by the AFM tip. After bilayer puncture, the tip rapidly moves across a thin water layer that resides between the bilayer and the mica substrate [102, 103]. The tip force increases drastically after touching the mica surface. The raw data from force spectroscopy is the tip force (or cantilever deflection) and the vertical position  $z$  of the scanner. For our data analysis, the scanner position  $z$  is converted into the mica-tip separation  $s$  (Figure 3.8) [104].

Force-separation curves ( $>300$ ) at each concentration of E107-3 are shown in Figure 3.9A. The tip force gradually increases when the separation becomes smaller than  $\sim 6$  nm. To obtain the position where bilayer puncture occurs, we bin the force curves into the two-dimensional space of force and separation (Figure 3.10). The obtained probability indicates that at  $0 \mu\text{M}$  E107-3, the puncture force occurs at  $s$  of  $3.4\text{--}4.5$  nm. The distance between the point where the force starts to increase (i.e., force onset) and the point where the bilayer is punctured is slightly less than the reported POPC or POPG bilayer thickness ( $\sim 3\text{--}4$  nm) [93-95]. This could be explained by considering that bilayer puncture occurs before the apex of the tip reaches the bottom of the supported bilayer. Such a consideration is reasonable since the tip end radius is  $\sim 20$  nm, which is much larger than the distance between the nearest lipid chains ( $\sim 1$  nm). Similar positions of the force onset and bilayer puncture are observed when the concentration of E107-3 increases (Figure 3.10). This indicates that the supported bilayer is not disintegrated and remains stable after being exposed up to  $100 \mu\text{M}$  E107-3. Our result is in contrast to the effect of ethanol, which shifts the positions of the force onset and bilayer puncture to smaller  $s$  [101].

The puncture force is correlated with bilayer stability. However, its magnitude is affected by many factors, including buffer condition, sample preparation protocol, tip selection, and parameters used for force measurements. Large variation of bilayer puncture forces has been reported by different groups (from  $<1$  nN to  $>10$  nN) [81, 82, 86, 87, 101, 105-111]. For the POPC/POPG bilayer in this study, the probability distribution of  $F_P$  indicates that the most probable  $F_P$  is  $2.8$  nN (Figure 3.9B). The most probable  $F_P$  remains the same at  $5 \mu\text{M}$  E107-3, and decreases slightly to  $2.6$  and  $2.4$  nN at  $20$  and  $100 \mu\text{M}$  E107-3, respectively. Considering the widths of the puncture force distributions (FWHM is  $0.40$ ,  $0.15$ ,  $0.21$ , and  $0.18$  nN for  $0$ ,  $5$ ,  $20$ , and  $100$

$\mu\text{M}$  E107-3, respectively), the change of  $F_P$  induced by E107-3 is relatively small. This highlights that the mechanical stability of the lipid bilayer is not markedly altered by E107-3.

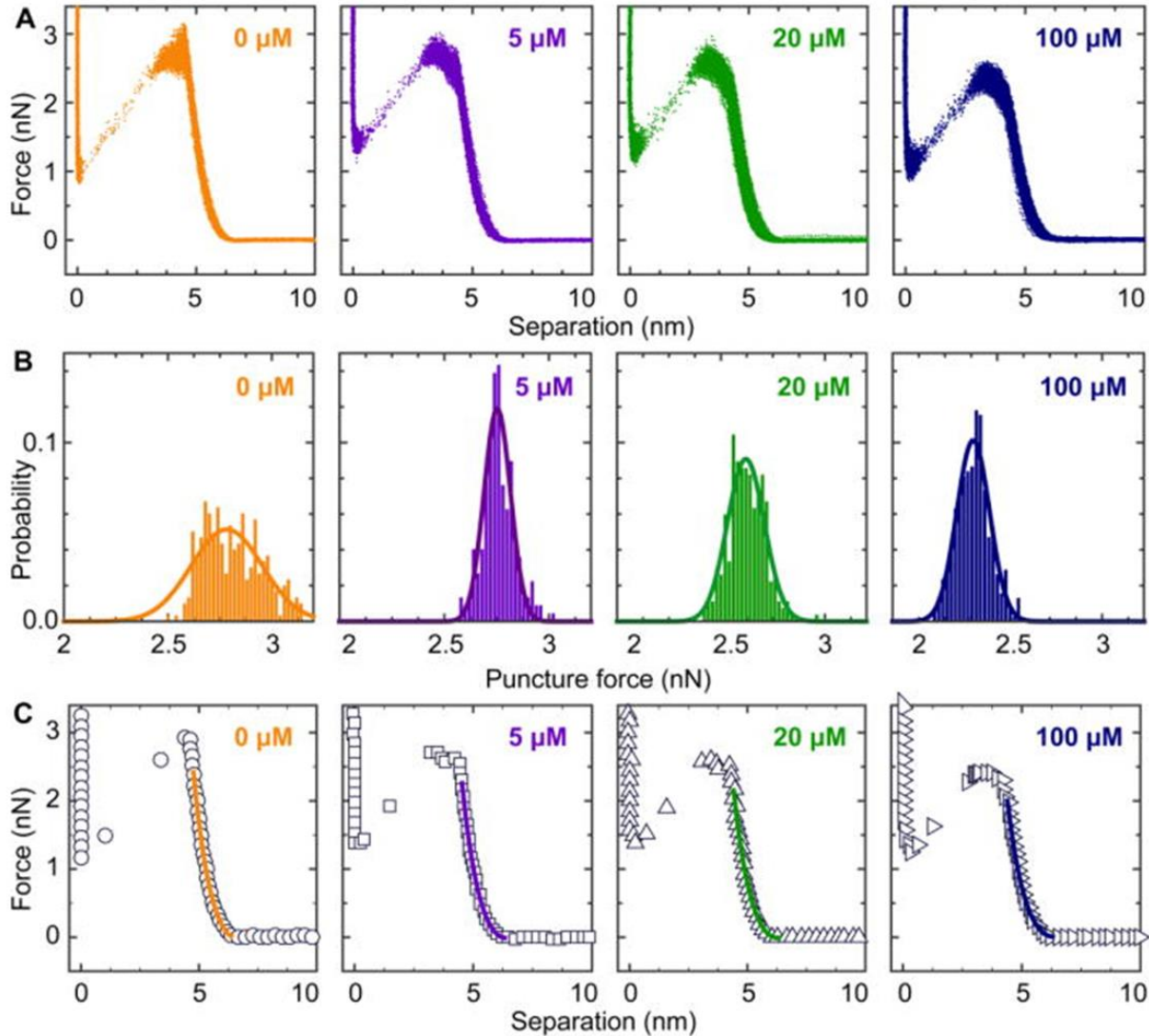


Figure 3.9 Force-separation curves of a POPC/POPG bilayer exposed to incremental concentrations of E107-3. Each panel is a superposition of  $>300$  curves. (A) Probability distributions of the puncture force  $F_P$  determined from force-separation curves. Solid lines are Gaussian curve fitting (B). An example of model fitting to force-separation curves at different peptide concentrations (C).

In addition to the puncture force, other mechanical properties of the lipid bilayer can be inferred from the obtained force-separation curves. In the elastic deformation regime of the lipid

bilayer, the tip force is dominated by stretching of lipid molecules near the tip. Free energy calculation of a tension-free lipid bilayer results in a quadratic relationship between the tip force and the tip-mica separation  $s$  [103]:

$$F = \pi K_A R \left( \frac{D - s}{s} \right)^2 \quad (3.2)$$

where  $K_A$  is the lateral area compressibility modulus of the lipid bilayer,  $R$  is the tip end radius, and  $D$  is the bilayer thickness.

The equation assumes that the thickness of the water layer between the bilayer and the mica surface is zero. For non-zero water layer thickness,  $D$  is a combination of the thicknesses of the bilayer and the water layer. Using equation (3.2) and the obtained force spectroscopy data, we are able to determine the change of the lipid bilayer's mechanical property (i.e.,  $K_A$ ) after being exposed to E107-3.

An example of the elastic model fitting is shown in Figure 3.9C. It is clear that good agreement is obtained between the theoretical prediction and the force spectroscopy data. Two criteria are used to determine the region for data fitting: (i) the tip force is no larger than 80% of the puncture force  $F_P$  (the cut-off force), and (ii) the largest tip-mica separation  $s$  is 6.2 nm (the cut-off position). The first criterion is based on the observation that many force curves deviate from the quadratic function when the force approaches  $F_P$ ; the second criterion is related to the fact that the equation is only valid within a regime where the lipid bilayer deforms elastically. Nevertheless, we find that the effect of the cut-off position is minimal, whereas an increase of the cut-off force to 90% of  $F_P$  decreases  $K_A$  by ~8%. It has shown that the attractive force between the

mica and the tip is near zero in a fluid when  $s$  is larger than 2 nm [112]. Therefore, the influence of the mica substrate is negligible for our data fitting using the elastic deformation model.

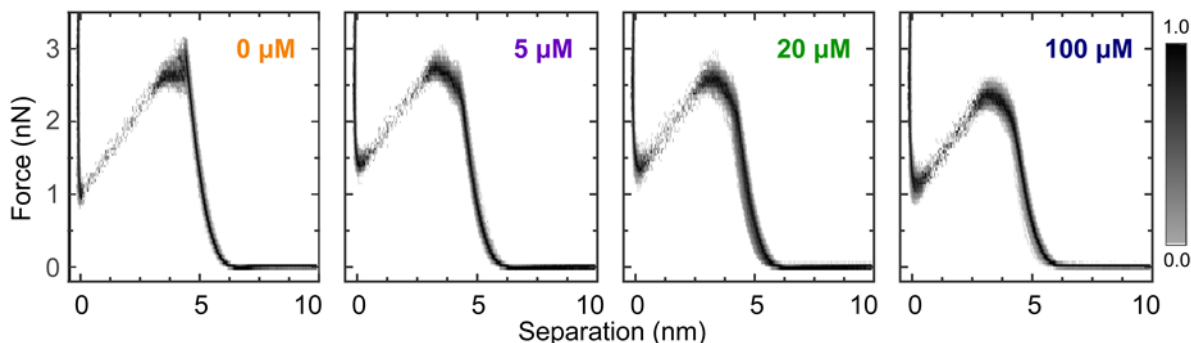


Figure 3.10 Probability distributions of force-separation curves shown in Figure 3.9. The probability of each panel is obtained by binning >300 curves into two-dimensional grids. For a fixed separation  $s$ , the probability (along  $F$  direction) is normalized by the maximum probability at that separation  $s$ .

Using equation (3.2) and the two cut-off criteria, we analyze all the force curves shown in Figure 3.9A. The results are summarized in Table 3-1. The obtained  $K_A$  is  $246 \pm 19$  mN/m for the control bilayer. This value is in good agreement with the reported value for a POPC bilayer obtained from micropipette aspiration [113]. Bilayer elastic parameters can also be evaluated using molecular dynamics (MD) simulations. The reported  $K_A$  from the simulation work is smaller for POPG than for POPC bilayers [114]. Since the POPC/POPG bilayer we use contains 10 mol% POPG, our  $K_A$  may not exactly correspond to that of a pure POPC bilayer.

Table 3-1 Concentration-dependent effect of E107-3 on lipid bilayer nanomechanics. The bilayer area compressibility modulus  $K_A$  is determined from AFM-based force spectroscopy data

107-3( $\mu$ M)	0	5	20	100
$K_A$ (mN/m)	$246 \pm 19$	$202 \pm 24$	$182 \pm 21$	$151 \pm 18$

To explore the impact of E107-3 on the elastic property of planar lipid bilayers, we perform force spectroscopy measurements after exposing the bilayer to incremental concentrations of E107-3. The obtained force curves are analyzed using the elastic bilayer deformation model (equation 3.2). The resulting  $K_A$  is  $202 \pm 24$ ,  $182 \pm 21$ , and  $151 \pm 18$  mN/m at 5, 20, and 100  $\mu$ M E107-3, respectively. Equation (3.2) shows that the determined  $K_A$  is stringently associated with the tip radius  $R$ ; therefore, the uncertainty of the tip radius contributes as the primary source for the uncertainty of  $K_A$  [103]. However, since the same tip is used for the force spectroscopy measurements, the values of  $K_A$  in Table 3-1 unequivocally show that E107-3 decreases  $K_A$  of the planar bilayer.

### **3.2.5 Double-bilayer structure in the presence of calcium ions**

In addition to modulating bilayer physical properties, AMPs can also impair lipid bilayers by extracting lipids from the bilayer environment [31]. In the presence of fusogenic agents, the extracted lipids may associate together and spontaneously form a second bilayer on top of the original bilayer (i.e., a double-bilayer architecture mimicking the pre-fusion contact state [115]). We use calcium ion as a fusion promoter [116] to test whether E107-3 can extract lipid molecules from planar bilayers. The experimental procedure is very similar to solution AFM measurements presented in the section of Materials and Methods. The main difference is that force spectroscopy measurements are performed on the same bilayer after obtaining an AFM image. After forming a POPC/POPG bilayer in the AFM fluid cell, we remove excessive vesicles and then inject a buffer solution containing 5 mM  $\text{CaCl}_2$  and 10 mM HEPES pH 7.4. Solution AFM imaging and force spectroscopy measurements show that a single bilayer is formed (Figure 3.11). We later add 50  $\mu$ M E107-3 in 5 mM  $\text{CaCl}_2$  and 10 mM HEPES pH 7.4 to the preformed planar bilayer. After incubating for  $\sim$ 40 min, the resulting AFM image containing two distinct regions is shown

in Figure 3.12. Height discontinuity at the region boundary indicates that the two regions have a height difference of  $\sim 5.5$  nm Figure 3.12 This value is close to the total thickness of a lipid bilayer and an inter-bilayer water layer [117]

To validate the formation of a double-bilayer structure, we perform force spectroscopy measurement. It is found that the lower region (region **a**) has a single puncture event located at a separation  $s$  of  $\sim 3.5$  nm (Figure 3.12C). Conversely, the higher region (region **b**) exhibits two puncture events located at a separation  $s$  of  $\sim 3.5$  nm and  $\sim 8.1$  nm, respectively. The force onset position corresponding to the two puncture events is located at  $s$  of  $\sim 5.6$  nm and  $\sim 11.0$  nm, respectively.

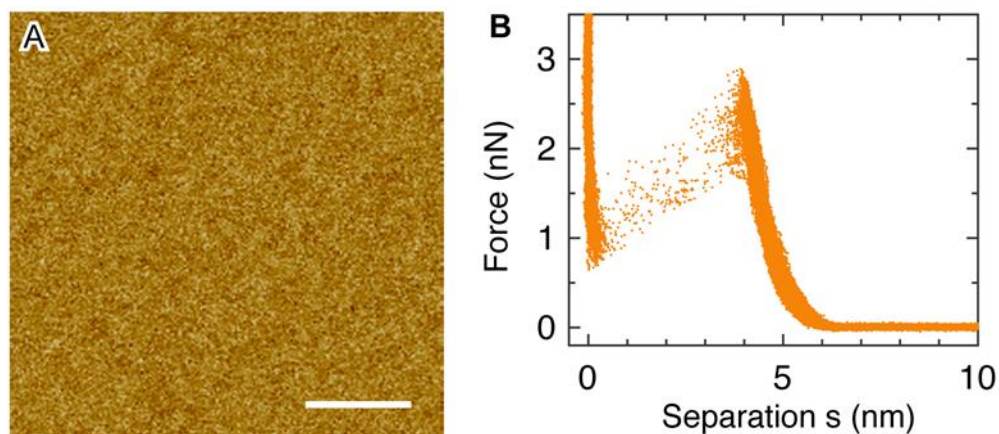


*Figure 3.11 Solution AFM height image of a POPC/POPG bilayer in 5 mM  $\text{CaCl}_2$  and 10 mM HEPES pH 7.4. Scale bar is  $0.6 \mu\text{m}$  (A). Force spectroscopy data for the bilayer in (A). A single puncture event is seen at a separation  $s$  of  $\sim 4.1$  nm and a puncture force  $F_P$  of  $\sim 2.2$  nN (B)*

These two values correspond well to the surface positions of mica-supported single and double bilayers [76]. Moreover, similar two-puncture events have been observed for double-bilayer membranes [118]. Based on the similar shape of the two force curves located at  $\sim 3.5$ – $5.6$  nm and  $\sim 8.1$ – $11.0$  nm (Figure 3.12C), as well as the height difference between the two regions

(Figure 3.12B), it is clear that the higher region corresponds to a double-bilayer structure, while the lower region corresponds to a single-bilayer structure. Formation of a second bilayer on top of the mica-supported bilayer requires lipid molecules that can only be supplied by the original bilayer (i.e., the mica-supported bilayer); therefore, our double-bilayer experiment demonstrates that E107-3 can extract lipids from planar bilayers.

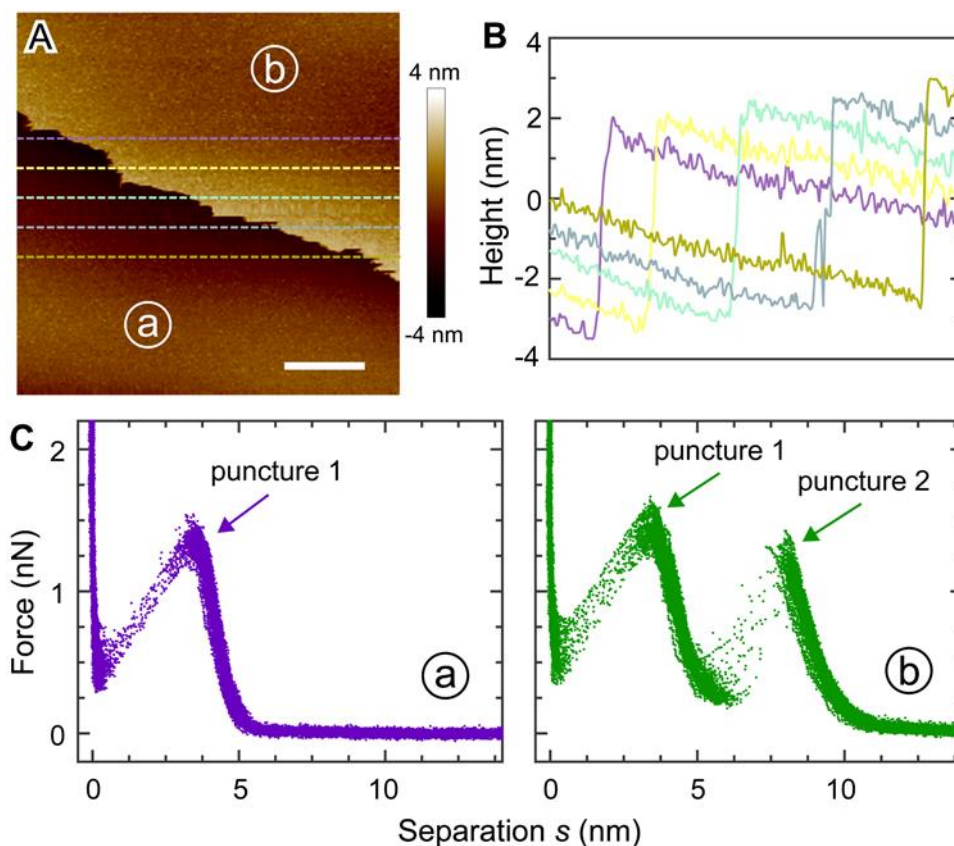


*Figure 3.12 A POPC/POPG bilayer treated with 50  $\mu\text{M}$  E107-3 in the presence of 5 mM  $\text{CaCl}_2$ . (A) Solution AFM height image. Two regions with distinct heights are highlighted as region **a** and **b**. Scale bar is 0.6  $\mu\text{m}$  (B) Height profiles along the dashed lines indicated in (A). A height discontinuity is seen when the horizontal lines cross the boundary of the two regions. (C) Force spectroscopy data for the region **a** and **b**, respectively. Only one puncture event is observed for the region **a**, while two puncture events are observed for the region **b**.*

Another piece of evidence supporting the role of lipid extraction by E107-3 is that similar double-bilayer structure using AFM imaging and force spectroscopy measurements are obtained when we expose POPC/POPG bilayers to the antimicrobial peptide daptomycin in the presence of calcium ions (unpublished data). Since it has been shown that daptomycin functions by extracting lipids [72], it is reasonable to argue that E107-3 can work in a similar way. Relating to the lipid extraction effect, one interesting question is which lipid (i.e., POPC or POPG) in our system is more prone to be extracted. As mentioned earlier, the two force curves corresponding to the double-bilayer structure have similar shapes (Figure 3.12C). This means that the physical properties of the two bilayers are similar. Since the original bilayer is composed of POPC and POPG, it is plausible that the newly formed bilayer contains both POPC and POPG, i.e., both POPC and POPG can be extracted by E107-3. Regarding the mechanism of the formation of a second bilayer, calcium ions promote the fusion propensity of extracted lipids; therefore, the extracted lipids by E107-3 can spontaneously deposit onto an existing surface (i.e., the original bilayer). This process has some similarity to the planar bilayer formation on a mica surface using SUVs.

### **3.3 Discussion**

In this study, we use a combination of experimental approaches to interrogate the molecular mechanism of a recently synthesized antimicrobial compound based on acylated reduced amide scaffold. The compound referred to as E107-3 has been demonstrated to exhibit promising antimicrobial property with a minimum inhibitory concentration  $<10 \mu\text{M}$  for both Gram-positive and Gram-negative microbes [29]. We specifically focus on how E107-3 impairs lipid membrane structural and mechanical integrity.

Using fluorescence spectroscopy-based calcein leakage experiment, we show that E107-3 perturbs lipid bilayer structure, yielding defects that allow calcein to permeate through the hydrophobic barrier. Vesicle leakage rate is dependent on the concentration of E107-3. The majority of the leakage occurs within the first few hours for concentrations  $\geq 20 \mu\text{M}$ , whereas  $5 \mu\text{M}$  of E107-3 is only able to induce a minuscule fraction of calcein leakage after incubation of  $\sim 20$  h. Compared to melittin, which causes acute vesicle leakage at  $<1 \mu\text{M}$ , E107-3 may perturb lipid bilayer properties through a mechanism that is different from transmembrane pore formation.

The kinetic response of individual vesicles to the treatment of E107-3 is qualitatively illustrated by the micropipette aspiration experiment. We find that the protrusion length of the aspirated GUV first increases and then decreases to near zero before the vesicle ruptures. The increase of the protrusion length most likely corresponds to the initial binding of E107-3 to the GUV surface. Both the hydrophobic side groups and the cationic characteristic of E107-3 (Figure 1.6) could promote the bilayer-binding process. Surface binding may not immediately induce the formation of bilayer defects; thus, no solutes are exchanged between the interior and exterior of the GUV (i.e., constant GUV volume). To accommodate the increase of the surface area, a fraction of the GUV protrudes into the micropipette. This explains the increase of the protrusion length during the first  $\sim 8$ -s period.

After reaching a maximum value, the protrusion length spontaneously decreases to near zero. Two possibilities could account for the behavior [40, 72, 74, 92]. The first one involves an invariant GUV surface area, while the GUV volume increases (by processes such as solute influx through finite-sized defects); the second one considers a constant GUV volume but the surface area decreases. A common scenario corresponding to the second possibility is lipid extraction from GUV bilayers [72, 74]. Our leakage experiment suggests that E107-3 can increase the bilayer

permeability to calcein. Therefore, it is plausible that exposure to E107-3 allows glucose/water molecules to translocate from the exterior to the interior of the GUV, thus increasing the GUV volume and decreasing the protrusion length. Solute influx, however, does not necessarily mean the formation of steady pores by E107-3, since transient defects also allow solutes to permeate through the bilayer. Lipid extraction accompanied by the decrease of the protrusion length has been observed for a broad spectrum of molecules [72, 74, 91]. We confirm the role of E107-3 in extracting lipids from planar bilayers by observing a double-bilayer structure in the presence of fusogenic calcium ions. Collectively, the decrease of  $L_P$  for aspirated GUVs is likely caused by two mixed processes of bilayer permeation and lipid extraction.

We use 5  $\mu\text{M}$  E107-3 for the aspiration experiment. For a typical GUV with a diameter of 40  $\mu\text{m}$ , the number of lipid molecules that the GUV contains is  $\sim 1.5 \times 10^{10}$  (lipid area  $\sim 0.65 \text{ nm}^2$  for POPC and POPG [93, 94]). When the GUV is submerged in 200  $\mu\text{L}$  of 5  $\mu\text{M}$  peptide solution, the estimated peptide to lipid ratio (P/L) is  $4.0 \times 10^4$ . This value is much larger compared to the P/L values used in the leakage experiment (P/L  $\sim 1$  for 100  $\mu\text{M}$  peptide). The different P/L values may account for the different kinetic responses in the aspiration and leakage experiments. We note that although the P/L value is large in the aspiration experiment, only a portion of the peptide molecules will be able to interact with the GUV within the time scale of Figure 3.3. This is illustrated by the root mean square displacement of glucose molecules. It takes  $\sim 33 \text{ s}$  for glucose to travel by 200  $\mu\text{m}$  in water (diffusion coefficient  $\sim 600 \mu\text{m}^2/\text{s}$  [119]). Therefore, for the time scale of the aspiration experiment, only a shell of peptide molecules surrounding the GUV will be able to interact with the GUV bilayer. Such a consideration will decrease the effective P/L in the aspiration experiment.

We use solution AFM to determine the effects of E107-3 on nanoscopic structural and mechanical properties of planar lipid bilayers. AFM height images reveal that E107-3 and melittin perturb lipid bilayers differently. Specifically, melittin perforates lipid bilayer by forming pore-like structures, while E107-3 only mildly increases the bilayer roughness by generating heterogeneous features that have a correlation length  $\xi$  of  $\sim 5\text{--}7$  nm.

To further explore the impact of E107-3 on lipid bilayer mechanical properties, we use AFM-based force spectroscopy. We find that E107-3 only slightly decreases the bilayer puncture force even at 100  $\mu\text{M}$ . This behavior is in contrast to the marked decrease of the bilayer puncture force when melittin is added (data not shown). The disparity further supports that E107-3 and melittin act by different mechanisms. We also analyze the force spectroscopy data by using an elastic deformation model. The bilayer area compressibility modulus  $K_A$  is found to decrease continuously from 246 to 150 mN/m when the concentration of E107-3 increases from 0 to 100  $\mu\text{M}$ . The large decrease of  $K_A$  (by 39%) contrasts with the mild decrease of the bilayer puncture force. This indicates that  $K_A$  might be a more suitable parameter to describe the impact of E107-3 on lipid bilayer mechanical integrity.

To explain our experimental data, we propose a bilayer interaction model illustrated in Figure 3.13. E107-3 contains one cationic group ( $R_1$ ) and three hydrophobic groups ( $R_2$ ,  $R_3$ , and  $R_4$ ) (Figure 1.6). After binding to the bilayer surface facilitated by electrostatic and hydrophobic interactions, the hydrophobic groups of E107-3 will insert into the hydrocarbon chain region. Inter-leaflet redistribution of the compound can be achieved by the flip-flop mechanism [120]. Due to the bulky adamantyl and phenyl groups of E107-3, the cohesive interaction between lipid chains is likely perturbed. Moreover, the compound only has ten atoms (carbon and nitrogen) along the backbone; therefore, its length is likely to be less than the thickness of one lipid

monolayer, potentially inducing vacancies within the hydrophobic core. Similar vacancies have been observed in simulations when coiled-coil peptides insert into lipid bilayers [121]. The peculiar architecture of E107-3 may cause rearrangement of neighboring lipids in both leaflets (Figure 3.13), resulting in a rougher bilayer as suggested by our AFM images (Figure 3.4). Local defects are formed by impaired lipid chain packing in the vicinity of the compound. The disrupted lipid chain packing enhances bilayer permeability, allowing small molecules (e.g., sugars and calcein) to translocate across the hydrophobic barrier. This explains our vesicle leakage data and serves as a potential mechanism (i.e., influx of solutes) for the behavior of the protrusion length  $L_P$  observed in our aspiration experiment.

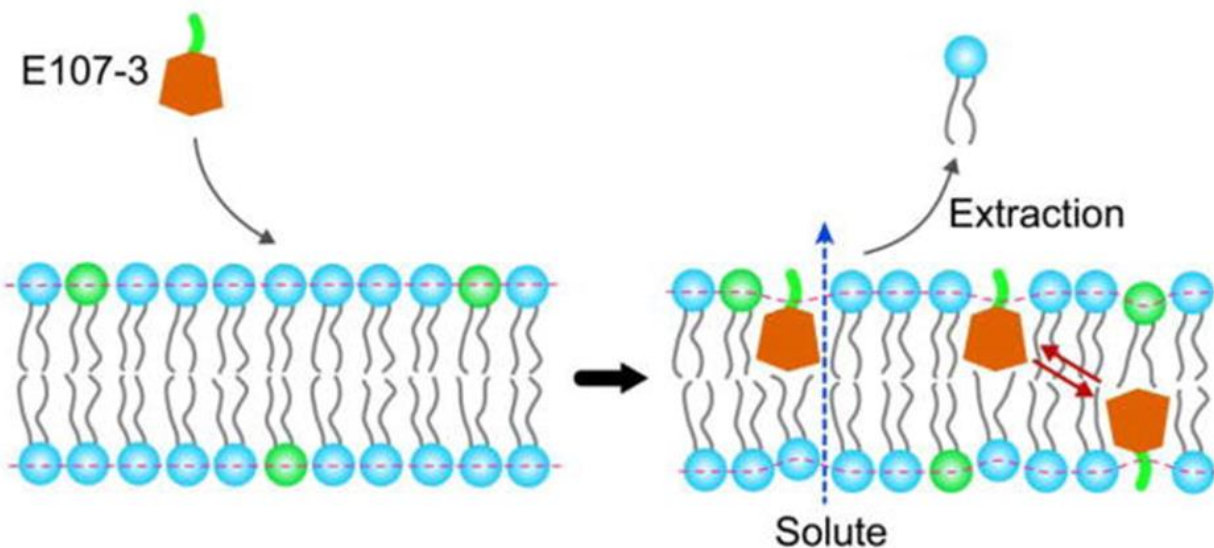


*Figure 3.13 A schematic diagram of bilayer disruption induced by E107-3. The lipid bilayer is composed of a mixture of POPC (cyan head) and POPG (green head) lipids. The amphipathic nature of E107-3 is illustrated by the green (hydrophilic) and brown (hydrophobic) colors. The insertion of E107-3 into the lipid bilayer causes rearrangement of neighboring lipids in both leaflets, resulting in a corrugated bilayer containing local defects that allow small molecules to permeate through the hydrophobic barrier. E107-3 can redistribute between the two leaflets by flip-flopping. The perturbation of bilayer integrity imparted by E107-3 is exacerbated by lipid extraction from the bilayer environment.*

In addition to the perturbation within the bilayer plane, our double-bilayer experiment shows that E107-3 can extract lipids from the bilayer environment. The lipid extraction effect of E107-3 is also consistent with the decrease of the protrusion length  $L_P$  observed in the GUV aspiration experiment. Moreover, lipid extraction contributes to the enhanced bilayer permeability observed in the calcein leakage experiment. Finally, we note that in addition to the hydrophobic groups, the cationic group of E107-3 may also contribute to the perturbation exerted on lipid bilayers. This is supported by theoretical calculation showing that electrostatic interaction increases the rate of tension-induced pore formation in lipid bilayers [122].

The viability of microbes is critically dependent on the structural and mechanical integrity of their membranous envelope. Our leakage experiment reveals that lipid bilayer permeability is increased by E107-3. Therefore, modulation of membrane permeability could be one mechanism employed by E107-3 in killing bacteria. Our force spectroscopy data show that E107-3 alters lipid bilayer mechanical properties by decreasing the bilayer puncture force and the area compressibility modulus. In line with our findings, a recent report by Henderson et al. showed that many antimicrobial peptides share a common capability of reducing the interfacial line tension of lipid membranes, resulting in impaired lipid membrane integrity [123]. Similarly, reduction of lipid bilayer bending rigidity has been observed for an array of AMPs, including alamethicin [124-126], melittin [127], and magainin [128]. Membrane material properties are essential to proper functions of many membrane proteins [129]. Therefore, E107-3 could also act by impairing bacterial membrane mechanical integrity. The two mechanisms could work synergistically. For example, weakened membrane mechanical properties could result in a larger probability of forming transient defects, thus increasing membrane permeability.

### 3.4 Conclusions

Here we report the effects of an antimicrobial peptidomimetic (i.e., E107-3) on structural and mechanical properties of POPC/POPG lipid bilayers. The compound was recently synthesized based on the acylated reduced amide scaffold and has been shown to exhibit good antimicrobial potency. Time-course and steady-state fluorescence spectroscopy measurements reveal that E107-3 induces membrane defects that allow calcein to permeate through the hydrophobic barrier. Compared to the bee venom antimicrobial peptide melittin, the leakage efficacy of E107-3 is two orders less, implying that disparate antimicrobial mechanisms might be used by the two agents. To obtain the kinetic response of individual GUVs exposed to E107-3, we use fluorescence microscopy-based micropipette aspiration experiment. We find that the protrusion length of the aspirated GUV first increases and then decreases to near zero. GUVs are ruptured once the protrusion length diminishes. The increase of the protrusion length is likely caused by initial surface binding of E107-3, resulting in GUV area expansion, whereas the decrease of the GUV protrusion length could be due to solute/water influx and/or lipid extraction. We use solution AFM to study the impact of E107-3 on nanoscopic structures of planar lipid bilayers. We find that unlike melittin, which produces pore-like structures, E107-3 only slightly increases the roughness of the lipid bilayer surface. We use a correlation length to characterize the length scale of the heterogeneous structures induced by E107-3. The correlation length  $\xi$  is found to be  $\sim 5\text{--}7$  nm. Finally, we use AFM-based force spectroscopy to determine lipid bilayer mechanical properties. We find a moderate decrease of the lipid bilayer puncture force  $F_P$  as the concentration of E107-3 increases from 0 to 100  $\mu\text{M}$ . We next apply a bilayer elastic deformation model to analyze the obtained force spectroscopy data. We find that the bilayer area compressibility modulus  $K_A$  is 246 mN/m for the POPC/POPG bilayer;  $K_A$  decreases to 202, 182, and 151 mN/m at 5, 20, and 100

$\mu\text{M}$  E107-3, respectively. To test the effect of lipid extraction by E107-3, we use a method involving double-bilayer formation. In the presence of calcium ions, a double-bilayer structure is obtained (by AFM imaging and force spectroscopy measurements) after adding E107-3 to a preformed POPC/POPG bilayer. Since the formation of a second bilayer requires lipid molecules that can only be provided by the original bilayer, our double-bilayer experiment demonstrates that E107-3 can extract lipids from planar bilayers. Together, our experimental data unambiguously show that E107-3 impairs lipid bilayer structural and mechanical integrity. The observed modulations are useful to elucidate the molecular mechanism used by E107-3 in killing bacteria

## 4. INTERACTION OF COLISTIN WITH LPS CONTAINING BILAYER AND E.COLI BACTERIA<sup>2</sup>

This chapter discuss about the permeability of the membrane depending on LPS content as the effect of antimicrobial peptide colistin. It also describes the micro and macro-cluster of lipids induced by colistin on LPS containing bilayer as well as effect of divalent cation Mg<sup>2+</sup> in cluster formation. Part of this chapter is published previously in ACS omega under the title ‘*Lipopolysaccharide -Dependent Membrane Permeation and Lipid Clustering Caused by Cyclic Lipopeptide Colistin.*’ in 2018.

### 4.1 Introduction

Polymyxins (A–E) belong to a group of cyclic lipopeptides with potent antimicrobial characteristics [130]. Figure 1.7 shows that the heptapeptide ring of polymyxins is enriched with the unusual cationic diaminobutyric acid (DAB); the C-terminus of the exocyclic tripeptide is fused to the macrocyclic ring, while the N-terminus is linked to a fatty acid tail (prominently 6-methyl-octanoic acid). Colistin known as polymyxin E was initially derived from the Gram-positive bacterium *Bacillus colistinus*. Colistin is effective at a few micromolar concentrations to inhibit bacterial growth or kill bacteria. Polymyxins, primarily polymyxin B and colistin, were used as broad-spectrum antibiotics for clinical application starting in the 1950s. Later clinical experiences showed that polymyxin-treatment was often accompanied with neurotoxic and

---

<sup>2</sup>“Reproduced with permission from Khadka, N.K., C.M. Aryal, and J.J. Pan, *Lipopolysaccharide-Dependent Membrane Permeation and Lipid Clustering Caused by Cyclic Lipopeptide Colistin.* *Acs Omega*, 2018. **3**(12): p. 17828-17834. Copyright 2018 American Chemical Society

nephrotoxic effects, although the toxicity was reversible upon discontinuation of the drug usage [131]. The potential toxicity rendered polymyxins less desirable compared to other antibiotics. The usage of polymyxins was gradually abandoned in the early 1980s. Recently, multidrug-resistant (MDR) bacterial pathogens, mostly Gram-negative species such as *P. aeruginosa*, *A. baumannii*, and *K. pneumoniae*, have emerged as a great health threat. Because of their potent antimicrobial activities and low susceptibility to bacterial resistance, polymyxins have received a renewed interest in combating MDR infections [132, 133]. In particular, polymyxins are currently used as last-resort drugs to treat infections (e.g., cystic fibrosis) caused by microbes that are resistant to almost all available antibiotics [134, 135].

The envelope of Gram-negative bacteria has a complex multi-layered architecture, including the outer membrane (OM), the cytoplasmic membrane, and a peptidoglycan layer located at the periplasmic space [136]. The OM of Gram-negative bacteria forms a permeability barrier that is essential to bacterial viability. The OM has an asymmetric organization; the outer monolayer is mainly composed of lipopolysaccharides (LPS), while the inner leaflet is formed by phospholipids. Compared to phospholipids, polyanionic LPS molecules are better suited for intermolecular interactions to form a supramolecular organization. Structurally, LPS can be divided into three regions: an amphipathic lipid A moiety, a hydrophilic oligosaccharide core (including the inner and outer cores), and an O-antigen chain. It is believed that strong intermolecular interactions of LPS bridged by divalent cations (e.g.,  $Mg^{2+}$  and  $Ca^{2+}$ ) are the primary mechanism of enhancing the OM stability and limiting the permeation of external agents such as lipophilic antibiotic compounds [137, 138].

Polymyxins have a high affinity for LPS molecules [139-142]. This is exemplified by the antiendotoxic effect of polymyxins in treating septic shock caused by free LPS molecules (also

known as endotoxins) [143]. The strong association of polymyxins with LPS also explains the formation of rod-shaped projections from the cell wall of Gram-negative bacteria when exposed to polymyxin B [144]. Although the exact mechanism underlying polymyxin functioning against Gram-negative bacteria remains an open question, impairment of the LPS layer is believed to play a crucial role in initiating the bactericidal activity. Polymyxin binding will cause the displacement of divalent cations that are important for stabilizing the LPS layer by linking phosphates of neighboring LPS molecules. A weakened LPS layer will allow more polymyxins (and other solutes) to traverse the OM [145, 146]. The mechanism was coined as the self-promoted uptake pathway [145]. Collectively, the first step of polymyxin functioning is to modify the structure and organization of the LPS-enriched OM bilayer. Subsequent bactericidal activity can be carried out by different mechanisms that are still not fully understood. A few of the proposed bactericidal mechanisms include the perforation of the cell wall [147], formation of molecular contacts between the OM and the cytoplasmic membrane [148], loss of enzymatic components [149, 150], and production of reactive oxygen species [151].

To elucidate the effect of polymyxins on the OM bilayer, many studies have used LPS-containing vesicles or monolayers. A selective examples include (i) electron microscopy showed that colistin disintegrated ribbon-like vesicular structures formed by isolated LPS [152]; (ii) electron spin resonance revealed that polymyxin B had a large impact on the packing property of LPS [153]; (iii) polymyxins inserted into LPS monolayers at the air-water interface as evidenced by an increase in the surface pressure [154, 155]; (iv) electrophysiological measurements showed that polymyxin B induced electrically active lesions in LPS-containing bilayers [156, 157]; (v) nuclear magnetic resonance (NMR) coupled with computational modeling were used to predict the molecular binding mode of polymyxin B and LPS molecules [158-160].

In contrast to the abundant studies of polymyxins interacting with LPS in vesicular or monolayer systems, only a few reports of polymyxin-LPS interactions in a planar bilayer setup have been made. A recent study used LPS/phospholipid mixtures (and deep rough LPS) to prepare oriented multilamellar stacks to mimic the OM bilayer; the authors then used X-ray diffuse scattering to explore the effect of colistin on mechanical properties of the LPS-containing bilayers [161]. Here we used solution atomic force microscopy (AFM) to investigate the effect of colistin on nanoscale topographic structures of LPS-containing lipid bilayers. Our AFM-based study is motivated by the facts that (i) AFM is a suitable technique to visually detect structural changes of lipid bilayers induced by membrane-active compounds and (ii) only two AFM-based studies have been reported on polymyxins interacting with LPS; one study was performed on a lipid A monolayer [162] and the other used biotinylated LPS to form a monolayer supported by a densely packed avidin layer [163].

In this studies, we first used vesicle leakage experiment to study changes in bilayer permeability caused by colistin. The obtained results revealed that colistin-induced bilayer permeation was dependent on the LPS fraction in LPS/phospholipid bilayers. We then used solution AFM to explore structural changes of planar lipid bilayers. Our AFM measurements showed that the effect of colistin on bilayer topographic structure was dependent on the LPS fraction and the peptide concentration. Importantly, we observed nanoscale clusters that are consistent with the complex formation of colistin and LPS molecules. The segregated lipid clusters could produce membrane lesions (i.e., cluster edges) that are consistent with our vesicle leakage data. We also found that both bilayer permeabilization and cluster development were inhibited by introducing magnesium ions into LPS-containing lipid bilayers. Results from our vesicle leakage

and solution AFM experiments provided useful insights into the mechanism that could be used by polymyxins in impairing the permeability barrier of the OM of Gram-negative bacteria.

## 4.2 Results

### 4.2.1 Vesicle leakage

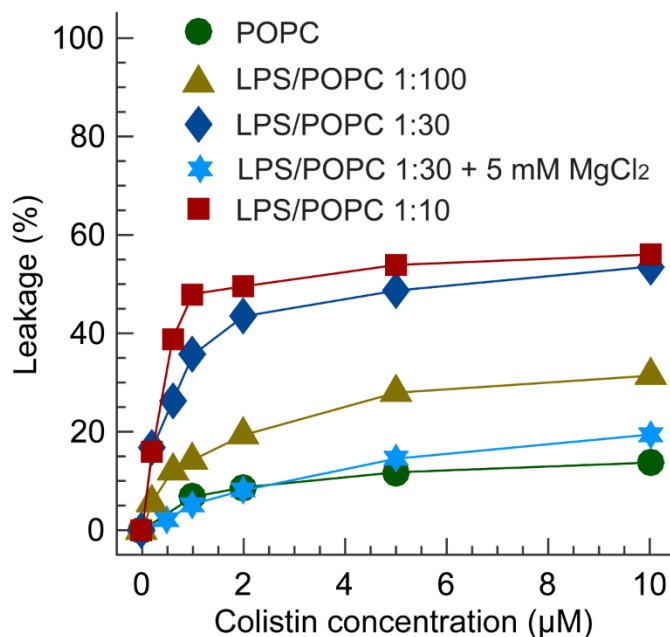


*Figure 4.1 Vesicle leakage induced by colistin as a function of the peptide concentration. Vesicles were prepared at several weight ratios of LPS/POPC. Vesicles with 5 mM MgCl<sub>2</sub> both inside and outside was used to examine the effect of magnesium ions. The measurements were performed after incubating vesicles with colistin for 20 h. Leakage of 0% corresponds to control vesicles, and leakage of 100% corresponds to the treatment with 20 mM Triton X-100.*

We used fluorescence spectroscopy to examine the effect of colistin on bilayer permeability. Lipid vesicles were prepared at several LPS/POPC weight ratios. Note that because the molecular weight of the isolated LPS is unknown, we use weight ratios for LPS/POPC bilayers in this study. Calcein-enclosed lipid vesicles were prepared by gel filtration. Fluorescence signal from control vesicles is small due to the self-quenching property of the fluorophore (i.e., calcein).

When colistin binds to lipid vesicles, the resulting increase in the bilayer permeability will cause an increase in the fluorescence signal. We have previously used this method to evaluate changes in bilayer permeability caused by different compounds [104, 164, 165].

Here we used vesicle leakage to measure changes in the bilayer permeability after incubating lipid vesicles with colistin for 20 h. The result is summarized in Figure 4.1. For the LPS-absent POPC vesicles, a maximum permeability increase of ~10% was observed. The addition of LPS at 1:100 yielded a maximum permeability of ~30% (10  $\mu$ M colistin). A further increase of the LPS/POPC weight ratio to 1:30 and 1:10 resulted in a maximum permeability of ~55% (10  $\mu$ M colistin). By comparing the maximum leakage % for LPS/POPC bilayers with different LPS fractions, we conclude that colistin-induced bilayer permeation is dependent on the LPS fraction.

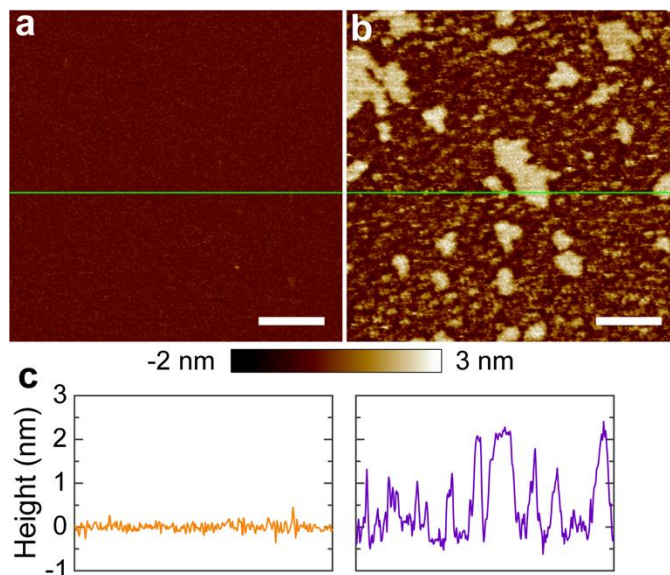


*Figure 4.2 Solution AFM images of an LPS/POPC 1:60 bilayer before (a) and after (b) exposure to 10  $\mu$ M colistin. Height scale is indicated by the color at the bottom. The same color bar is used for all AFM images in the study. Scale bars are 200 nm. (c) Height profile along the solid green lines in (a) and (b).*

In addition, because the maximum leakage % is <100% for all LPS/POPC bilayers studied, we conjecture that only a portion of the fluorophore molecules was released from lipid vesicles even when the maximum leakage was achieved. This indicates that colistin did not completely damage lipid vesicles as the surfactant Triton X-100 would. Lastly, we examined the effect of divalent cationic magnesium ions on bilayer permeabilization. This is done by preparing LPS/POPC 1:30 vesicles with 5 mM MgCl<sub>2</sub> both inside and outside. Figure 4.1 shows that the magnesium ions significantly suppressed the maximum leakage % such that the LPS/POPC 1:30 vesicles suspended in 5 mM MgCl<sub>2</sub> responded similarly to colistin as the POPC vesicles did. Therefore, magnesium ions abrogated the effect of LPS in enhancing bilayer permeabilization caused by colistin.

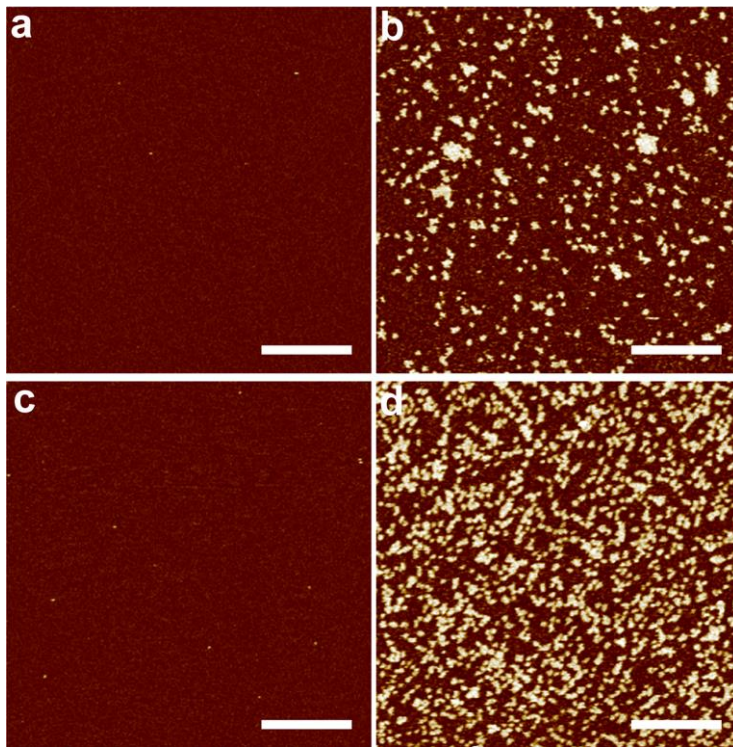


*Figure 4.3 Solution AFM images of an LPS/POPC 1:60 bilayer before (a) and after (b) exposure to 10  $\mu$ M colistin; solution AFM images of an LPS/POPC 1:30 bilayer before (c) and after (d) exposure to 10  $\mu$ M colistin. Height scale is 5 nm. Scale bars are 1  $\mu$ m.*

#### 4.2.2 AFM experiment on planar lipid bilayers

We conducted solution AFM measurements to visually detect nanoscale structural changes of LPS/POPC bilayers induced by colistin. Figure 4.2 shows the AFM images of an LPS/POPC 1:60 bilayer before and after exposure to 10  $\mu\text{M}$  colistin. The control bilayer exhibited a macroscopically homogeneous organization. The smooth surface structure is also indicated by the height profile along the bilayer surface (Figure 4.2c). After confirming the quality of the control bilayer, we used a syringe pump to inject a 10  $\mu\text{M}$  colistin solution. Figure 4.2b shows the modified bilayer structure after exposure to 10  $\mu\text{M}$  colistin. Numerous small clusters with a length scale of  $\sim 20$  nm were observed. Larger clusters with a length scale up to a few hundred nanometers were also present at several locations. For simplicity, we will refer to the smaller clusters as "nano-clusters", and the larger clusters as "macro-clusters" or "clusters". AFM is sensitive to the bilayer normal dimension. The height profile along an arbitrary path showed that the macro-clusters have a height of  $\sim 2$  nm above the background. The height of the nano-clusters is not well-defined by the height profile because the path does not always coincide with the center of the nano-clusters. Nevertheless, the nano-clusters have a height of  $\sim 1$ – $2$  nm as evidenced by the height profile.

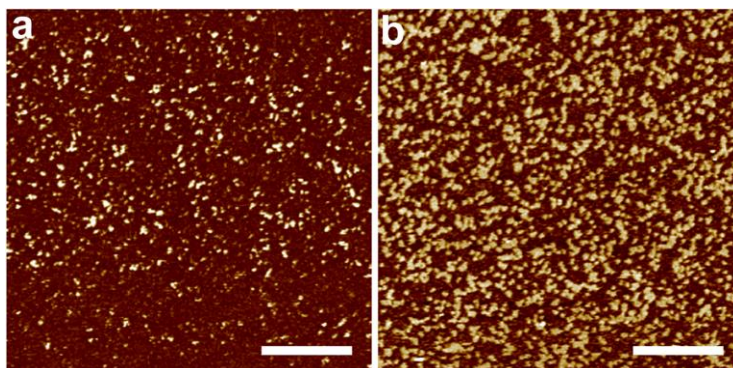


*Figure 4.4 Solution AFM images of an LPS/POPC 1:30 bilayer exposed to 5  $\mu\text{M}$  (a) and 10  $\mu\text{M}$  (b) colistin. Height scale is 5 nm. Scale bars are 1  $\mu\text{m}$ .*

After obtaining the preliminary data of bilayer restructuring, we are interested in the effect of the LPS fraction in regulating colistin-induced lipid clustering. We used AFM imaging to explore bilayer remodeling induced by colistin at two LPS fractions. Figure 4.3 shows the AFM images of two LPS-containing bilayers (i.e., LPS/POPC of 1:60 and 1:30) before and after treatment with 10  $\mu\text{M}$  colistin. Dispersed clusters with a length scale of a few hundred nanometers were observed for the LPS/POPC 1:60 bilayer (Figure 4.3b). (Note that Fig. 4b and Fig. 3b are similar except for the image sizes. The nano-clusters in Figure 4.2b are not distinguishable in Figure 4.3b.) Increasing the LPS fraction to 1:30 caused a marked increase in the number of the macro-clusters (Figure 4.3d). Despite the striking difference in their numbers, macro-clusters in both bilayers had a height of  $\sim 2$  nm. Collectively, our AFM experiment on two LPS/POPC bilayers with varying LPS fractions showed that the degree of lipid clustering induced by colistin is positively correlated with the fraction of LPS in LPS/POPC bilayers.

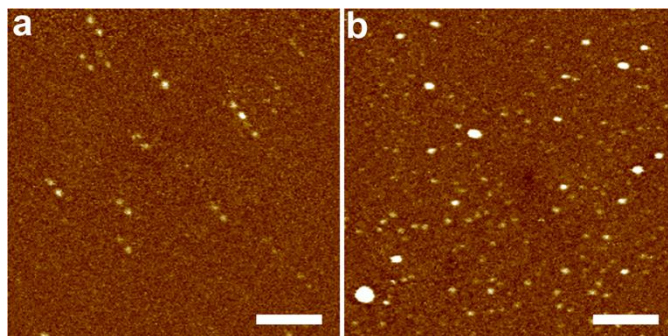


*Figure 4.5 Solution AFM images of an LPS/POPC 1:30 bilayer in 5 mM  $\text{MgCl}_2$  before (a) and after (b) exposure to 5  $\mu\text{M}$  colistin. Height scale is 5 nm. Scale bars are 200 nm.*

Next, we examined the effect of the peptide concentration in mediating colistin-bilayer interactions. We used an LPS/POPC 1:30 bilayer as the control system – AFM image of the control bilayer is the same as Figure 4.3c. Exposure of the control bilayer to 5  $\mu\text{M}$  colistin caused the formation of many macro-clusters (Figure 4.4a). The number of macro-clusters increased

significantly when the peptide concentration was increased to 10  $\mu\text{M}$  (Figure 4.4b). Note that the cluster height is similar at the two peptide concentrations. Altogether, our AFM measurements of an LPS/POPC bilayer showed that the number of macro-clusters induced by colistin is proportional to the peptide concentration.

Lastly, we investigated the effect of magnesium ions on colistin-induced bilayer remodeling. The control bilayer of LPS/POPC 1:30 was prepared from SUVs in the presence of 5 mM  $\text{MgCl}_2$ . AFM image showed that the control bilayer had a few small spots likely caused by magnesium ions-induced LPS aggregation (Figure 4.5a). Exposing the control bilayer to 5  $\mu\text{M}$  colistin in conjugation with 5 mM  $\text{MgCl}_2$  did not result in marked changes in the bilayer structure, although the number of small spots increased moderately (Figure 4.5b). Notice that the small spots in the presence of 5 mM  $\text{MgCl}_2$  had a different morphology compared to the nano-clusters in Figure 4.2b. Moreover, no macro-clusters were observed in the presence of 5 mM  $\text{MgCl}_2$  (Figure 4.5b). Overall, by comparing Figure 4.4a and Figure 4.5b (the same bilayer composition and peptide concentration), we conclude that magnesium ions inhibited the effect of colistin in inducing lipid clustering in LPS-containing bilayers.

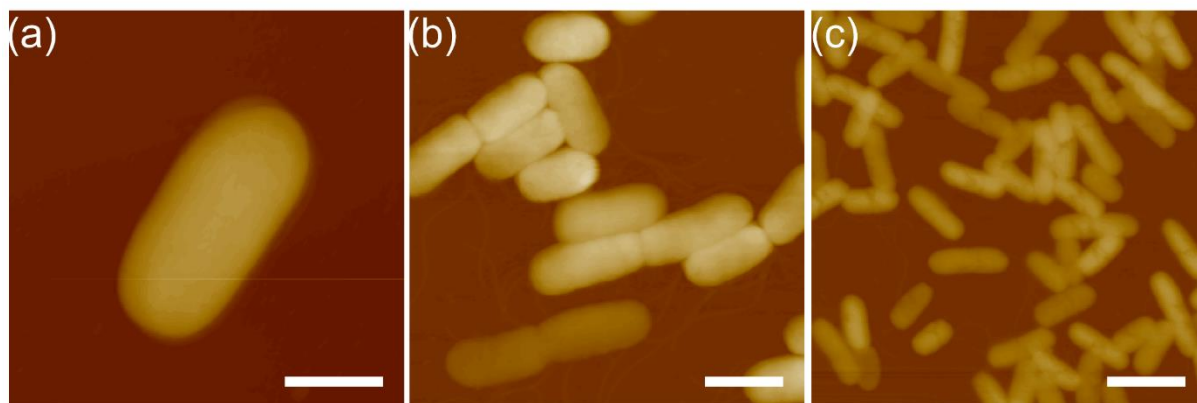


Figure 4.6 *E.coli* before adding colistin ( a), after adding 1 $\mu\text{M}$  (b) and 5  $\mu\text{M}$  colistin (c) for 30 minutes. Scale bar for (a), (b),and (c) is 1 $\mu\text{m}$  , 2 $\mu\text{m}$  ,4 $\mu\text{m}$  respectively.

### 4.2.3 Morphological changes induced by colistin in *E.coli*

We studied the effect of colistin on gram-negative bacteria, *E.coli* incubated at two concentration for the various time period. Figure 4.6 (a) shows the control bacteria with rod-shaped mostly smooth but also some with a slightly rough surface. Referring to minimal inhibitory concentration (MIC) for the susceptible strain of *E.coli* [166], we choose two concentration at near MIC value ( $1\ \mu\text{M}$ ) and above MIC value ( $5\ \mu\text{M}$ ) to investigate the morphological changes developed by the effect of colistin.

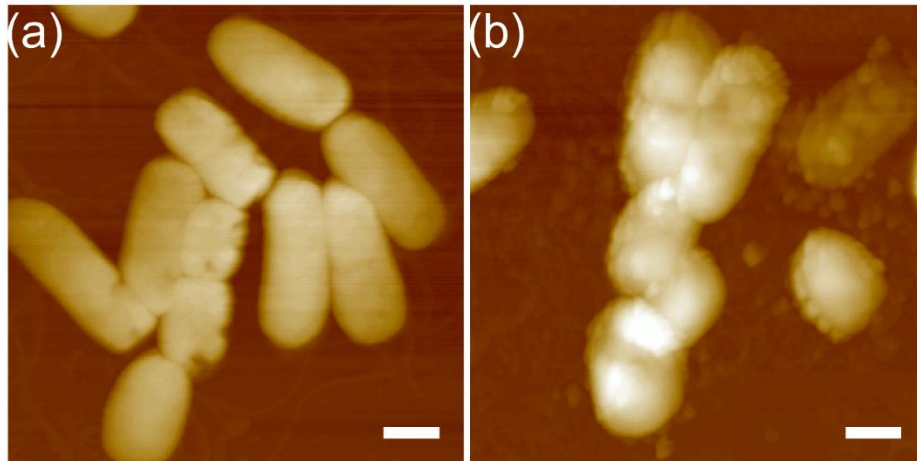
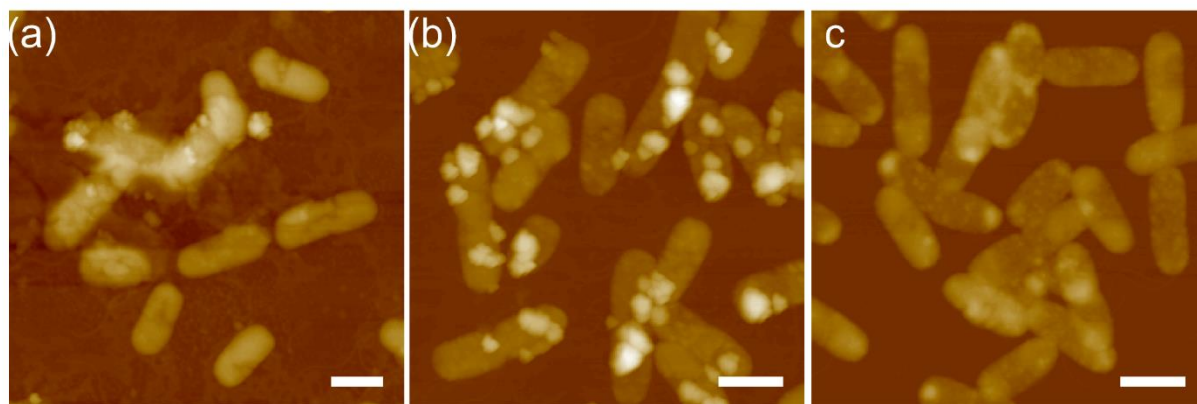


Figure 4.7 *E.coli* after adding  $1\ \mu\text{M}$  colistin and incubated for 1hr (a) and for 4 hours (b). Scale bar on the diagram is  $1\ \mu\text{M}$ .

*E.coli* incubated with colistin for 30 minutes have slight morphological changes Figure 4.6 b and c are the images taken after incubation with  $1\ \mu\text{M}$  and  $5\ \mu\text{M}$  colistin respectively. The edges seem to be corrugated, multiple cells develop cracked or wrinkled structure. However, the shape and content of the bacteria remain intact for both concentrations.

When the incubation time is increased to 1 hour,  $1\ \mu\text{M}$  colistin seems to produce a more dramatic effect.(Figure 4.7a) The surface of cells seems to develop bumps and valley. The edges

of the bacteria seem to have ‘chopped off’ regions indicating the deformity on the cells. Still, no visible lysis is developed. Further incubation of bacteria to 4 hours with 1uM colistin shows small structures lying around or near the cells (Figure 4.7b). This debris might be clusters of LPS as obtained in the bilayer experiment. The number of flagella decreased significantly too.



*Figure 4.8 Morphology of E.coli after incubated with 5μM colistin for 1hr (a), 2hrs (b), and 4hrs (c). Scale bar for each image is 2μM.*

Treatment of bacterial cells with 5 μM colistin for 1hour induced severe change in morphology (Figure 4.8a). Lots of cellular debris can be seen around the cells. Some of the cells contained segregation of mass, leaving an indentation in some part and raised bumps on the other region. Other cells have unusual raised mass content, most likely outside of the cell envelope. This might be the leakage of intracellular content accumulating at the cellular surface. Most of the cells have a similar accumulation of mass on their boundary when the incubation of colistin with same concentration was carried out for 2 hours (Figure 4.8b). These structures are obtained predominantly at the apex region for most of the cells. However, no regular pattern of evolving bumps is noticed. Further treating the bacteria for 4 hours with 5 μM (Figure 4.8c) colistin showed that the cells are flattened out with noticeable grainy surface. This might be due to losing the

cellular content after leakage, leaving behind the hollow enclosure. Some of the cells still have raised bumps at the apex region

### **4.3 Discussion**

In this study, we used fluorescence spectroscopy and solution AFM to interrogate the effect of colistin on membrane permeability and nanoscale structures. We are particularly interested in the relationship between the content of the OM-specific LPS and the degree of membrane restructuring induced by colistin. Our vesicle leakage experiment showed that colistin binding impaired the permeability barrier of LPS-containing lipid vesicles. The maximum leakage % was found to increase with the fraction of LPS. Addition of the divalent cationic magnesium ions inhibited the effect of LPS in enhancing bilayer permeabilization caused by colistin. We used solution AFM to determine the impact of colistin on nanoscale structures of LPS-containing lipid bilayers. The AFM experiment revealed that colistin caused a marked change in bilayer topography as evidenced by the formation of nano- and macro-clusters. We found that the degree of lipid clustering was dependent on the LPS fraction; more extensive lipid clustering was observed in lipid bilayers containing a larger fraction of LPS. In addition, more clusters were formed at higher peptide concentrations. Lastly, magnesium ions were found to antagonize lipid clustering induced by colistin.

We used a mixture of LPS and phospholipids to prepare vesicular and planar lipid bilayers. Our choice of the lipid composition was based on several considerations. Firstly, it has been shown that LPS/phospholipid bilayers are suitable for evaluating antimicrobial peptide-LPS interactions [167]. Secondly, there is no experimental evidence to definitively prove that the outer monolayer of the OM is exclusively composed of LPS [136, 168]. Interestingly, deep rough LPS was reported

to coexist with phospholipids in the outer monolayer of the OM in Gram-negative bacterial mutants [169]. Thirdly, the antibacterial activity of polymyxins is correlated with the content (and the chemical structure) of LPS. Complete loss of LPS was reported to serve as a mechanism for developing polymyxin-resistance by *A. baumannii* [170]. Similarly, LPS in cell wash solution was found to reduce the susceptibility of *P. aeruginosa* to colistin [171]. Collectively, studies of colistin interacting with LPS/phospholipid bilayers are useful to reveal the mechanism of OM permeation caused by polymyxins.

Owing to their opposite charge states, colistin and LPS can form stoichiometric complexes [139, 172]. The strong binding affinities of polymyxins to LPS have been broadly demonstrated by using fluorophore-tagged polymyxins [141, 142]. There are two driving forces directing the recognition of polymyxins toward LPS. The initial binding is facilitated by long-range electrostatic interactions between the negatively charged phosphates of LPS and the positively charged DAB of polymyxins. After initial binding, hydrophobic interactions between the hydrophobic tails of the lipid A motif of LPS and the hydrophobic domains of polymyxins can further increase the peptides' binding affinity. Many efforts have been made to elucidate the complex structure of polymyxins binding to LPS at a molecular level. A comprehensive summarization can be found in the review work by Velkov and coworkers [173]. In essence, the polycationic heptapeptide ring of polymyxins resides in the vicinity of the interface between the lipid A motif and the oligosaccharide core, while the acyl tail of polymyxins penetrates into the hydrophobic core of LPS. The proposed complex models are in line with the electrostatic and hydrophobic driving forces in stabilizing the binding of polymyxins to LPS. Unlike polyanionic LPS, zwitterionic phospholipids have a weak association with polymyxins [174-177].

The distinctive binding affinities of colistin to LPS and POPC are likely responsible for the nano- and macro-clusters observed in our AFM experiment. Our observation of lipid clustering has some similarity to an earlier study, which used a monolayer formed by *E. coli* total extract (no LPS) [178]. Although their AFM experiment was performed in air, the authors obtained circular protrusions (height of ~1 nm) with a radius of 20 nm or 120 nm, depending on the concentration of polymyxin B. Another study using fluorescence polarization also reported domain formation of polymyxin B and phosphatidic acid in the presence of phosphatidylcholine [179]. To explain the clusters observed in our AFM experiments, we propose a schematic model of colistin bound to an LPS/POPC bilayer (Figure 4.9). The insertion of colistin causes lipid redistribution such that LPS and colistin segregate away from POPC to form isolated clusters. The cluster and the POPC patch have a height difference of ~2 nm because of the bulky macrocyclic ring of colistin (and the ordered oligosaccharide core of LPS). The probability of cluster formation is larger at higher LPS contents (and colistin concentrations). Therefore, the proposed model is in line with our observation of lipid clustering as a function of the LPS fraction (and the peptide concentration). Magnesium ions have a strong binding affinity to LPS [140]. Introduction of magnesium ions will competitively inhibit the binding of colistin to LPS [180]. Consequently, magnesium ions will reduce the development of LPS-colistin clusters (Figure 4.9).

Our vesicle leakage experiment showed that colistin increased the permeability of LPS/POPC bilayers; the maximum leakage % increased with the LPS fraction. Membrane perforation is a popular mechanism proposed for the bactericidal activity of polymyxins. LPS tends to decrease bilayer permeability by having a tighter packing of acyl chains [181]. Permeability enhancement of LPS-containing bilayers (including the OM) can be achieved by pore formation or an alteration in lipid packing [145, 168, 182].

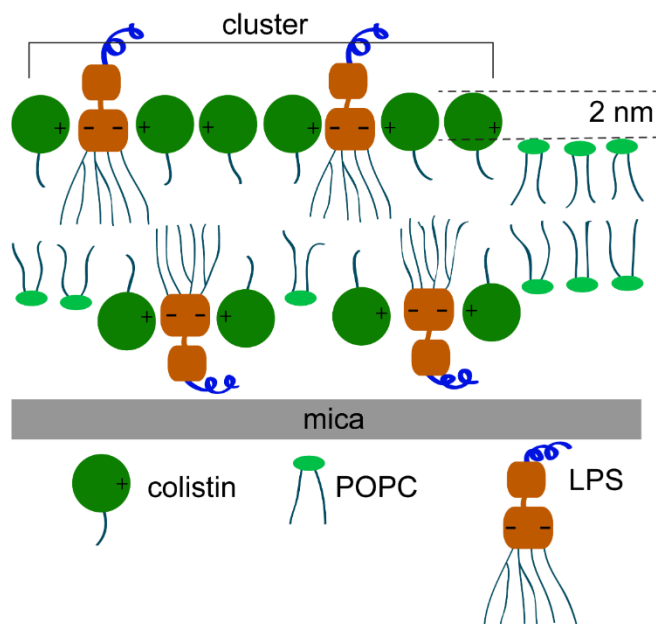


*Figure 4.9 A schematic diagram depicting the proposed mechanism of colistin-induced clustering of LPS molecules in mica-supported planar bilayers. The insertion of colistin into the LPS/POPC bilayer causes a lateral redistribution of the LPS molecules. LPS-enriched clusters are formed by electrostatic interactions between colistin and LPS. The protrusion of colistin macrocyclic ring (and LPS oligosaccharide core) could account for the 2-nm height of the clusters observed in AFM imaging. Owing to the discontinuity between the cluster and the rest of the bilayer, solutes will have a larger probability of permeating through the cluster edge. The model also predicts that bilayer permeability is positively correlated with the total length of the cluster perimeter.*

Based on electrophysiological measurements, Seydel and coworkers proposed pore-like lesions induced by polymyxins in asymmetric LPS bilayers [156, 157]. Our high-resolution AFM imaging did not show transmembrane pores induced by colistin. Note that we have previously observed <10 nm-sized pores using the same AFM setup [89]. Instead of transmembrane pores, we argue that the hypothetical lesions could correspond to cluster edges proposed in our lipid clustering model. Owing to the discontinuity (and the height mismatch) at the edge of LPS-colistin clusters, solutes will have a larger probability of permeating through the cluster edge. The total length of the cluster perimeter increases with the LPS fraction. Therefore, our lipid clustering model can account for the leakage behavior as a function of the LPS fraction in LPS/POPC

vesicles. Because magnesium ions inhibited cluster development (Fig. 6), the probability of solutes permeating through cluster edges is significantly reduced. Therefore, our lipid clustering model also supports the role of magnesium ions in abrogating colistin-induced bilayer permeabilization.

#### **4.4 Conclusions**

Here we report the effect of the cyclic lipopeptide colistin on membrane permeability and nanoscale structures of LPS-containing lipid bilayers. Fluorescence spectroscopy-based vesicle leakage experiment revealed that colistin binding impaired bilayer integrity, leading to an enhancement of the bilayer permeability. The maximum increase in the bilayer permeability was positively correlated with the LPS fraction in LPS/phospholipid bilayers. Addition of the divalent cationic magnesium ions suppressed the effect of LPS in enhancing bilayer permeabilization. We used solution AFM to gain a structural perspective of colistin-induced membrane remodeling. We found that colistin caused the formation of nano- and macro-clusters that protruded from the bilayer by  $\sim 2$  nm. Moreover, cluster development was enhanced by increasing the fraction of LPS or colistin concentration but abolished by magnesium ions. To explain our experimental data, we propose a lipid clustering model where LPS and colistin form large-scale clusters that are segregated from the POPC patch. The discontinuity (and the thickness mismatch) at the cluster edge will create a passage that allows solutes to permeate through. The degree of bilayer permeation is proportional to the total length of the cluster perimeter. Because more clusters are formed at higher LPS contents, our lipid clustering model supports the vesicle leakage data.

## **5. PORE FORMATION INDUCED BY AMPHIPATHIC HELIX H0 OF ENDOPHILIN BAR DOMAIN ON PLANAR LIPID BILAYER**

### **5.1 Introduction**

The BAR domain-containing protein superfamilies' are associated with various cellular activities, several of which are guided by membrane curvature sensing and generation. BAR domains consist of coiled-coil 3- $\alpha$  helices' monomers of roughly half cones whose outer surface is enriched with hydrophilic residues and inner surface with hydrophobic ones[183]. The hydrophobic interaction between the internal surfaces of the monomers, arranged in opposite direction, results in a symmetric BAR dimer consisting of the core with bundled six helices and two arms [183]. During this coupling, the hydrophobic surfaces are buried in the dimer contact area [183] but forming an inner surface enriched with positive charges [184, 185]. Based on the crystal structures, the superfamily of BAR proteins are categorized as i) classical BAR ii) N-BAR iii) I-BAR iv) F-BAR [186].

Endophilin, in addition to the BAR domain, consists of N-terminus helix H0, a variable length middle region and a src homology domain 3 (SH3) region [187, 188]. While SH3 domain binds with proline-rich dynamin[189] and synaptojanin [190] during the process of synaptic vesicle endocytosis, the BAR domain is responsible for sensing [191] and generating membrane curvature[186]. At lower BAR protein concentration, it works as a membrane sensing whereas at higher concentration it can deform membrane and induce membrane curvature resulting tubulation and vesiculation [186, 191]. N-BAR domains are suggested to bend membranes by two mechanisms. The concave surface of the BAR region is suggested to form a scaffold on the

membrane substrate, predominantly with negatively charged lipid bilayers [191, 192]. Upon binding to a lipid membrane, the unstructured N-terminal region of N-BAR assembles to an amphiphilic helix H0 [193, 194]. The other mechanism suggests that the bending formation occurs by inserting this helix H0 in the plane of the membrane. The midpoint of this helix embedded aligns to the phosphate level of lipid headgroup on the proximal bilayer leaflet [193, 195]. This is known as the wedging mechanism. Both mechanisms are shown to be highly coordinated for working of endophilin [196]. The helix H0 is suggested to be responsible for sensing membrane curvature through hydrophobic insertion in the region-containing lipid packing defects [195]. Simulation work has shown that folding of helix H0, which is mediated by packing defects, is favorable for positive curvature surfaces rather than flat or negative curvature surfaces [197]. However, the role of helix H0 in the generation of molecular surface curvature is yet debatable. Deletion of helix H0 in endophilin followed the linear sorting with membrane curvature, indicating membrane curvature sensing capability [198] and tubulation activity with amphiphysin [191]. Such amphipathic inserts are also found in other proteins like epsins [199], and G-proteins [200].

Most of the experiments, with either wild type or mutant BAR domains, are performed with vesicles or tubules that have curvature surfaces [191-194]. Here, we visualize the modification on the surface of planar supported bilayer containing different lipids, induced by amphipathic helix H0 of the endophilin A1 using AFM. This N-terminal containing peptide has 1-24 residues of human endophilin A1 with an amino acid sequence of MSVAGLKKQFHKATQKVSEKVGGA. We use the AFM topographic images to observe the modulation induced by endophilin helix H0 on the lipid bilayers.

## 5.2 Results

We studied the effect by endophilin helix H0 on the supported bilayers with different composition using fluid AFM.

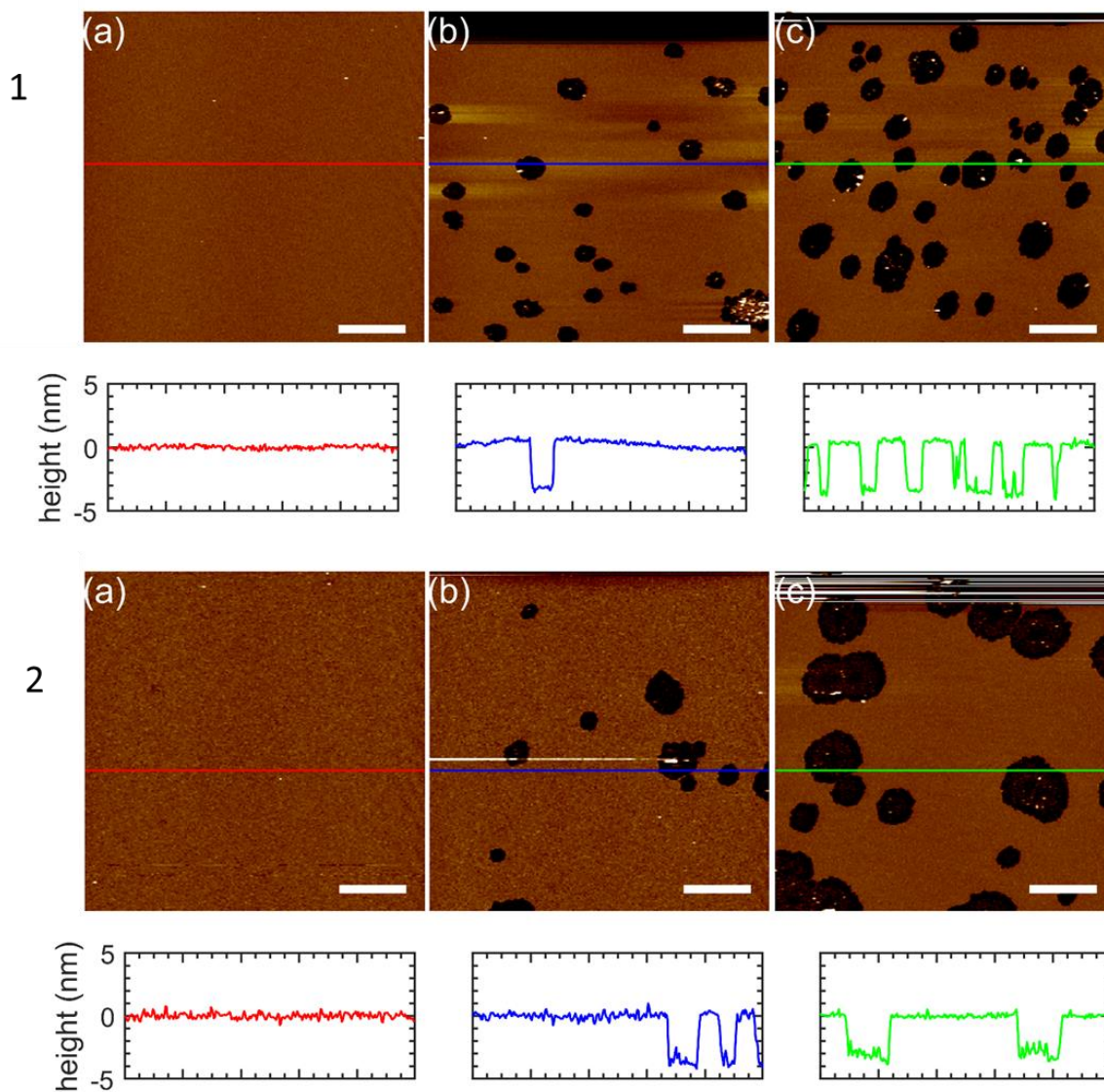


*Figure 5.1 Mica supported lipid bilayers incubated with helix H0 of endophilin. POPC (1) and POPC/POPE (2) bilayers before endophilin helix H0 incubation (a) and after 0.2  $\mu\text{M}$  (b) 0.5  $\mu\text{M}$  (c) incubation. Scale bars for all the images are 2 $\mu\text{m}$ . Height profile of the lines across the figures are shown below the images. The depth of the pores for all the images are around 4 nm.*

### 5.2.1 Endophilin helix H0 in neutral bilayer

We prepared supported lipid bilayer containing POPC or POPC+30mol % POPE, now on termed as POPC/POPE to investigate the effect by amphipathic helix H0 of endophilin N-BAR domain. Figure 5.1 (1a) shows the smooth POPC, and Figure 5.1(2a) shows POPC/POPE bilayers before adding the endophilin helix H0 in them.

The bilayers were treated with either 0.2 or 0.5  $\mu\text{M}$  endophilin helix H0 solution in ultrapure water. Within less than 10-minute incubation with the peptide, the POPC bilayer was perturbed by generating pores of different sizes. This indicates that the helix H0 is able to interact with bilayer relatively quick. The height profile of the pores formed on the bilayer is  $\sim 4\mu\text{m}$ . This indicates that the defects are across the bilayer, forming transmembrane pores. Nearly spherical pores with slight variation in size are formed in the bilayer. With the increased concentration of endophilin helix H0 (0.5  $\mu\text{M}$ ), and equal incubation time (around 10-minutes), the number as well as the size of pores generated on the bilayer increased. At this concentration, the size of the pores formed can be categorized into three distinct classes: small, medium and large size. This multiple sized pore formation might be the disruption at a different stage or caused by distinctive subunit complexes. At higher concentration endophilin (at 2 $\mu\text{M}$ ), the bilayer was completely washed away.

Intrestingly, the number of pores formed in POPC/POPE bilayers as shown in Figure 5.1 (2) are lesser than the ones obtained in POPC alone bilayer. The depth of the pore is similar to the ones obtained in POPC bilayer incubated with the helix H0. However, for alike concentrations, the size of the pore in POPC/POPE bilayer was larger than observed in POPC lipid bilayer.

### 5.2.2 Endophilin BAR helix H0 in negatively charged bilayer

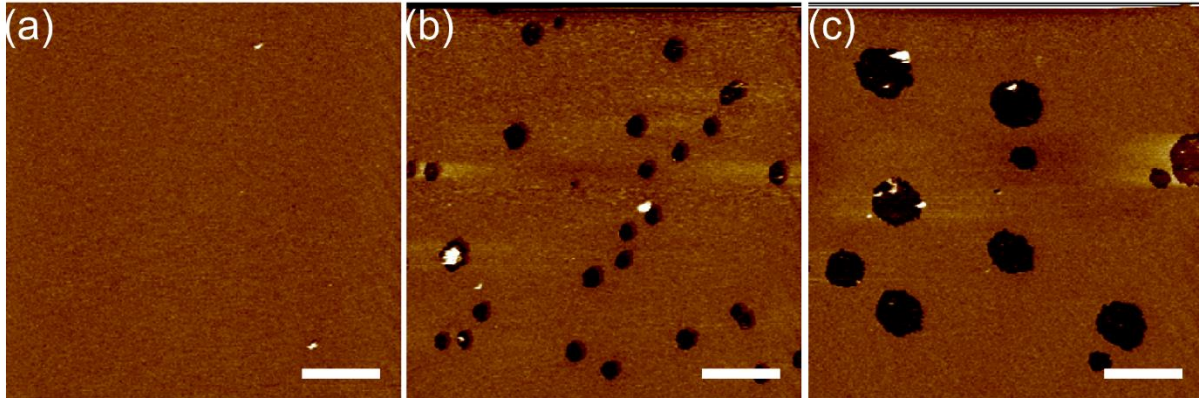


*Figure 5.2 POPC/POPG bilayer treated with different concentration of endophilin helix H0. Bilayer before helix H0 treatment (a) After 0.2  $\mu\text{M}$  (b) and after 0.5  $\mu\text{M}$  (c). Endophilin helix H0 treated images were acquired in less than 10 minutes of exposure time. All the scale bars are 2 $\mu\text{m}$  size*

To investigate the effect of endophilin helix H0 in the planar bilayer containing anionic lipid, we prepared bilayer of POPC/20 mol % POPG (POPC/POPG). We treated the bilayer with endophilin helix H0 at a concentration of 0.2  $\mu\text{M}$  and 0.5  $\mu\text{M}$ . The disruption induced by lower concentration endophilin helix H0 is similar to the damage induced in POPC bilayer at the equivalent concentration. However, the disruption caused by 0.5  $\mu\text{M}$  helix H0 is in a lesser extent than the disruption caused in a zwitterionic lipid bilayer at the same concentration.

### 5.2.3 Endophilin BAR helix H0 with POPC/ cholesterol bilayer

We studied the effect of endophilin helix H0 in the bilayer containing cholesterol. This is important because sterols like cholesterol are the major component of the plasma membrane and modulator for membrane fluidity. Tinier transmembrane pores were formed in the bilayer containing POPC+30mol% cholesterol incubated with 0.2  $\mu\text{M}$  helix H0 for ~10 minutes (Figure 5.3(b)). The size of the pore is relatively smaller and does not increase with an increase in the helix

H0 concentration (Figure 5.3(b)). Nevertheless, the number of pores formed in the bilayers are somewhat similar to the pores formed in POPC bilayer.

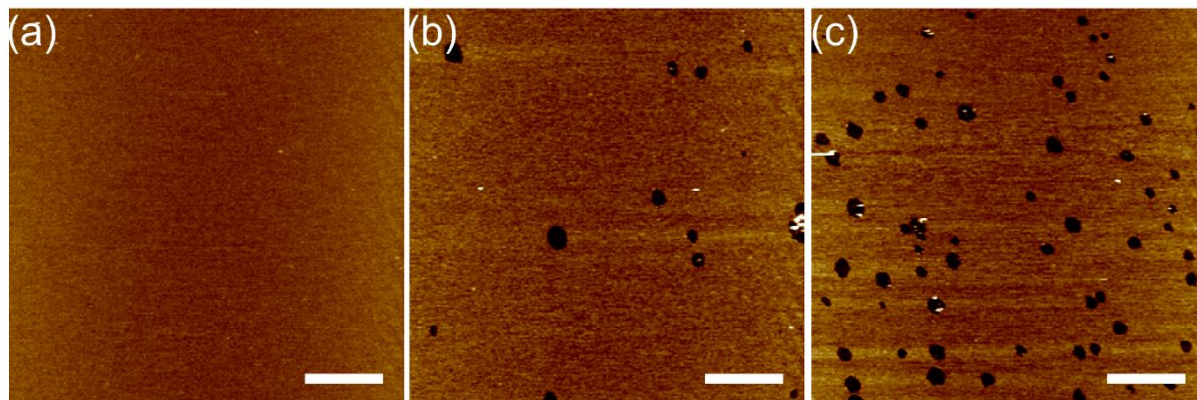


*Figure 5.3 POPC/Chol. bilayer treated with endophilin helix. Bilayer before treating with H0 (a) and after treating the bilayer with 0.2  $\mu$ M (b), and 0.5  $\mu$ M (c) concentration. All the scale bars are 2 $\mu$ m size*

#### **5.2.4 Time course effect on POPC/Cholesterol**

The images obtained after incubating POPC/Chol bilayer with 0.2  $\mu$ M endophilin A1 helix H0 at different time-period shows the changes seen in the bilayer perturbation as in Figure 5.4. The nature of pore formation remains almost the same over the image acquisition time frame. However, the number of pores formed remains constant after at least 20 minutes of incubation with endophilin helix H0. Variation in size of the pores is still observed even in longer incubation time. We did not notice any healing of bilayer perturbation within almost an hour's observation. A similar experiment performed earlier with endophilin N-BAR suggested the healing of sliver formation in an anionic bilayer [201]. This might suggest that the amphiphilic helix is not able to heal the bilayer, but a complete N-BAR domain might be able to do so.

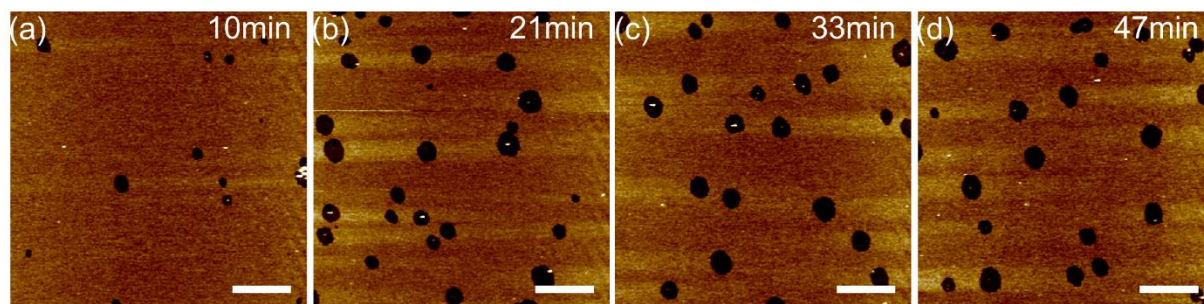


*Figure 5.4 Time dependent effect of helix 0 on POPC/Chol bilayer. Images are taken as the bilayer was exposed to 0.2 $\mu$ M endophilin helix H0 for 10 minutes (a) 21 minutes (b), 33 minutes (c), and 47 minutes (d). The number and size of the pore formation were saturated after 33 minutes incubation period.*

For most of the lipid bilayers incubated with endophilin helix H0, around the center of the pores, small bright spherical structures were observed. Interestingly, the washed away POPC bilayer surface by 2  $\mu$ M endophilin concentration contained mesh-like features built of similar spherical structures. The height of these structures is comparable with the height of the bilayer. These spherical structures might be the adhered remnant helix H0-bilayer cluster or H0 oligomers. The bright spots might be due to loosely attached bilayer clusters, which are attracted to the cantilever tip and pulled away during scanning.

### 5.3 Discussion

Here, we study the interaction of the N-terminal amphipathic helix H0 of the endophilin1 BAR domain on planar lipid bilayer using AFM in the fluid phase. We observed transmembrane pores generated in all the lipid species bilayer that we used for our experiment. This is the first kind of studies on planar lipid bilayer with endophilin N-terminal helix H0 alone for membrane modification.

Our selection for the concentration of the endophilin helix H0 is near to and higher than the concentration of endophilin found in the proximity of the site during the generation of synaptic

vesicles( $\sim 1\mu\text{M}$ )[193]. However, the concentration we use does not necessarily refer to the quantity that is bound to the surface of the bilayer. Nature of insertion of the amphiphilic helix in the monolayer exposed to it is in question. This insertion, not transmembrane, generates an expansion which is resisted by the other monolayer. Hence, to minimize this stress, the membrane must bulge or protrude towards top monolayer[202]. In addition, the interaction between helix H0 regions of different N-BAR endophilin during deep insertion has been reported in an earlier study [203]. The lower concentration of endophilin in the bilayer is found to be a promoter of the membrane curvature sensing while the higher concentration promotes vesicle formation or tubules generation [204]. We believe similar protrusion or cellular structures are generated with helix H0 after insertion into the membrane. However, in the flat bilayer, while scanning with AFM tip, such formed structures or protrusion might be disrupted and dragged away during the imaging process leaving behind the transmembrane pores. Additionally, the size of the pores formed on the bilayers is much larger than the typical size of the vesicles/neck of tubules formed by endophilin N-BAR. We attribute this to the extensive pairing of H0 helices' binding to a site of probable packing defects. A similar AFM study on lipid bilayer was performed earlier with endophilin NBAR domain showing the sliver formation at higher concentration [201].

Another noticeable feature of the disruption mechanism is the edges of the defect. The edges are not smooth but consist of very uneven horizontal protrusions. This implies that the extraction of lipids from the bilayer by helices is carried non-uniformly.

Contrary to the formation of slivers with the NBAR domain only on anionic lipid-containing bilayer, this helix H0 generated transmembrane defects on the bilayers containing both negatively charged lipid and purely neutral lipid. A possibility of binding of the helix H0 to the neutral bilayer, though weakly, has been suggested [194]. We believe that this binding is due to

hydrophobic interaction with the lipid bilayer and not electrostatic one. The binding is strong enough for the insertion on the outer monolayer. Eventually, this incorporation of helix H0 in the bilayer is able to generate morphological structures or bulges which when scanned with AFM are disrupted by the tip, and observed as defects in the bilayer.

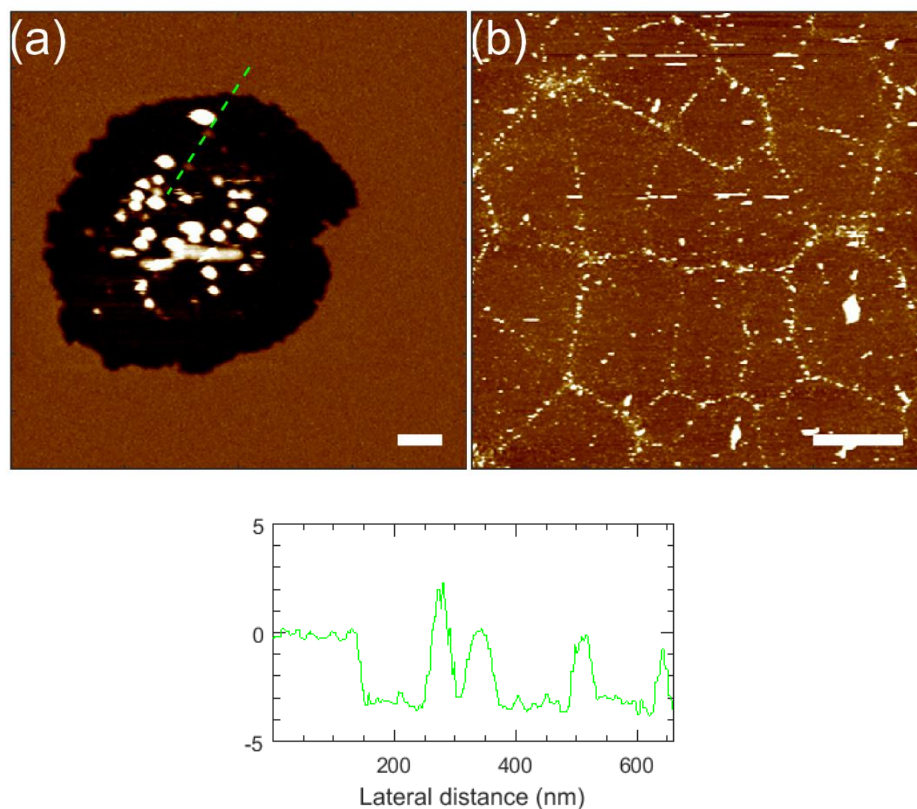


*Figure 5.5 POPC/POPE bilayer exposed to 0.5 $\mu$ M helix H0 concentration (a) and POPC bilayer with 2 $\mu$ M helix H0 concentration (b). Scale bars are at 0.2  $\mu$ m and 2 $\mu$ m respectively. Height profile of dotted line across the image (a) is shown below the image.*

Furthermore, since cholesterol is one of the important components of membrane bilayer influencing the fluidity and thickness, we studied the effect of helix H0 in the supported bilayer containing cholesterol. The influences on the peptides in presence of cholesterol have been shown

in a number of studies. In our studies, the size of the pores generated on the cholesterol-containing bilayer were smaller than the bilayer without it. This might suggest that the helix H0 is prone to attach with more fluidic bilayer and generate larger transmembrane defects.

#### **5.4 Conclusion**

In this study, we investigated the effect of amphiphilic helix H0 of endophilin BAR domain on the planar lipid bilayer. This amphiphilic helix is suggested to insert in the bilayer during the remodeling of the cell membrane. Endophilin helix H0 is found to bind with the planar bilayer without showing the lipid specificity. Transmembrane defects are observed on the bilayer instantly when scanning with the AFM. The number and size of the defects saturated below 30 minutes of incubation time with the cholesterol-containing bilayer. Our experiment with amphiphilic helix H0 of endophilin suggests the interaction with the planar bilayer is independent of lipid type.

## 6. CONCLUSIONS AND FUTURE DIRECTIONS

### 6.1 Conclusion

The purpose of this work is to study the interaction of bio-medically relevant macromolecules with the model lipid bilayers. We studied the peptidomimetics E107-3 and colistin as a compound related to treatment for drug-resistant species. Along with, we also studied the effect of N-terminal amphipathic helix H0 of endophilin on the solid supported lipid bilayer membrane. A number of techniques like vesicle permeability, aspiration of the GUV, and mostly fluid AFM were used during studies. We found out that the potential antimicrobial peptidomimetics E107 is able to permeate through the membrane inducing nanoscopic heterogeneous structures. We also found that the puncture force and membrane compressibility modulus decreases with increasing E107 concentration incubated on the bilayer. Membrane permeability of the LPS containing vesicles is enhanced with increased colistin concentration. Increment in membrane permeability is also positively correlated with increased fraction of LPS content on vesicles. However, the addition of magnesium ions diminishes the effect of increased permeability with LPS containing vesicles. Along with raised membrane permeability, colistin is able to form nanoscopic and macroscopic clusters protruded ~2nm on the surface of LPS containing bilayer. We observe the generation of transmembrane defects by the amphiphilic helix H0 of an endophilin BAR domain on both anionic and purely zwitterionic lipid supported bilayer as observed by the AFM.

## 6.2 Future Studies

The rapid evolution of antimicrobial drug resistant species is demanding immediate attention to seek effective treatment. Many drug resistant species are found to modulate their membrane to hinder the effect of the antibacterial agents. In this scenario, the importance of the study about the antibacterial agents with the bacterial membrane mimicking model is even magnified. A further detailed study in this field with more diverse instruments and methodology is required to get a better understanding. This includes the study of real bacterial cells, both susceptible and resistant, with the antimicrobial agents. A more detailed study on change in mechanical properties of the outer membrane by antimicrobial agents of such species is essential. And in-depth understanding of surface modification of bacterial cells by antimicrobial agents helps to design and develop effective treatment agents or methods.

Moreover, the studies with N-BAR endophilin amphiphilic helix H0 is limited to only flat supported bilayer with certain lipid species. Further study of this helix H0 with other curvature bilayers like GUVs is essential. More robust methodologies needs to be used to decipher the binding mechanism of endophilin helix H0 on membranes. Additionally, the study in the planar bilayer with wild type and other mutants of the BAR domain will definitely provide a better understanding of the curvature generation and sensing mechanism.

## 7. REFERENCES

1. Mitra, K., T. Ubarretxena-Belandia, T. Taguchi, G. Warren, and D.M. Engelman, *Modulation of the bilayer thickness of exocytic pathway membranes by membrane proteins rather than cholesterol*. Proceedings of the National Academy of Sciences of the United States of America, 2004. **101**(12): p. 4083-4088.
2. Watson, H., *Biological membranes*. Essays Biochem, 2015. **59**: p. 43-69.
3. Singer, S.J. and G.L. Nicolson, *The fluid mosaic model of the structure of cell membranes*. Science, 1972. **175**(4023): p. 720-31.
4. Nicolson, G.L., *The Fluid-Mosaic Model of Membrane Structure: Still relevant to understanding the structure, function and dynamics of biological membranes after more than 40 years*. Biochimica Et Biophysica Acta-Biomembranes, 2014. **1838**(6): p. 1451-1466.
5. Coskun, U. and K. Simons, *Cell membranes: the lipid perspective*. Structure, 2011. **19**(11): p. 1543-8.
6. Vittorio Luzzati, H.D., Annette Gulik, Tadeusz Gulik-Krzywicki, Paolo Mariani, Rodolfo Vargas, *The cubic phases of lipids*, in *Studies in Surface Science and Catalysis* 2004. p. 17-40.
7. Koynova R1, T.B., *Transitions between lamellar and non-lamellar phases in membrane lipids and their physiological roles*. OA Biochemistry, 2013.
8. Evans, D.F. and H. Wennerström, *The colloidal domain: where physics, chemistry, biology, and technology meet*. 1999.

9. Khandelia, H. and I. Vattulainen, *Lipid Organization, Aggregation, and Self-assembly*, in *Encyclopedia of Biophysics*, G.C.K. Roberts, Editor. 2013, Springer Berlin Heidelberg: Berlin, Heidelberg. p. 1273-1280.
10. Spooner, M.J. and P.A. Gale, *Anion transport across varying lipid membranes - the effect of lipophilicity*. *Chemical Communications*, 2015. **51**(23): p. 4883-4886.
11. Koebnik, R., K.P. Locher, and P. Van Gelder, *Structure and function of bacterial outer membrane proteins: barrels in a nutshell*. *Mol Microbiol*, 2000. **37**(2): p. 239-53.
12. Tripathi, P., A. Beaussart, G. Andre, T. Rolain, S. Lebeer, J. Vanderleyden, P. Hols, and Y.F. Dufrene, *Towards a nanoscale view of lactic acid bacteria*. *Micron*, 2012. **43**(12): p. 1323-1330.
13. Reichmann, N.T. and A. Grundling, *Location, synthesis and function of glycolipids and polyglycerolphosphate lipoteichoic acid in Gram-positive bacteria of the phylum Firmicutes*. *Fems Microbiology Letters*, 2011. **319**(2): p. 97-105.
14. Brown, S., J.P.S. Maria, and S. Walker, *Wall Teichoic Acids of Gram-Positive Bacteria*. *Annual Review of Microbiology*, Vol 67, 2013. **67**: p. 313-336.
15. Zgurskaya, H.I., C.A. Lopez, and S. Gnanakaran, *Permeability Barrier of Gram-Negative Cell Envelopes and Approaches To Bypass It*. *Acs Infectious Diseases*, 2015. **1**(11): p. 512-522.
16. Mueller, P., H.T. Tien, W.C. Wescott, and D.O. Rudin, *Reconstitution of Excitable Cell Membrane Structure in Vitro*. *Circulation*, 1962. **26**(5): p. 1167-&.
17. Khan, M.S., N.S. Dosoky, and J.D. Williams, *Engineering Lipid Bilayer Membranes for Protein Studies*. *International Journal of Molecular Sciences*, 2013. **14**(11): p. 21561-21597.

18. Giner-Casares, J.J., G. Brezesinski, and H. Mohwald, *Langmuir monolayers as unique physical models*. *Current Opinion in Colloid & Interface Science*, 2014. **19**(3): p. 176-182.
19. Mouritsen, O.G., *Model Answers to Lipid Membrane Questions*. Cold Spring Harbor Perspectives in Biology, 2011. **3**(9).
20. Weiner, N., L. Lieb, S. Niemiec, C. Ramachandran, Z. Hu, and K. Egbaria, *Liposomes - a Novel Topical Delivery System for Pharmaceutical and Cosmetic Applications*. *Journal of Drug Targeting*, 1994. **2**(5): p. 405-410.
21. Sercombe, L., T. Veerati, F. Moheimani, S.Y. Wu, A.K. Sood, and S. Hua, *Advances and Challenges of Liposome Assisted Drug Delivery*. *Frontiers in Pharmacology*, 2015. **6**.
22. Mennicke, U. and T. Salditt, *Preparation of solid-supported lipid bilayers by spin-coating*. *Langmuir*, 2002. **18**(21): p. 8172-8177.
23. Richter, R.P., R. Berat, and A.R. Brisson, *Formation of solid-supported lipid bilayers: An integrated view*. *Langmuir*, 2006. **22**(8): p. 3497-3505.
24. Wagner, M.L. and L.K. Tamm, *Reconstituted syntaxin1A/SNAP25 interacts with negatively charged lipids as measured by lateral diffusion in planar supported bilayers*. *Biophysical Journal*, 2001. **81**(1): p. 266-275.
25. Bourgaux, C. and P. Couvreur, *Interactions of anticancer drugs with biomembranes: What can we learn from model membranes?* *Journal of Controlled Release*, 2014. **190**: p. 127-138.
26. Antony, H.A. and S.C. Parija, *Antimalarial drug resistance: An overview*. *Trop Parasitol*, 2016. **6**(1): p. 30-41.
27. Velayati, A.A., M.R. Masjedi, P. Farnia, P. Tabarsi, J. Ghanavi, A.H. ZiaZarifi, and S.E. Hoffner, *Emergence of New Forms of Totally Drug-Resistant Tuberculosis Bacilli Super*

- Extensively Drug-Resistant Tuberculosis or Totally Drug-Resistant Strains in Iran.* Chest, 2009. **136**(2): p. 420-425.
28. Housman, G., S. Byler, S. Heerboth, K. Lapinska, M. Longacre, N. Snyder, and S. Sarkar, *Drug Resistance in Cancer: An Overview.* Cancers, 2014. **6**(3): p. 1769-1792.
29. Teng, P., D. Huo, A. Nimmagadda, J.F. Wu, F.Y. She, M. Su, X.Y. Lin, J.Y. Yan, A.N. Cao, C.W. Xi, Y. Hu, and J.F. Cai, *Small Antimicrobial Agents Based on Acylated Reduced Amide Scaffold.* Journal of Medicinal Chemistry, 2016. **59**(17): p. 7877-7887.
30. Weissenhorn, W., *Crystal structure of the endophilin-A1 BAR domain.* Journal of Molecular Biology, 2005. **351**(3): p. 653-661.
31. Shai, Y., *Mode of action of membrane active antimicrobial peptides.* Biopolymers, 2002. **66**(4): p. 236-248.
32. Ladokhin, A.S., W.C. Wimley, and S.H. White, *Leakage of membrane vesicle contents: Determination of mechanism using fluorescence reuquenching.* Biophysical Journal, 1995. **69**(5): p. 1964-1971.
33. Ladokhin, A.S., M.E. Selsted, and S.H. White, *Sizing membrane pores in lipid vesicles by leakage of co-encapsulated markers: Pore formation by melittin.* Biophysical Journal, 1997. **72**(4): p. 1762-1766.
34. Kristensen, K., J.R. Henriksen, and T.L. Andresen, *Quantification of leakage from large unilamellar lipid vesicles by fluorescence correlation spectroscopy.* Biochimica Et Biophysica Acta-Biomembranes, 2014. **1838**(12): p. 2994-3002.
35. Barkleit, A., H. Foerstendorf, B. Li, A. Rossberg, H. Moll, and G. Bernhard, *Coordination of uranium(VI) with functional groups of bacterial lipopolysaccharide studied by EXAFS and FT-IR spectroscopy.* Dalton Transactions, 2011. **40**(38): p. 9868-9876.

36. Morales-Pennington, N.F., J. Wu, E.R. Farkas, S.L. Goh, T.M. Konyakhina, J.Y. Zheng, W.W. Webb, and G.W. Feigenson, *GUV preparation and imaging: Minimizing artifacts*. *Biochimica Et Biophysica Acta-Biomembranes*, 2010. **1798**(7): p. 1324-1332.
37. Biotechnology, S.C. *Calcein disodium salt*. 2019; Available from: <https://www.scbt.com/scbt/product/calcein-disodium-salt-108750-13-6>.
38. Olbrich, K., W. Rawicz, D. Needham, and E. Evans, *Water permeability and mechanical strength of polyunsaturated lipid bilayers*. *Biophysical Journal*, 2000. **79**(1): p. 321-327.
39. Kwok, R. and E. Evans, *Thermoelasticity of Large Lecithin Bilayer Vesicles*. *Biophysical Journal*, 1981. **35**(3): p. 637-652.
40. Longo, M.L., A.J. Waring, L.M. Gordon, and D.A. Hammer, *Area expansion and permeation of phospholipid membrane bilayers by influenza fusion peptides and melittin*. *Langmuir*, 1998. **14**(9): p. 2385-2395.
41. Sun, Y., C.C. Lee, W.C. Hung, F.Y. Chen, M.T. Lee, and H.W. Huang, *The bound states of amphipathic drugs in lipid bilayers: Study of curcumin*. *Biophysical Journal*, 2008. **95**(5): p. 2318-2324.
42. Evans, E., W. Rawicz, and B.A. Smith, *Back to the future: mechanics and thermodynamics of lipid biomembranes*. *Faraday Discussions*, 2013. **161**: p. 591-611.
43. Karal, M.A., J.M. Alam, T. Takahashi, V. Levadny, and M. Yamazaki, *Stretch-Activated Pore of the Antimicrobial Peptide, Magainin 2*. *Langmuir*, 2015. **31**(11): p. 3391-3401.
44. Khan, M.K., Wang, Q.Y., Fitzpatrick, M.E., *Atomic force microscopy (AFM) for materials characterization*. *Materials Characterization Using Nondestructive Evaluation (NDE) Methods*. 2016.

45. Benzitouni, S., M. Zaabat, J. Ebothe, B. Boudine, and R. Coste, *The use of advanced atomic force microscopy for the quantitative nanomechanical characterization of Co-doped ZnO thin films*. Chinese Journal of Physics, 2017. **55**(6): p. 2458-2467.
46. Kosaka, P.M., S. Gonzalez, C.M. Dominguez, A. Cebollada, A. San Paulo, M. Calleja, and J. Tamayo, *Atomic force microscopy reveals two phases in single stranded DNA self-assembled monolayers*. Nanoscale, 2013. **5**(16): p. 7425-7432.
47. nunano. *A pedant's (Christmas) guide to AFM probe terminology* 2016 December 14; Available from: <https://www.nunano.com/blog/2016/12/12/a-pedants-christmas-guide-to-afm-probe-terminology>.
48. Pittenger, B.E., N.; Su, C., *Quantitative mechanical property mapping at the nanoscale with PeakForce QNM*. 2010: Application Note Veeco Instruments Inc.
49. Zasloff, M., *Antimicrobial peptides of multicellular organisms*. Nature, 2002. **415**(6870): p. 389-395.
50. Reddy, K.V.R., R.D. Yedery, and C. Aranha, *Antimicrobial peptides: premises and promises*. International Journal of Antimicrobial Agents, 2004. **24**(6): p. 536-547.
51. Wu, Y.D. and S. Gellman, *Peptidomimetics*. Accounts of Chemical Research, 2008. **41**(10): p. 1231-1232.
52. Simon, R.J., R.S. Kania, R.N. Zuckermann, V.D. Huebner, D.A. Jewell, S. Banville, S. Ng, L. Wang, S. Rosenberg, C.K. Marlowe, D.C. Spellmeyer, R.Y. Tan, A.D. Frankel, D.V. Santi, F.E. Cohen, and P.A. Bartlett, *Peptoids - a Modular Approach to Drug Discovery*. Proceedings of the National Academy of Sciences of the United States of America, 1992. **89**(20): p. 9367-9371.

53. Cheng, R.P., S.H. Gellman, and W.F. DeGrado, *beta-peptides: From structure to function*. Chemical Reviews, 2001. **101**(10): p. 3219-3232.
54. Trabocchi, A., F. Guarna, and A. Guarna, *gamma- and delta-amino acids: Synthetic strategies and relevant applications*. Current Organic Chemistry, 2005. **9**(12): p. 1127-1153.
55. Graybill, T.L., M.J. Ross, B.R. Gauvin, J.S. Gregory, A.L. Harris, M.A. Ator, J.M. Rinker, and R.E. Dolle, *Synthesis and Evaluation of Azapeptide-Derived Inhibitors of Serine and Cysteine Proteases*. Bioorganic & Medicinal Chemistry Letters, 1992. **2**(11): p. 1375-1380.
56. Li, X., Y.D. Wu, and D. Yang, *alpha-Aminoxy Acids: New Possibilities from Foldamers to Anion Receptors and Channels*. Accounts of Chemical Research, 2008. **41**(10): p. 1428-1438.
57. Risseeuw, M.D.P., J. Mazurek, A. van Langenvelde, G.A. van der Marel, H.S. Overkleeft, and M. Overhand, *Synthesis of alkylated sugar amino acids: conformationally restricted L-Xaa-L-Ser/Thr mimics*. Organic & Biomolecular Chemistry, 2007. **5**(14): p. 2311-2314.
58. Horne, W.S. and S.H. Gellman, *Foldamers with Heterogeneous Backbones*. Accounts of Chemical Research, 2008. **41**(10): p. 1399-1408.
59. Nelson, J.C., J.G. Saven, J.S. Moore, and P.G. Wolynes, *Solvophobicity driven folding of nonbiological oligomers*. Science, 1997. **277**(5333): p. 1793-1796.
60. Teng, P., Y. Shi, P. Sang, and J.F. Cai, *gamma-AApeptides as a New Class of Peptidomimetics*. Chemistry-a European Journal, 2016. **22**(16): p. 5458-5466.
61. Shi, Y., P. Teng, P. Sang, F.Y. She, L.L. Wei, and J.F. Cai, *gamma-AApeptides: Design, Structure, and Applications*. Accounts of Chemical Research, 2016. **49**(3): p. 428-441.

62. Patch, J.A. and A.E. Barron, *Mimicry of bioactive peptides via non-natural, sequence-specific peptidomimetic oligomers*. *Current Opinion in Chemical Biology*, 2002. **6**(6): p. 872-877.
63. Zivec, M., Z. Jakopin, and S. Gobec, *Recent Advances in the Synthesis and Applications of Reduced Amide Pseudopeptides*. *Current Medicinal Chemistry*, 2009. **16**(18): p. 2289-2304.
64. Fridkin, G., T. Gilon, A. Loyter, and C. Gilon, *Systematic solid-phase synthesis of linear pseudooligolysines containing multiple adjacent CH<sub>2</sub>NH amide bond surrogates: potential agents for gene delivery*. *Journal of Peptide Research*, 2001. **58**(1): p. 36-44.
65. Lozano, J.M., M.P. Alba, M. Vanegas, Y. Silva, J.L. Torres-Castellanos, and M.E. Patarroyo, *MSP-1 malaria pseudopeptide analogs: Biological and immunological significance and three-dimensional structure*. *Biological Chemistry*, 2003. **384**(1): p. 71-82.
66. Todorovic, A., J.R. Holder, J.W. Scott, and C. Haskell-Luevano, *Synthesis and activity of the melanocortin Xaa-D-Phe-Arg-Trp-NH<sub>2</sub> tetrapeptides with amide bond modifications*. *Journal of Peptide Research*, 2004. **63**(3): p. 270-278.
67. Coburn, C.A., S.J. Stachel, K.G. Jones, T.G. Steele, D.M. Rush, J. DiMuzio, B.L. Pietrak, M.T. Lai, Q. Huang, J. Lineberger, L.X. Jin, S. Munshi, M.K. Holloway, A. Espeseth, A. Simon, D. Hazuda, S.L. Graham, and J.P. Vacca, *BACE-1 inhibition by a series of psi[CH<sub>2</sub>NH] reduced amide isosteres*. *Bioorganic & Medicinal Chemistry Letters*, 2006. **16**(14): p. 3635-3638.

68. Epand, R.F., P.B. Savage, and R.M. Epand, *Bacterial lipid composition and the antimicrobial efficacy of cationic steroid compounds (Ceragenins)*. *Biochimica Et Biophysica Acta-Biomembranes*, 2007. **1768**(10): p. 2500-2509.
69. Portet, T., S.E. Gordon, and S.L. Keller, *Increasing Membrane Tension Decreases Miscibility Temperatures; an Experimental Demonstration via Micropipette Aspiration*. *Biophysical Journal*, 2012. **103**(8): p. L35-L37.
70. Bagatolli, L.A. and D. Needham, *Quantitative optical microscopy and micromanipulation studies on the lipid bilayer membranes of giant unilamellar vesicles*. *Chemistry and Physics of Lipids*, 2014. **181**: p. 99-120.
71. Dimova, R., *Recent developments in the field of bending rigidity measurements on membranes*. *Advances in Colloid and Interface Science*, 2014. **208**: p. 225-234.
72. Chen, Y.F., T.L. Sun, Y. Sun, and H.W. Huang, *Interaction of Daptomycin with Lipid Bilayers: A Lipid Extracting Effect*. *Biochemistry*, 2014. **53**(33): p. 5384-5392.
73. Lee, M.T., T.L. Sun, W.C. Hung, and H.W. Huang, *Process of inducing pores in membranes by melittin*. *Proceedings of the National Academy of Sciences of the United States of America*, 2013. **110**(35): p. 14243-14248.
74. Sun, Y., W.C. Hung, F.Y. Chen, C.C. Lee, and H.W. Huang, *Interaction of Tea Catechin (-)-Epigallocatechin Gallate with Lipid Bilayers*. *Biophysical Journal*, 2009. **96**(3): p. 452a-452a.
75. Dufrene, Y.F. and G.U. Lee, *Advances in the characterization of supported lipid films with the atomic force microscope*. *Biochimica Et Biophysica Acta-Biomembranes*, 2000. **1509**(1-2): p. 14-41.

76. Leonenko, Z.V., A. Carnini, and D.T. Cramb, *Supported planar bilayer formation by vesicle fusion: the interaction of phospholipid vesicles with surfaces and the effect of gramicidin on bilayer properties using atomic force microscopy*. *Biochimica Et Biophysica Acta-Biomembranes*, 2000. **1509**(1-2): p. 131-147.
77. Shaw, J.E., J.R. Alattia, J.E. Verity, G.G. Prive, and C.M. Yip, *Mechanisms of antimicrobial peptide action: Studies of indolicidin assembly at model membrane interfaces by in situ atomic force microscopy*. *Journal of Structural Biology*, 2006. **154**(1): p. 42-58.
78. Goksu, E.I., J.M. Vanegas, C.D. Blanchette, W.C. Lin, and M.L. Longo, *AFM for structure and dynamics of biomembranes*. *Biochimica Et Biophysica Acta-Biomembranes*, 2009. **1788**(1): p. 254-266.
79. Dimitriadis, E.K., F. Horkay, J. Maresca, B. Kachar, and R.S. Chadwick, *Determination of elastic moduli of thin layers of soft material using the atomic force microscope*. *Biophysical Journal*, 2002. **82**(5): p. 2798-2810.
80. Garcia-Manyes, S., G. Oncins, and F. Sanz, *Effect of ion-binding and chemical phospholipid structure on the nanomechanics of lipid bilayers studied by force spectroscopy*. *Biophysical Journal*, 2005. **89**(3): p. 1812-1826.
81. Garcia-Manyes, S. and F. Sanz, *Nanomechanics of lipid bilayers by force spectroscopy with AFM: A perspective*. *Biochimica Et Biophysica Acta-Biomembranes*, 2010. **1798**(4): p. 741-749.
82. Garcia-Manyes, S., G. Oncins, L. Redondo, and F. Sanz, *Nanomechanics of Lipid Bilayers: Heads or Tails?* *Biophysical Journal*, 2010. **98**(3): p. 75a-75a.

83. Picas, L., P.E. Milhiet, and J. Hernandez-Borrell, *Atomic force microscopy: A versatile tool to probe the physical and chemical properties of supported membranes at the nanoscale*. Chemistry and Physics of Lipids, 2012. **165**(8): p. 845-860.
84. Shamitko-Klingensmith, N., K.M. Molchanoff, K.A. Burke, G.J. Magnone, and J. Legleiter, *Mapping the Mechanical Properties of Cholesterol-Containing Supported Lipid Bilayers with Nanoscale Spatial Resolution*. Langmuir, 2012. **28**(37): p. 13411-13422.
85. Wang, X., R.N. Sanderson, and R. Ragan, *Evaluation of Young's Modulus of Tethered 1-Palmitoyl-2-oleoyl-sn-glycero-3-phosphocholine Membranes Using Atomic Force Spectroscopy*. Journal of Physical Chemistry C, 2014. **118**(50): p. 29301-29309.
86. Suarez-Germa, C., A. Morros, M.T. Montero, J. Hernandez-Borrell, and O. Domenech, *Combined force spectroscopy, AFM and calorimetric studies to reveal the nanostructural organization of biomimetic membranes*. Chemistry and Physics of Lipids, 2014. **183**: p. 208-217.
87. Garcia-Arribas, A.B., J.V. Busto, A. Alonso, and F.M. Goni, *Atomic Force Microscopy Characterization of Palmitoylceramide and Cholesterol Effects on Phospholipid Bilayers: A Topographic and Nanomechanical Study*. Langmuir, 2015. **31**(10): p. 3135-3145.
88. Redondo-Morata, L., R.L. Sanford, O.S. Andersen, and S. Scheuring, *Effect of Statins on the Nanomechanical Properties of Supported Lipid Bilayers*. Biophysical Journal, 2016. **111**(2): p. 363-372.
89. Pan, J.J. and N.K. Khadka, *Kinetic Defects Induced by Melittin in Model Lipid Membranes: A Solution Atomic Force Microscopy Study*. Journal of Physical Chemistry B, 2016. **120**(20): p. 4625-4634.

90. Heerklotz, H. and J. Seelig, *Leakage and lysis of lipid membranes induced by the lipopeptide surfactin*. European Biophysics Journal with Biophysics Letters, 2007. **36**(4-5): p. 305-314.
91. Shi, Z., J.N. Sachs, E. Rhoades, and T. Baumgart, *Biophysics of alpha-synuclein induced membrane remodelling*. Physical Chemistry Chemical Physics, 2015. **17**(24): p. 15561-15568.
92. Lee, M.T., W.C. Hung, F.Y. Chen, and H.W. Huang, *Mechanism and kinetics of pore formation in membranes by water-soluble amphipathic peptides*. Proceedings of the National Academy of Sciences of the United States of America, 2008. **105**(13): p. 5087-5092.
93. Kucerka, N., M.P. Nieh, and J. Katsaras, *Fluid phase lipid areas and bilayer thicknesses of commonly used phosphatidylcholines as a function of temperature*. Biochimica Et Biophysica Acta-Biomembranes, 2011. **1808**(11): p. 2761-2771.
94. Kucerka, N., B.W. Holland, C.G. Gray, B. Tomberli, and J. Katsaras, *Scattering Density Profile Model of POPG Bilayers As Determined by Molecular Dynamics Simulations and Small-Angle Neutron and X-ray Scattering Experiments*. Journal of Physical Chemistry B, 2012. **116**(1): p. 232-239.
95. Pan, J.J., D. Marquardt, F.A. Heberle, N. Kucerka, and J. Katsaras, *Revisiting the bilayer structures of fluid phase phosphatidylglycerol lipids: Accounting for exchangeable hydrogens*. Biochimica Et Biophysica Acta-Biomembranes, 2014. **1838**(11): p. 2966-2969.
96. Ho, C.S., N.K. Khadka, and J.J. Pan, *Sub-ten-nanometer heterogeneity of solid supported lipid membranes determined by solution atomic force microscopy*. Biochimica Et Biophysica Acta-Biomembranes, 2016. **1858**(2): p. 181-188.

97. Connell, S.D., G. Heath, P.D. Olmsted, and A. Kisil, *Critical point fluctuations in supported lipid membranes*. Faraday Discussions, 2013. **161**: p. 91-111.
98. Honerkamp-Smith, A.R., P. Cicuta, M.D. Collins, S.L. Veatch, M. den Nijs, M. Schick, and S.L. Keller, *Line tensions, correlation lengths, and critical exponents in lipid membranes near critical points*. Biophysical Journal, 2008. **95**(1): p. 236-246.
99. Honerkamp-Smith, A.R., S.L. Veatch, and S.L. Keller, *An introduction to critical points for biophysicists; observations of compositional heterogeneity in lipid membranes*. Biochimica Et Biophysica Acta-Biomembranes, 2009. **1788**(1): p. 53-63.
100. Amazon, J.J. and G.W. Feigensohn, *Lattice simulations of phase morphology on lipid bilayers: Renormalization, membrane shape, and electrostatic dipole interactions*. Physical Review E, 2014. **89**(2).
101. Stetter, F.W.S. and T. Hugel, *The Nanomechanical Properties of Lipid Membranes are Significantly Influenced by the Presence of Ethanol*. Biophysical Journal, 2013. **104**(5): p. 1049-1055.
102. Kim, J., G. Kim, and P.S. Cremer, *Investigations of water structure at the solid/liquid interface in the presence of supported lipid bilayers by vibrational sum frequency spectroscopy*. Langmuir, 2001. **17**(23): p. 7255-7260.
103. Das, C., K.H. Sheikh, P.D. Olmsted, and S.D. Connell, *Nanoscale mechanical probing of supported lipid bilayers with atomic force microscopy*. Physical Review E, 2010. **82**(4).
104. Khadka, N.K., X.L. Cheng, C.S. Ho, J. Katsaras, and J.J. Pan, *Interactions of the Anticancer Drug Tamoxifen with Lipid Membranes*. Biophysical Journal, 2015. **108**(10): p. 2492-2501.

105. Seghezza, S., S. Dante, A. Diaspro, and C. Canale, *High resolution nanomechanical characterization of multi-domain model membranes by fast Force Volume*. Journal of Molecular Recognition, 2015. **28**(12): p. 742-750.
106. Redondo-Morata, L., M.I. Giannotti, and F. Sanz, *Structural impact of cations on lipid bilayer models: Nanomechanical properties by AFM-force spectroscopy*. Molecular Membrane Biology, 2014. **31**(1): p. 17-28.
107. Redondo-Morata, L., M.I. Giannotti, and F. Sanz, *Influence of Cholesterol on the Phase Transition of Lipid Bilayers: A Temperature-Controlled Force Spectroscopy Study*. Langmuir, 2012. **28**(35): p. 12851-12860.
108. Lima, L.M.C., M.I. Giannotti, L. Redondo-Morata, M.L.C. Vale, E.F. Marques, and F. Sanz, *Morphological and Nanomechanical Behavior of Supported Lipid Bilayers on Addition of Cationic Surfactants*. Langmuir, 2013. **29**(30): p. 9352-9361.
109. Alessandrini, A., H.M. Seeger, T. Caramaschi, and P. Facci, *Dynamic Force Spectroscopy on Supported Lipid Bilayers: Effect of Temperature and Sample Preparation*. Biophysical Journal, 2012. **103**(1): p. 38-47.
110. Gumi-Audenis, B., F. Sanz, and M.I. Giannotti, *Impact of galactosylceramides on the nanomechanical properties of lipid bilayer models: an AFM-force spectroscopy study*. Soft Matter, 2015. **11**(27): p. 5447-5454.
111. Sullan, R.M.A., J.K. Li, C.C. Hao, G.C. Walker, and S. Zou, *Cholesterol-Dependent Nanomechanical Stability of Phase-Segregated Multicomponent Lipid Bilayers*. Biophysical Journal, 2010. **99**(2): p. 507-516.

112. Zhong, J., C.H. Yang, W.F. Zheng, L.X. Huang, Y.K. Hong, L.J. Wang, and Y.L. Sha, *The role of calcium ions in the interactions of PrP106-126 amide with model membranes*. Colloids and Surfaces B-Biointerfaces, 2010. **77**(1): p. 40-46.
113. Henriksen, J., A.C. Rowat, E. Brief, Y.W. Hsueh, J.L. Thewalt, M.J. Zuckermann, and J.H. Ipsen, *Universal behavior of membranes with sterols*. Biophysical Journal, 2006. **90**(5): p. 1639-1649.
114. Venable, R.M., F.L.H. Brown, and R.W. Pastor, *Mechanical properties of lipid bilayers from molecular dynamics simulation*. Chemistry and Physics of Lipids, 2015. **192**: p. 60-74.
115. Chernomordik, L.V. and M.M. Kozlov, *Mechanics of membrane fusion*. Nature Structural & Molecular Biology, 2008. **15**(7): p. 675-683.
116. Papahadjopoulos, D.V., W.J.; Pangborn, W.J.; Poste, G., *Studies on Membrane-Fusion .II. Induction of Fusion in Pure Phospholipid Membranes by Calcium-Ions and Other Divalent Metals*. Biochimica Et Biophysica Acta, 1976. **448**(2): p. 265-283.
117. Nagle, J.F. and S. Tristram-Nagle, *Structure of lipid bilayers*. Biochimica Et Biophysica Acta-Reviews on Biomembranes, 2000. **1469**(3): p. 159-195.
118. Han, X.J., A.S. Achalkumar, M.R. Cheetham, S.D.A. Connell, B.R.G. Johnson, R.J. Bushby, and S.D. Evans, *A Self-assembly Route for Double Bilayer Lipid Membrane Formation*. Chemphyschem, 2010. **11**(3): p. 569-574.
119. Ribeiro, A.C.F., O. Ortona, S.M.N. Simoes, C.I.A.V. Santos, P.M.R.A. Prazeres, A.J.M. Valente, V.M.M. Lobo, and H.D. Burrows, *Binary mutual diffusion coefficients of aqueous solutions of sucrose, lactose, glucose, and fructose in the temperature range from (298.15 to 328.15) K*. Journal of Chemical and Engineering Data, 2006. **51**(5): p. 1836-1840.

120. Leventis, R. and J.R. Silvius, *Use of cyclodextrins to monitor transbilayer movement and differential lipid affinities of cholesterol*. Biophysical Journal, 2001. **81**(4): p. 2257-2267.
121. Woo, S.Y. and H. Lee, *All-atom simulations and free-energy calculations of coiled-coil peptides with lipid bilayers: binding strength, structural transition, and effect on lipid dynamics*. Scientific Reports, 2016. **6**.
122. Karal, M.A., V. Levadnyy, T.A. Tsuboi, M. Belaya, and M. Yamazaki, *Electrostatic interaction effects on tension-induced pore formation in lipid membranes*. Physical Review E, 2015. **92**(1).
123. Henderson, J.M., A.J. Waring, F. Separovic, and K.Y.C. Lee, *Antimicrobial Peptides Share a Common Interaction Driven by Membrane Line Tension Reduction*. Biophysical Journal, 2016. **111**(10): p. 2176-2189.
124. Vitkova, V., P. Meleard, T. Pott, and I. Bivas, *Alamethicin influence on the membrane bending elasticity*. European Biophysics Journal with Biophysics Letters, 2006. **35**(3): p. 281-286.
125. Pabst, G., S. Danner, R. Podgornik, and J. Katsaras, *Entropy-driven softening of fluid lipid Bilayers by alamethicin*. Langmuir, 2007. **23**(23): p. 11705-11711.
126. Pan, J.J., D.P. Tieleman, J.F. Nagle, N. Kucerka, and S. Tristram-Nagle, *Alamethicin in lipid bilayers: Combined use of X-ray scattering and MD simulations*. Biochimica Et Biophysica Acta-Biomembranes, 2009. **1788**(6): p. 1387-1397.
127. Pott, T., C. Gerbeaud, N. Barbier, and P. Meleard, *Melittin modifies bending elasticity in an unexpected way*. Chemistry and Physics of Lipids, 2015. **185**: p. 99-108.
128. Bouvrais, H., P. Meleard, T. Pott, K.J. Jensen, J. Brask, and J.H. Ipsen, *Softening of POPC membranes by magainin*. Biophysical Chemistry, 2008. **137**(1): p. 7-12.

129. McIntosh, T.J. and S.A. Simon, *Roles of bilayer material properties in function and distribution of membrane proteins*. Annual Review of Biophysics and Biomolecular Structure, 2006. **35**: p. 177-198.
130. Storm, D.R., K.S. Rosenthal, and P.E. Swanson, *Polymyxin and Related Peptide Antibiotics*. Annual Review of Biochemistry, 1977. **46**: p. 723-763.
131. Falagas, M.E. and S.K. Kasiakou, *Toxicity of polymyxins: a systematic review of the evidence from old and recent studies*. Critical Care, 2006. **10**(1).
132. Evans, M.E., D.J. Feola, and R.P. Rapp, *Polymyxin B sulfate and colistin: Old antibiotics for emerging multiresistant gram-negative bacteria*. Annals of Pharmacotherapy, 1999. **33**(9): p. 960-967.
133. Li, J., R.L. Nation, J.D. Turnidge, R.W. Milne, K. Coulthard, C.R. Rayner, and D.L. Paterson, *Colistin: the re-emerging antibiotic for multidrug-resistant Gram-negative bacterial infections*. Lancet Infectious Diseases, 2006. **6**(9): p. 589-601.
134. Falagas, M.E. and S.K. Kasiakou, *Colistin: The revival of polymyxins for the management of multidrug-resistant gram-negative bacterial infections*. Clinical Infectious Diseases, 2005. **40**(9): p. 1333-1341.
135. Arnold, T.M., G.N. Forrest, and K.J. Messmer, *Polymyxin antibiotics for gram-negative infections*. American Journal of Health-System Pharmacy, 2007. **64**(8): p. 819-826.
136. Costerto, J.W., J.M. Ingram, and K.J. Cheng, *Structure and Function of Cell-Envelope of Gram-Negative Bacteria*. Bacteriological Reviews, 1974. **38**(1): p. 87-110.
137. Labischinski, H., G. Barnickel, H. Bradaczek, D. Naumann, E.T. Rietschel, and P. Giesbrecht, *High State of Order of Isolated Bacterial Lipopolysaccharide and Its Possible*

- Contribution to the Permeation Barrier Property of the Outer-Membrane.* Journal of Bacteriology, 1985. **162**(1): p. 9-20.
138. Snyder, S., D. Kim, and T.J. McIntosh, *Lipopolysaccharide bilayer structure: Effect of chemotype, core mutations, divalent cations, and temperature.* Biochemistry, 1999. **38**(33): p. 10758-10767.
139. Morrison, D.C. and D.M. Jacobs, *Binding of Polymyxin B to Lipid A Portion of Bacterial Lipopolysaccharides.* Immunochemistry, 1976. **13**(10): p. 813-818.
140. Schindler, M. and M.J. Osborn, *Interaction of Divalent Cations and Polymyxin B with Lipopolysaccharide.* Biochemistry, 1979. **18**(20): p. 4425-4430.
141. Moore, R.A., N.C. Bates, and R.E.W. Hancock, *Interaction of Polycationic Antibiotics with Pseudomonas-Aeruginosa Lipopolysaccharide and Lipid-a Studied by Using Dansyl-Polymyxin.* Antimicrobial Agents and Chemotherapy, 1986. **29**(3): p. 496-500.
142. McInerney, M.P., K.D. Roberts, P.E. Thompson, J. Li, R.L. Nation, T. Velkov, and J.A. Nicolazzo, *Quantitation of Polymyxin-Lipopolysaccharide Interactions Using an Image-Based Fluorescent Probe.* Journal of Pharmaceutical Sciences, 2016. **105**(2): p. 1006-1010.
143. Rifkind, D. and J.D. Palmer, *Neutralization of Endotoxin Toxicity in Chick Embryos by Antibiotics.* Journal of Bacteriology, 1966. **92**(4): p. 815-819.
144. Koike, M., K. Iida, and T. Matsuo, *Electron Microscopic Studies on Mode of Action of Polymyxin.* Journal of Bacteriology, 1969. **97**(1): p. 448-452.
145. Hancock, R.E.W., *Alterations in Outer-Membrane Permeability.* Annual Review of Microbiology, 1984. **38**: p. 237-264.

146. Vaara, M., *Agents That Increase the Permeability of the Outer-Membrane*. Microbiological Reviews, 1992. **56**(3): p. 395-411.
147. Newton, B.A., *Properties and Mode of Action of the Polymyxins*. Bacteriological Reviews, 1956. **20**(1): p. 14-27.
148. Cajal, Y., J. Ghanta, K. Easwaran, A. Surolia, and M.K. Jain, *Specificity for the exchange of phospholipids through polymyxin B mediated intermembrane molecular contacts*. Biochemistry, 1996. **35**(18): p. 5684-5695.
149. Feingold, D.S., J.N. Goldman, and H.M. Kuritz, *Locus of Lethal Event in Serum Bactericidal Reaction*. Journal of Bacteriology, 1968. **96**(6): p. 2127-2131.
150. Cerny, G. and M. Teuber, *Differential Release of Periplasmic Versus Cytoplasmic Enzymes from Escherichia Coli B by Polymyxin B*. Archiv Fur Mikrobiologie, 1971. **78**(2): p. 166-179.
151. Sampson, T.R., X. Liu, M.R. Schroeder, C.S. Kraft, E.M. Burd, and D.S. Weiss, *Rapid Killing of Acinetobacter baumannii by Polymyxins Is Mediated by a Hydroxyl Radical Death Pathway*. Antimicrobial Agents and Chemotherapy, 2012. **56**(11): p. 5642-5649.
152. Lopes, J. and W.E. Inniss, *Electron Microscopy of Effect of Polymyxin on Escherichia Coli Lipopolysaccharide*. Journal of Bacteriology, 1969. **100**(2): p. 1128-1130.
153. Peterson, A.A., R.E.W. Hancock, and E.J. McGroarty, *Binding of Polycationic Antibiotics and Polyamines to Lipopolysaccharides of Pseudomonas-Aeruginosa*. Journal of Bacteriology, 1985. **164**(3): p. 1256-1261.
154. Zhang, L.J., P. Dhillon, H. Yan, S. Farmer, and R.E.W. Hancock, *Interactions of bacterial cationic peptide antibiotics with outer and cytoplasmic membranes of Pseudomonas aeruginosa*. Antimicrobial Agents and Chemotherapy, 2000. **44**(12): p. 3317-3321.

155. Clausell, A., M. Garcia-Subirats, M. Pujol, M.A. Busquets, F. Rabanal, and Y. Cajal, *Gram-negative outer and inner membrane models: Insertion of cyclic cationic lipopeptides*. Journal of Physical Chemistry B, 2007. **111**(3): p. 551-563.
156. Schroder, G., K. Brandenburg, and U. Seydel, *Polymyxin B Induces Transient Permeability Fluctuations in Asymmetric Planar Lipopolysaccharide Phospholipid Bilayers*. Biochemistry, 1992. **31**(3): p. 631-638.
157. Wiese, A., M. Munstermann, T. Gutschmann, B. Lindner, K. Kawahara, U. Zahringer, and U. Seydel, *Molecular mechanisms of polymyxin B Membrane interactions: Direct correlation between surface charge density and self-promoted transport*. Journal of Membrane Biology, 1998. **162**(2): p. 127-138.
158. Bhattacharjya, S., S.A. David, V.I. Mathan, and P. Balaram, *Polymyxin B nonapeptide: Conformations in water and in the lipopolysaccharide-bound state determined by two-dimensional NMR and molecular dynamics*. Biopolymers, 1997. **41**(3): p. 251-265.
159. Pristovsek, P. and J. Kidric, *Solution structure of polymyxins B and E and effect of binding to lipopolysaccharide: An MMR and molecular modeling study*. Journal of Medicinal Chemistry, 1999. **42**(22): p. 4604-4613.
160. Mares, J., S. Kumaran, M. Gobbo, and O. Zerbe, *Interactions of Lipopolysaccharide and Polymyxin Studied by NMR Spectroscopy*. Journal of Biological Chemistry, 2009. **284**(17): p. 11498-11506.
161. Dupuy, F.G., I. Pagano, K. Andenoro, M.F. Peralta, Y. Elhady, F. Heinrich, and S. Tristram-Nagle, *Selective Interaction of Colistin with Lipid Model Membranes*. Biophysical Journal, 2018. **114**(4): p. 919-928.

162. Roes, S., U. Seydel, and T. Gutschmann, *Probing the properties of lipopolysaccharide monolayers and their interaction with the antimicrobial peptide polymyxin B by atomic force microscopy*. Langmuir, 2005. **21**(15): p. 6970-6978.
163. Oh, Y.J., B. Plochberger, M. Rechberger, and P. Hinterdorfer, *Characterizing the effect of polymyxin B antibiotics to lipopolysaccharide on Escherichiacoli surface using atomic force microscopy*. Journal of Molecular Recognition, 2017. **30**(6): p. e2605.
164. Ho, C.S., N.K. Khadka, F.Y. She, J.F. Cai, and J.J. Pan, *Polyglutamine aggregates impair lipid membrane integrity and enhance lipid membrane rigidity*. Biochimica Et Biophysica Acta-Biomembranes, 2016. **1858**(4): p. 661-670.
165. Khadka, N.K., P. Teng, J.F. Cai, and J.J. Pan, *Modulation of lipid membrane structural and mechanical properties by a peptidomimetic derived from reduced amide scaffold*. Biochimica Et Biophysica Acta-Biomembranes, 2017. **1859**(5): p. 734-744.
166. Ebbensgaard, A., H. Mordhorst, M.T. Overgaard, C.G. Nielsen, F.M. Aarestrup, and E.B. Hansen, *Comparative Evaluation of the Antimicrobial Activity of Different Antimicrobial Peptides against a Range of Pathogenic Bacteria*. Plos One, 2015. **10**(12).
167. Matsuzaki, K., K. Sugishita, and K. Miyajima, *Interactions of an antimicrobial peptide, magainin 2, with lipopolysaccharide-containing liposomes as a model for outer membranes of Gram-negative bacteria*. Febs Letters, 1999. **449**(2-3): p. 221-224.
168. Nikaido, H., *Molecular basis of bacterial outer membrane permeability revisited*. Microbiology and Molecular Biology Reviews, 2003. **67**(4): p. 593-656.
169. Smit, J., Y. Kamio, and H. Nikaido, *Outer Membrane of Salmonella-Typhimurium - Chemical-Analysis and Freeze-Fracture Studies with Lipopolysaccharide Mutants*. Journal of Bacteriology, 1975. **124**(2): p. 942-958.

170. Moffatt, J.H., M. Harper, P. Harrison, J.D.F. Hale, E. Vinogradov, T. Seemann, R. Henry, B. Crane, F.S. Michael, A.D. Cox, B. Adler, R.L. Nation, J. Li, and J.D. Boyce, *Colistin Resistance in Acinetobacter baumannii Is Mediated by Complete Loss of Lipopolysaccharide Production*. *Antimicrobial Agents and Chemotherapy*, 2010. **54**(12): p. 4971-4977.
171. Yokota, S., H. Hakamada, S. Yamamoto, T. Sato, T. Shiraishi, M. Shinagawa, and S. Takahashi, *Release of large amounts of lipopolysaccharides from Pseudomonas aeruginosa cells reduces their susceptibility to colistin*. *International Journal of Antimicrobial Agents*, 2018. **51**(6): p. 888-896.
172. Bader, J. and M. Teuber, *Action of Polymyxin-B on Bacterial Membranes .1. Binding to O-Antigenic Lipopolysaccharide of Salmonella-Typhimurium*. *Zeitschrift Fur Naturforschung Section C-a Journal of Biosciences*, 1973. **28** c(7-8): p. 422-430.
173. Velkov, T., P.E. Thompson, R.L. Nation, and J. Li, *Structure-Activity Relationships of Polymyxin Antibiotics*. *Journal of Medicinal Chemistry*, 2010. **53**(5): p. 1898-1916.
174. Few, A.V., *The Interaction of Polymyxin-E with Bacterial and Other Lipids*. *Biochimica Et Biophysica Acta*, 1955. **16**(1): p. 137-145.
175. Imai, M., K. Inoue, and S. Nojima, *Effect of Polymyxin B on Liposomal Membranes Derived from Escherichia Coli Lipids*. *Biochimica Et Biophysica Acta*, 1975. **375**(1): p. 130-137.
176. Teuber, M. and J. Bader, *Action of Polymyxin B on Bacterial Membranes: Binding Capacities for Polymyxin B of Inner and Outer Membranes Isolated from Salmonella-Typhimurium G30*. *Archives of Microbiology*, 1976. **109**(1-2): p. 51-58.

177. Zidovetzki, R., U. Banerjee, D.W. Harrington, and S.I. Chan, *NMR Study of the Interactions of Polymyxin B, Gramicidin S, and Valinomycin with Dimyristoyllecithin Bilayers*. *Biochemistry*, 1988. **27**(15): p. 5686-5692.
178. Clausell, A., M.A. Busquets, M. Pujol, A. Alsina, and Y. Cajal, *Polymyxin B-lipid interactions in Langmuir-Blodgett monolayers of Escherichia coli lipids: A thermodynamic and atomic force microscopy study*. *Biopolymers*, 2004. **75**(6): p. 480-490.
179. Sixl, F. and H.J. Galla, *Polymyxin Interaction with Negatively Charged Lipid Bilayer Membranes and the Competitive Effect of Ca<sup>2+</sup>*. *Biochimica Et Biophysica Acta*, 1981. **643**(3): p. 626-635.
180. Newton, B.A., *Reversal of the Antibacterial Activity of Polymyxin by Divalent Cations*. *Nature*, 1953. **172**(4369): p. 160-161.
181. Allende, D. and T.J. McIntosh, *Lipopolysaccharides in bacterial membranes act like cholesterol in eukaryotic plasma membranes in providing protection against melittin-induced bilayer lysis*. *Biochemistry*, 2003. **42**(4): p. 1101-1108.
182. Nikaido, H. and M. Vaara, *Molecular Basis of Bacterial Outer Membrane Permeability*. *Microbiological Reviews*, 1985. **49**(1): p. 1-32.
183. Masuda, M. and N. Mochizuki, *Structural characteristics of BAR domain superfamily to sculpt the membrane*. *Seminars in Cell & Developmental Biology*, 2010. **21**(4): p. 391-398.
184. Blood, P.D. and G.A. Voth, *Direct observation of Bin/amphiphysin/Rvs (BAR) domain-induced membrane curvature by means of molecular dynamics simulations*. *Proceedings of the National Academy of Sciences of the United States of America*, 2006. **103**(41): p. 15068-15072.

185. Zimmerberg, J. and S. McLaughlin, *Membrane curvature: How BAR domains bend bilayers*. Current Biology, 2004. **14**(6): p. R250-R252.
186. Zhu, C., S.L. Das, and T. Baumgart, *Nonlinear Sorting, Curvature Generation, and Crowding of Endophilin N-BAR on Tubular Membranes*. Biophysical Journal, 2012. **102**(8): p. 1837-1845.
187. Jao, C.C., B.G. Hegde, J.L. Gallop, P.B. Hegde, H.T. McMahon, I.S. Haworth, and R. Langen, *Roles of Amphipathic Helices and the Bin/Amphiphysin/Rvs (BAR) Domain of Endophilin in Membrane Curvature Generation*. Journal of Biological Chemistry, 2010. **285**(26): p. 20164-20170.
188. Ambroso, M.R., B.G. Hegde, and R. Langen, *Endophilin A1 induces different membrane shapes using a conformational switch that is regulated by phosphorylation*. Proceedings of the National Academy of Sciences of the United States of America, 2014. **111**(19): p. 6982-6987.
189. Luo, L., J. Xue, A. Kwan, R. Gamsjaeger, J. Wielens, L. von Kleist, L. Cubeddu, Z. Guo, J.L. Stow, M.W. Parker, J.P. Mackay, and P.J. Robinson, *The Binding of Syndapin SH3 Domain to Dynamin Proline-rich Domain Involves Short and Long Distance Elements*. Journal of Biological Chemistry, 2016. **291**(18): p. 9411-9424.
190. Cestra, G., L. Castagnoli, L. Dente, O. Minenkova, A. Petrelli, N. Migone, U. Hoffmuller, J. Schneider-Mergener, and G. Cesareni, *The SH3 domains of endophilin and amphiphysin bind to the proline-rich region of synaptojanin 1 at distinct sites that display an unconventional binding specificity*. Journal of Biological Chemistry, 1999. **274**(45): p. 32001-32007.

191. Peter, B.J., H.M. Kent, I.G. Mills, Y. Vallis, P.J.G. Butler, P.R. Evans, and H.T. McMahon, *BAR domains as sensors of membrane curvature: The amphiphysin BAR structure*. Science, 2004. **303**(5657): p. 495-499.
192. Ayton, G.S., E. Lyman, V. Krishna, R.D. Swenson, C. Mim, V.M. Unger, and G.A. Voth, *New Insights into BAR Domain-Induced Membrane Remodeling*. Biophysical Journal, 2009. **97**(6): p. 1616-1625.
193. Gallop, J.L., C.C. Jao, H.M. Kent, P.J.G. Butler, P.R. Evans, R. Langen, and H.T. McMahon, *Mechanism of endophilin N-BAR domain-mediated membrane curvature*. Embo Journal, 2006. **25**(12): p. 2898-2910.
194. Fernandes, F., L.M.S. Loura, F.J. Chichon, J.L. Carrascosa, A. Fedorov, and M. Prieto, *Role of helix 0 of the N-BAR domain in membrane curvature generation*. Biophysical Journal, 2008. **94**(8): p. 3065-3073.
195. Bhatia, V.K., K.L. Madsen, P.Y. Bolinger, A. Kunding, P. Hedegard, U. Gether, and D. Stamou, *Amphipathic motifs in BAR domains are essential for membrane curvature sensing*. Embo Journal, 2009. **28**(21): p. 3303-3314.
196. Poudel, K.R., Y.M. Dong, H. Yu, A. Su, T. Ho, Y. Liu, K. Schulten, and J.H. Bai, *A time course of orchestrated endophilin action in sensing, bending, and stabilizing curved membranes*. Molecular Biology of the Cell, 2016. **27**(13): p. 2119-2132.
197. Cui, H.S., E. Lyman, and G.A. Voth, *Mechanism of Membrane Curvature Sensing by Amphipathic Helix Containing Proteins*. Biophysical Journal, 2011. **100**(5): p. 1271-1279.
198. Chen, Z.M., C. Zhu, C.J. Kuo, J. Robustelli, and T. Baumgart, *The N-Terminal Amphipathic Helix of Endophilin Does Not Contribute to Its Molecular Curvature*

- Generation Capacity*. Journal of the American Chemical Society, 2016. **138**(44): p. 14616-14622.
199. Ford, M.G.J., I.G. Mills, B.J. Peter, Y. Vallis, G.J.K. Praefcke, P.R. Evans, and H.T. McMahon, *Curvature of clathrin-coated pits driven by epsin*. Nature, 2002. **419**(6905): p. 361-366.
200. Antonny, B., S. BeraudDufour, P. Chardin, and M. Chabre, *N-terminal hydrophobic residues of the G-protein ADP-ribosylation factor-1 insert into membrane phospholipids upon GDP to GTP exchange*. Biochemistry, 1997. **36**(15): p. 4675-4684.
201. Suresh, S. and J.M. Edwardson, *The Endophilin N-BAR Domain Perturbs the Structure of Lipid Bilayers*. Biochemistry, 2010. **49**(27): p. 5766-5771.
202. Campelo, F., H.T. McMahon, and M.M. Kozlov, *The hydrophobic insertion mechanism of membrane curvature generation by proteins*. Biophysical Journal, 2008. **95**(5): p. 2325-2339.
203. Adam, J., N. Basnet, and N. Mizuno, *Structural insights into the cooperative remodeling of membranes by amphiphysin/BIN1*. Scientific Reports, 2015. **5**.
204. Cui, H.S., C. Mim, F.X. Vazquez, E. Lyman, V.M. Unger, and G.A. Voth, *Understanding the Role of Amphipathic Helices in N-BAR Domain Driven Membrane Remodeling*. Biophysical Journal, 2013. **104**(2): p. 404-411.

## APPENDIX A: LIST OF PUBLICATIONS

- **Nawal K. Khadka**, Chinta M. Aryal, Jianjun Pan. Lipopolysaccharide-Dependent Membrane Permeation and Lipid Clustering Caused by the Cyclic Lipopeptide Colistin. *ACS Omega* **2018**, DOI: 10.1021/acsomega.8b02260.
- Jianjun Pan, Annalisa Dalzini, **Nawal K. Khadka**, Chinta M. Aryal, Likai Song. Lipid Extraction by alpha-Synuclein Generates Semi-transmembrane Defects and Lipoprotein Nanoparticles. *ACS Omega* **2018**, 3: 9586-9597. PMID: PMC6120733.
- **Nawal K. Khadka**, Peng Teng, Jianfeng Cai, and Jianjun Pan. Modulation of Lipid Membrane Structural and Mechanical Properties by a Peptidomimetic Derived from Reduced Amide Scaffold. *Biochimica et Biophysica Acta - Biomembranes* **2017**, 1859: 734-744.
- Alekhya Nimmagadda, Xuan Liu, Peng Teng, Ma Su, Yaqiong Li, Qiao Qiao, **Nawal K. Khadka**, Xiaoting Sun, Jianjun Pan, Hai Xu, Qi Li, and Jianfeng Cai. Polycarbonates with Potent and Selective Antimicrobial Activity toward Gram-Positive Bacteria. *Biomacromolecules* **2017**, 18: 87-95. PMID: PMC4779675.
- Chian Sing Ho, **Nawal K. Khadka**, Fengyu She, Jianfeng Cai, and Jianjun Pan. Influenza M2 Transmembrane Domain Senses Membrane Heterogeneity and Enhances Membrane Curvature. *Langmuir* **2016**, 32: 6730-6738. PMID: PMC5131574.
- Jianjun Pan, **Nawal K. Khadka**. Kinetic Defects Induced by Melittin in Model Lipid Membranes: A Solution Atomic Force Microscopy Study. *The Journal of Physical Chemistry B* **2016**, 120: 4625-4634. PMID: PMC5123733
- Javier Alonso, Hafsa Khurshid, Jagannath Devkota, Zohreh Nemati, **Nawal K. Khadka**, Hariharan Srikanth, Jianjun Pan, and Manh-Huong Phan. Superparamagnetic Nanoparticles Encapsulated in Lipid Vesicles for Advanced Magnetic Hyperthermia and Biodetection. *Journal of Applied Physics* **2016**, 119: 083904.
- Chian Sing Ho, **Nawal K. Khadka**, Fengyu She, Jianfeng Cai, and Jianjun Pan. Polyglutamine Aggregates Impair Lipid Membrane Integrity and Enhance Lipid Membrane Rigidity. *Biochimica et Biophysica Acta – Biomembranes* **2016**, 1858: 661-670. PMID: PMC4779675
- Chian Sing Ho, **Nawal K. Khadka**, and Jianjun Pan. Sub-Ten-Nanometer Heterogeneity of Solid Supported Lipid Membranes Determined by Solution Atomic Force Microscopy. *Biochimica et Biophysica Acta – Biomembranes* **2016**, 1858: 181-188.
- **Nawal K. Khadka**, Chian Sing Ho, and Jianjun Pan. Macroscopic and Nanoscopic Heterogeneous Structures in a Three-Component Lipid Bilayer Mixtures Determined by Atomic Force Microscopy. *Langmuir* **2015**, 31: 12417-12425.
- **Nawal K. Khadka**, Xiaolin Cheng, Chian Sing Ho, John Katsaras, and Jianjun Pan. Interactions of the Anticancer Drug Tamoxifen with Lipid Membranes. *Biophysical Journal* **2015**, 108: 2492-2501.

- Jianjun Pan, Xiaolin Cheng, Melissa Sharp, Chian-Sing Ho, **Nawal Khadka**, John Katsaras. Structural and Mechanical Properties of Cardiolipin Lipid Bilayers Determined Using Neutron Spin Echo, Small Angle Neutron and X-ray Scattering, and Molecular Dynamics Simulations. *Soft Matter* **2014**, 11:130-138.

## APPENDIX B. COPYRIGHT PERMISSIONS

Sincerely,  
Nawal K Khadka  
Ph.D. Candidate  
Department of Physics  
USF, Tampa, Florida

ganesh-office@omega.acs.org  
to me

Tue, May 7, 9:35 AM ☆ ↶ ⋮

Dear Dr. Khadka,

Thank you for contacting us.

Permission can be granted. Please see the link below for more details:

<https://pubs.acs.org/pb-assets/acspubs/Migrated/dissertation.pdf>

Sincerely,  
Ksenija Golubovic  
Peer Review Analyst  
On behalf of

Dr. Krishna Ganesh  
Coeditor  
ACS Omega  
Phone: +1 434 326-1691  
Email: [Ganesh-office@omega.acs.org](mailto:Ganesh-office@omega.acs.org)  
\*\*\*

### American Chemical Society's Policy on Theses and Dissertations

**If your university requires you to obtain permission, you must use the RightsLink permission system.  
See RightsLink instructions at <http://pubs.acs.org/page/copyright/permissions.html>.**

This is regarding request for permission to include **your** paper(s) or portions of text from **your** paper(s) in your thesis. Permission is now automatically granted; please pay special attention to the **implications** paragraph below. The Copyright Subcommittee of the Joint Board/Council Committees on Publications approved the following:

#### Copyright permission for published and submitted material from theses and dissertations

ACS extends blanket permission to students to include in their theses and dissertations their own articles, or portions thereof, that have been published in ACS journals or submitted to ACS journals for publication, provided that the ACS copyright credit line is noted on the appropriate page(s).

#### Publishing implications of electronic publication of theses and dissertation material

Students and their mentors should be aware that posting of theses and dissertation material on the Web prior to submission of material from that thesis or dissertation to an ACS journal may affect publication in that journal. Whether Web posting is considered prior publication may be evaluated on a case-by-case basis by the journal's editor. If an ACS journal editor considers Web posting to be "prior publication", the paper will not be accepted for publication in that journal. If you intend to submit your unpublished paper to ACS for publication, check with the appropriate editor prior to posting your manuscript electronically.

**Reuse/Republishing of the Entire Work in Theses or Collections:** Authors may reuse all or part of the Submitted, Accepted or Published Work in a thesis or dissertation that the author writes and is required to submit to satisfy the criteria of degree-granting institutions. Such reuse is permitted subject to the ACS' "Ethical Guidelines to Publication of Chemical Research" (<http://pubs.acs.org/page/policy/ethics/index.html>); the author should secure written confirmation (via letter or email) from the respective ACS journal editor(s) to avoid potential conflicts with journal prior publication\*/embargo policies. Appropriate citation of the Published Work must be made. If the thesis or dissertation to be published is in electronic format, a direct link to the Published Work must also be included using the ACS Articles on



RightsLink®

[Home](#)[Create Account](#)[Help](#)

**Title:** Modulation of lipid membrane structural and mechanical properties by a peptidomimetic derived from reduced amide scaffold

**Author:** Nawal K. Khadka, Peng Teng, Jianfeng Cai, Jianjun Pan

**Publication:** Biochimica et Biophysica Acta (BBA) - Biomembranes

**Publisher:** Elsevier

**Date:** May 2017

© 2017 Elsevier B.V.

**LOGIN**

If you're a [copyright.com](#) user, you can login to RightsLink using your [copyright.com](#) credentials. Already a RightsLink user or want to [learn more?](#)

Please note that, as the author of this Elsevier article, you retain the right to include it in a thesis or dissertation, provided it is not published commercially. Permission is not required, but please ensure that you reference the journal as the original source. For more information on this and on your other retained rights, please visit: <https://www.elsevier.com/about/our-business/policies/copyright#Author-rights>

[BACK](#)[CLOSE WINDOW](#)

Copyright © 2019 [Copyright Clearance Center, Inc.](#) All Rights Reserved. [Privacy statement](#); [Terms and Conditions](#). Comments? We would like to hear from you. E-mail us at [customercare@copyright.com](mailto:customercare@copyright.com)

Review

# The Fluid—Mosaic Model of Membrane Structure: Still relevant to understanding the structure, function and dynamics of biological membranes after more than 40 years ☆

Garth L. Nicolson   

Show more

<https://doi.org/10.1016/j.bbamem.2013.10.019>

Under a Creative Commons license

Get rights and content

open access

 <https://s100.copyright.com/AppDispatchServlet?publisherName=ELS&center>

 Apps  instruments.pdf



### Creative Commons Attribution License (CC BY)

This article is available under the terms of the [Creative Commons Attribution License \(CC BY\)](#). You may distribute and copy the article, create extracts, abstracts, and other revised versions, adaptations or derivative works of or from an article (such as a translation), to include in a collective work (such as an anthology), to text or data mine the article, including for commercial purposes without permission from Elsevier. The original work must always be appropriately credited.

Permission is not required for this type of reuse.

CLOSE WINDOW

Copyright © 2019 [Copyright Clearance Center, Inc.](#) All Rights Reserved.  
Comments? We would like to hear from you. E-mail us at [customercare@copyright.com](mailto:customercare@copyright.com)

## Highlights

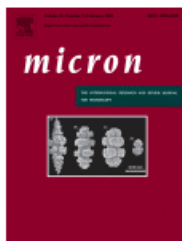
- An updated Fluid—Mosaic Membrane Model is proposed that takes into account data not available in 1972.
- The model stresses the roles of specialized fluctuating membrane domains, such as lipid rafts and protein complexes.
- Cooperative events that drive formation of lipid and protein complexes are discussed.
- Membrane-associated cytoskeletal networks and extracellular matrix structures limit lateral diffusion and range of motion.

Graphical abstract from ‘The Fluid—Mosaic Model of Membrane Structure: Still relevant to understanding the structure, function and dynamics of biological membranes after more than 40 years’ by Garth L. Nicolson [Biochimica et Biophysica Acta \(BBA\) - Biomembranes](#)

[Volume 1838, Issue 6, June 2014, Pages 1451-1466](#)



- [Home](#)
- [Account Info](#)
- [Help](#)



**Title:** Towards a nanoscale view of lactic acid bacteria  
**Author:** Prachi Tripathi,Audrey Beaussart,Guillaume Andre,Thomas Rolain,Sarah Lebeer,Jos Vanderleyden,Pascal Hols,Yves F. Dufrêne

**Publication:** Micron  
**Publisher:** Elsevier  
**Date:** December 2012

Copyright © 2012 Elsevier Ltd. All rights reserved.

Logged in as:  
 Nawal khadka  
 Account #:  
 3001443312

[LOGOUT](#)

### Order Completed

Thank you for your order.

This Agreement between 14601 N 42nd st ("You") and Elsevier ("Elsevier") consists of your license details and the terms and conditions provided by Elsevier and Copyright Clearance Center.

Your confirmation email will contain your order number for future reference.

[printable details](#)

License Number	4616550831872
License date	Jun 26, 2019
Licensed Content Publisher	Elsevier
Licensed Content Publication	Micron
Licensed Content Title	Towards a nanoscale view of lactic acid bacteria
Licensed Content Author	Prachi Tripathi,Audrey Beaussart,Guillaume Andre,Thomas Rolain,Sarah Lebeer,Jos Vanderleyden,Pascal Hols,Yves F. Dufrêne
Licensed Content Date	Dec 1, 2012
Licensed Content Volume	43
Licensed Content Issue	12
Licensed Content Pages	8
Type of Use	reuse in a thesis/dissertation
Portion	figures/tables/illustrations
Number of figures/tables/illustrations	1
Format	both print and electronic
Are you the author of this Elsevier article?	No
Will you be translating?	No
Original figure numbers	figure 1
Title of your thesis/dissertation	Modulations of Lipid Membranes Caused by Antimicrobial Agents and Helix 0 of Endophilin
Expected completion date	Aug 2019

Issue 23, 2015 Previous Article [Next Article](#)

**ChemComm**  
From the journal:  
**Chemical Communications**

## Anion transport across varying lipid membranes – the effect of lipophilicity

Michael J. Spooner<sup>a</sup> and Philip A. Gale<sup>a,b</sup>

[Author affiliations](#)

**Abstract**

The anion transport properties of a range of alkyl-substituted phenylthioureas were tested in vesicles of different lipid composition. Although changes in the bilayer affected the rate of transport for all compounds in the series, the 'ideal' log *P* for peak activity did not change depending on the composition of the bilayers tested.



**Check for updates**

**About** **Cited by** **Related**

M. J. Spooner and P. A. Gale, *Chem. Commun.*, 2015, **51**, 4883  
DOI: 10.1039/C5CC00823A

This article is licensed under a [Creative Commons Attribution 3.0 Unported Licence](#). Material from this article can be used in other publications provided that the correct acknowledgement is given with the reproduced material.

Reproduced material should be attributed as follows:

- For reproduction of material from NJC:  
[Original citation] - Published by The Royal Society of Chemistry (RSC) on behalf of the Centre National de la Recherche Scientifique (CNRS) and the RSC.
- For reproduction of material from PCCP:  
[Original citation] - Published by the PCCP Owner Societies.
- For reproduction of material from PPS:  
[Original citation] - Published by The Royal Society of Chemistry (RSC) on behalf of the European Society for Photobiology, the European Photochemistry Association, and RSC.
- For reproduction of material from all other RSC journals:  
[Original citation] - Published by The Royal Society of Chemistry.

Information about reproducing material from RSC articles with different licences is available on our [Permission Requests page](#).

Structures of lipids figure 2 from article is reused in this dissertation work.

M. J. Spooner and P. A. Gale, *Chem. Commun.*, 2015, **51**, 4883 DOI: 10.1039/C5CC00823A-  
Published by The Royal Society of Chemistry